MAGNETRON SPUTTERED METAL NITRIDE THIN FILMS FOR DEVICE APPLICATIONS

Ph.D. THESIS

by

RAVI PRAKASH

CENTRE OF NANOTECHNOLOGY
INDIAN INSTITUTE OF TECHNOLOGY ROORKEE
ROORKEE- 247667 (INDIA)
DECEMBER, 2018

MAGNETRON SPUTTERED METAL NITRIDE THIN FILMS FOR DEVICE APPLICATIONS

A THESIS

Submitted in partial fulfilment of the requirements for the award of the degree

of

DOCTOR OF PHILOSOPHY

in

PHYSICS

by

RAVI PRAKASH

CENTRE OF NANOTECHNOLOGY
INDIAN INSTITUTE OF TECHNOLOGY ROORKEE
ROORKEE- 247667 (INDIA)
DECEMBER, 2018

INDIAN INSTITUTE OF TECHNOLOGY ROORKEE
ROORKEE

CANDIDATE'S DECLARATION

I hereby certify that the work which is being presented in the thesis entitled **"MAGNETRON SPUTTERED METAL NITRIDE THIN FILMS FOR DEVICE APPLICATIONS"** in partial fulfilment of the requirements for the award of the Degree of Doctor of Philosophy and submitted in the Centre of Nanotechnology of the Indian Institute of Technology Roorkee, Roorkee is an authentic record of my own work carried out during a period from July, 2013 to December, 2018 under the supervision of Dr. Davinder Kaur, Professor, Department of Physics, Indian Institute of Technology Roorkee, Roorkee.

The matter presented in this thesis has not been submitted by me for the award of any other degree of this or any other Institute.

(RAVI PRAKASH)

This is to certify that the above statement made by the candidate is correct to the best of my knowledge.

(Davinder Kaur)
Supervisor

The Ph.D. Viva-Voce Examination of **Mr. Ravi Prakash**, Research Scholar, has been held on ……..

Chairman, SRC External Examiner

This is to certify that the student has made all the corrections in the thesis.

Supervisor Head of the Department

Date:

DEDICATED

TO

My beloved

Family

ABSTRACT

Metal nitride materials show enhanced performance in terms of physical and chemical properties as compared to their metal counterparts. In last decade, the thin films based on chromium nitride (CrN), titanium nitride (TiN), tungsten nitride (WN) and aluminium nitride (AlN) material have been studied extensively due to their wide range of potential applications such as protective coating, gas sensing, charge storage, diffusion barrier and memory storage. Moreover, the main reason for rising importance of metal nitride thin films is tailoring the properties by optimizing the thickness and composition. However, some binary metal nitrides are suggested as protective coating for cutting tools but those are not sufficient to fulfil the future demands. Therefore, ternary metal nitride nanocomposite thin films fabricated by addition of other metal into binary nitride matrix have attracted a great attention as refractory materials due to their wide spectrum of mechanical and electronic properties. In last couple of years, several advanced memory storage concepts have been evolved, but due to possessing tuneable electrical properties the resistive switching of metal nitride thin films is promising approach in terms of data storage. Recently, hierarchical nanostructures such as nanoball and nanowire of metal nitride thin films have been utilized for gas sensing applications due to providing high surface area.

The main objective of the thesis is to synthesize the various metal nitride thin films such as aluminium nitride (AlN), tungsten nitride (WN) and chromium tungsten nitride (CrWN) using DC magnetron sputtering technique. Thereafter, the resistive switching properties of AlN and WN thin films were investigated for non-volatile memory application in detail. Subsequently, the room temperature hydrogen gas sensing properties of palladium (Pd) capped WN thin film fabricated on porous silicon (PSi) substrate were also examined. The structural, corrosion and mechanical properties of CrWN nanocomposite thin films were investigated for industrial application such as protective coating for cutting tools.

This thesis is organized into six chapters. The summary of each chapter is discussed below:

Chapter 1 begins with historical overview and very incisive literature survey on the synthesis and properties of selected metal nitride thin films such as aluminium nitride (AlN), tungsten nitride (WN), chromium nitride and chromium tungsten nitride (CrWN). The chapter also provides essential information to understand the non-volatile memory storage, hydrogen gas sensor and protective coatings on cutting tools.

Chapter 2 present the details of the experimental techniques which have been employed for the synthesis and characterization of several metal nitride thin films. All thin film samples were fabricated using reactive DC magnetron sputtering technique. Various characterization techniques, such as X-rays diffraction (XRD), Raman Spectroscopy, X-Ray Photoelectronic Spectra (XPS), Atomic Force Microscopy (AFM) and Field Emission Scanning Electron Microscopy (FE-SEM) have been discussed in detail. Electrical properties of the aluminium nitride and tungsten nitride thin films were studied using Keithley 4200 semiconductor characterization system (SCS). Hydrogen gas sensing properties of nanoporous W_2N thin films were characterized using a custom made sensing setup. The Nanoindentation was used to study the mechanical properties such as hardness (H), elastic modulus (E), plasticity index (H/E) and resistance to plastic deformation (H^3/E^2) of CrWN nanocomposite thin films. In addition, a three electrode potentiostat was used to measure the corrosion rate of CrWN nanocomposite thin films.

Chapter 3 is divided into two sections. **Section 3.1** describes highly stable and bipolar resistive switching (RS) behaviour of aluminium nitride (AlN) thin film sandwiched between Cu (top) and Pt (bottom) electrodes. Resistive switching properties in Cu/AlN/Pt structure are induced by the formation/disruption of Cu conducting filaments in AlN thin film. Excellent non-volatile resistive switching characteristics have been observed at the voltage of + 2.6 V and - 1.7 V. Trap controlled space charge limited current (SCLC) and ohmic behaviour are the dominant conduction mechanisms at high resistance state (HRS) and low resistance state (LRS) respectively. The resistance ratio between HRS and LRS is found to be of the order of ~ 10^4. Moreover, the Cu/AlN/Pt structure also exhibited endurance upto > 10^4 cycles and a non-volatile retention time for > 10^4 sec. **Section 3.2** illustrates the influence of top electrode (TE) material on resistive switching properties of DC magnetron sputtered tungsten nitride (WN) thin film in TE (Ti, Al and Cu)/WN/Pt stack configuration. The Ti/WN/Pt and Al/WN/Pt structure exhibit two resistance states i.e. LRS and HRS, which were caused by formation and rupture of nitrogen vacancy related ionic filaments. Formation of additional Cu filaments in Cu/WN/Pt configuration is responsible for three resistance states (or say multilevel) switching. This study suggests that the electrode engineering of tungsten nitride thin film have potential for non-volatile and multilevel resistive memory application.

Chapter 4 depicts the room temperature hydrogen (H_2) gas sensing performance of the palladium modified tungsten nitride (Pd/W_2N) nanoballs (NBs) grown on the porous silicon substrate using reactive DC magnetron sputtering. Porous silicon substrate has attracted

enormous amount of consideration for gas sensing application due to its high reactive surface morphology. Reversible change in resistance was observed during hydrogenation and dehydrogenation process at room temperature. The H_2 gas sensing performances together with sensing mechanism of the Pd/W_2N NBs structure under low sensing range (5-500 ppm) were discussed in detail. Moreover, the prime requirements for sensing performance including stability, reproducibility and selectivity measurement are also studied at room temperature.

Chapter 5 describes the growth of chromium tungsten nitride ($Cr_{1-x}W_xN$) nanocomposite thin films on silicon (100) substrate using reactive magnetron co-sputtering. X-ray diffraction pattern of $Cr_{1-x}W_xN$ thin films reveal the presence of (111) and (200) orientation for different tungsten concentrations ($0 < x < 0.61$). In $Cr_{1-x}W_xN$ thin films, the atomic concentration (x) of tungsten (W) was controlled by varying the DC power on the W target. It is observed that, the addition of small amount of W atoms led to significant changes in the structural, electrochemical and mechanical properties of the $Cr_{1-x}W_xN$ films. The crystallite size of $Cr_{1-x}W_xN$ ($0 < x < 0.61$) thin films varies from 31.1 nm to 15.2 nm due to variation in nucleation rate and self-shadowing effect during deposition process. Electrochemical properties of these thin films were studied by Tafel polarization curves. The results show that, the addition of a certain amount of W atoms enhanced the corrosion rate which may be due to higher ratio between real surface area and projected area. Hardness of the $Cr_{1-x}W_xN$ thin films tends to increase with the decrease in grain size in accordance with the Hall-Petch relation. For $Cr_{0.48}W_{0.43}N$ thin film, the highest hardness of 43.18 GPa and elastic modulus of 341.02 GPa were achieved at the grain size of 15.2 nm.

Chapter 6 describes major conclusions drawn after thorough discussion and in-depth analysis that presented in individual chapters. A brief report on the scope for future work is also included.

ACKNOWLEDGEMENTS

Physics has a history of synthesizing many phenomena into a few theories.

Richard P. Feynman

This thesis is a part of years of experience and different person associated with this venture deserve special mention. It is with pleasure I record the acknowledgment to convey my deep sense gratitude for each and every one.

First, and foremost, I extend my sincerest gratitude to my supervisor Prof. Davinder Kaur, for her inspiration, keen insight, unwaning enthusiasm and willingness to share her knowledge and experience. She has supported me throughout my research with her patience and given immense freedom to work on my own. Her invaluable guidance and intellectual stimulation makes it possible to complete this work. I especially thank her for her prompt reading and careful analysis of my thesis.

I would also like to express my sincere thanks to Dr. R. K. Dutta, Head of the Centre and all other faculty members of Centre of Nanotechnology for their keen interest in this work. I take this opportunity to thank all the members of my SRC committee, Prof. R. P. Singh (Chairman)- Department of Biotechnology, Dr. P. Jeevanandam (Internal member)-Department of Chemistry and Dr. Tulika Maitra (External Member)- Department of Physics, IIT Roorkee for their invaluable suggestions and encouragement to carry out this work.

I am also grateful to Prof. Ramesh Chandra who has always been very generous and forthcoming in allowing me to run equipments at Institute Instrumentation Center (IIC), IIT Roorkee. His cheerful disposition has always been a great source of inspiration and encouragement. I am highly obliged and express my sincere thanks to the official & technical staff of the Institute Instrumentation Center and Centre of Nanotechnology.

It is my pleasure to acknowledge the advice and love received from my senior researchers in the lab; Dr. Navjot Kaur, Dr. Harish Sharma Akkera, Dr. Rahul Barman and Dr. Kirandeep Singh. They have shown utmost love and care in both my personal and academic matters. I greatly enjoyed working with all my lab mates Narendra Singh, Akhilesh Pandey, Shuvam Pawar, Shubham Sharma, Anuj Kumar, Pankaj Rawat, Krishan Kumar, Pradeep Kumar and Bhanu Ranjan and all the Master's students who completed their project work in "Functional Nanomaterials Research Lab" and have contributed for this lab. I thank them all for their full cooperation and ever needed help throughout to carry this work and also

for being around all the time. It was absolutely phenomenal experience to work with Dr. Ashwani Kumar, Dr. Amit Singh Rajput, Dr. Arvind Kumar and Ravikant of IIC. I would also thankful to Prof. Beer Pal Singh (Chaudhary Charan Singh University, Meerut) for his immense motivation and support since my post-graduation.

The inspiration, support, cooperation and patience which I have received from my friends are beyond the scope of any acknowledgement, yet I would express my heartfelt gratitude to them. I must accolade the company of Sachin Kumar, Yogesh Verma, Bhavna, Priyanka Gaur, Ranjeet, Izhar Faisal, Bijendra Singh, Gaurav Bharti, Aditya Kumar, Ashu Chaudhary and Ankit Negi which always relieved me from the workloads.

The financial support provided by University Grant Commission (UGC), Govt. of India is gratefully acknowledged.

I am forever indebted to my family for their support and faith in me, who have tolerated my protracted absences from home, especially during the past five years. I fill with the deepest sense of gratitude and exuberance of emotions in my heart whenever I think of my mother 'Smt. Kusum Lata'. She is a perfect example of ideal Indian woman and provided me the best care and shelter in this world. I salute her dedication and sacrifices that she made for our family. This acknowledgement would ring hollow without mentioning the name of my father 'Shri Prem Prakash'. I bow to my adorable father for his support and encouragement, not only to go complete this gigantic task but to have a pride to succeed in every walk of life. I acknowledge his sacrifices and love showered on me. Emotions of my heart should find new boundaries to contain my love for my loving brother Sudhanshu. His best wishes and motivation have been always with me during my whole Ph.D. My sincere and heartfelt thanks to two special people in my life, my elder sister Rovinsan and brother in law Mr. Jai Bhagwan whose selfless contribution in my life is deeply appreciated.

(RAVI PRAKASH)

LIST OF FIGURES

LIST OF TABLES

LIST OF PUBLICATIONS

A. Papers Published in Referred International Journals

1. "Improved resistive switching performance in Cu-cation migrated MoS_2 based ReRAM device incorporated with tungsten nitride bottom electrode"
   Ravi Prakash, Shubham Sharma, Anuj Kumar and Davinder Kaur
   Current Applied Physics, **19**, 260-265 (2019).

2. "Binder free and high performance of sputtered tungsten nitride thin film electrode for supercapacitor device"
   Ravi Prakash, Ashwani Kumar, Akhilesh Pandey and Davinder Kaur
   International Journal of Hydrogen Energy, **44**, 10823-10832 (2019).

3. "Pd capped W_2N nano porous thin films for remarkable room temperature hydrogen gas sensing performance"
   Ravi Prakash, Arvind Kumar and Davinder Kaur
   Sensors & Actuators: B. Chemical, **277**, 665-672 (2018).

4. "Effect of top electrode material on resistive switching properties of WN based thin films for non-volatile memory application"
   Ravi Prakash, Bhawani Pratap Singh Rathore and Davinder Kaur
   Journal of Alloys and Compounds, **726**, 693-697 (2017).

5. "Bipolar resistive switching behaviour in Cu/AlN/Pt structure for ReRAM application"
   Ravi Prakash and Davinder Kaur
   Vacuum, **143**, 102-105 (2017).

6. "Structural, corrosion and mechanical properties of sputtered deposited chromium tungsten nitride ($Cr_{1-x}W_xN$) nanocomposite thin films"
   Ravi Prakash, R. Jayaganthan and Davinder Kaur
   Advanced Materials Letters, **7 (9)**, 723-729 (2016).

7. "Effect of AlN layer on the resistive switching properties of TiO_2 based ReRAM devices"
   Bhawani Pratap Singh Rathore, **Ravi Prakash** and Davinder Kaur
   Current Applied Physics, **18**, 102-106 (2018).

8. "Growth and comparison of residual stress of AlN films on silicon (100), (110) and (111) substrates"
Akhilesh Pandey, Shankar Dutta, **Ravi Prakash**, R. Raman, Ashok K. Kapoor, and Davinder Kaur
Journal of Electronic Materials, **47**, 1405-1413 (2018).

9. "Effect of Mg content in $Ag/Zn_{1-X}Mg_XO/Cu$ structure for bipolar resistive switching performances"
Dibyaranjan Mallick, Rahul Barman, Kirandeep Singh, **Ravi Prakash** and Davinder Kaur
Advanced Material Letters, **9 (3)**, 153-157 (2018).

10. "Growth and evolution of residual stress of AlN films on silicon (100) wafer"
Akhilesh Pandey, **Ravi Prakash**, Shankar Dutta, Sandeep Dalal, R. Raman, Ashok K. Kapoor and Davinder Kaur
Materials Science in Semiconductor Processing, **52**, 16–23 (2016).

B. Paper Presented in National/International Conferences

1. "Effect of film thickness on structural and mechanical properties of AlCrN nanocomposite thin films deposited by reactive DC magnetron sputtering"
Ravi Prakash and Davinder Kaur
2nd International Conference on Condensed Matter & Applied Physics (ICC-2015) held at Govt. Engineering College, Bikaner, (India) during October 30-31, 2015.
AIP Conference Proceedings, **1728**, 020654 (2016).

2. "Effect of AlN Layer on the bipolar resistive switching behaviour in TiN thin film based ReRAM device for non-volatile memory application"
Ravi Prakash and Davinder Kaur
3rd International Conference on Condensed Matter & Applied Physics (ICC-2017) held at Ravindra Rangmanch, Bikaner, (India), November 24-25, 2017.
AIP Conference Proceedings, **1953**, 030262 (2018).

3. "Growth and morphological evolution of c-axis oriented AlN films on Si (100) substrates by DC sputtering technique"
Akhilesh Pandey, **Ravi Prakash**, Shankar Dutta, Sandeep Dalal, Anand Kumar, Ashok K. Kapoor, and Davinder Kaur
3rd International Conference on Condensed Matter & Applied Physics (ICC-2017) held at Ravindra Rangmanch, Bikaner, (India), November 24-25, 2017.
AIP Conference Proceedings, **1953**, 100028 (2018).

CONTENTS

Chapter 1

Introduction

CHAPTER 1

INTRODUCTION

1.1 Metal nitride materials

1.1.1 Metal nitrides

1.1.2 Overview of metal nitride thin film

1.1.3 Aluminum nitride (AlN)

1.1.4 Tungsten nitride (WN)

1.1.5 Chromium tungsten nitride ($Cr_{1-x}W_xN$)

1.2 Resistive switching behaviour

1.2.1 Overview of resistive switching

1.2.2 Literature survey

1.2.3 Resistive switching performance of metal nitride thin films

1.3 Hydrogen gas sensing

1.3.1 Overview of hydrogen gas sensing

1.3.2 Basic characteristics of gas sensor

1.3.3 Metal nitride thin films for hydrogen gas sensing application

1.4 Ternary metal nitride based thin films

1.4.1 Overview of ternary metal nitrides

1.4.2 General properties of ternary metal nitrides

1.4.3 Application of ternary nitride thin films

1.5 References

1.1 Metal nitride materials

1.1.1 Metal nitrides

Metal nitride (M_xN_y) is a class of chemical compound in which nitrogen is mixed with equal or lower electronegative metal. Metal nitride materials contain the nitride ion (N^{-3}) **[1]**. Interstitial alloys of nitrogen and early transition metal forms compound with metal-like character due to its similarity in the closed-packed crystal structures **[2-3]**. Indeed, metal nitrides are known for their ceramic-like behaviour when it comes to resistance against corrosion, high melting point and hardness, but metal or semiconductor like characters when it comes to electric and magnetic properties. Metal nitride materials can serve the following properties: Metallic to insulating, low to high thermal conductivity, absorption/emission bands from UV (ultraviolet) to visible range, positive to negative thermal expansion, soft to extreme hardness and paramagnetic to ferromagnetic behaviour **[4-6]**.

Metal nitride materials such as titanium nitride (TiN) and chromium nitride (CrN) are used as corrosion resistant and hard material **[7-10]**. Transition metal nitrides such as tungsten nitride (WN), vanadium nitride (VN) and molybdenum nitride (MoN) are used as catalyst due to exhibiting high surface area and tuneable electronic properties. Metal nitrides are utilized in superconducting solenoids, high-Q inductors, thin film miniature, Josephson junctions and bolometer. However, some metal nitrides are not chemically stable and thus can form ammonia and oxide/hydroxide of the metal after reacting with the water. The nitrides of vanadium, silicon, boron, titanium, tungsten, tantalum and aluminium are very refractory, hard in nature and shows resistance toward chemical attack **[6]**. Thus, metal nitrides are promising material for versatile applications due to its optical, electronic, thermal, mechanical and magnetic properties **[8, 11]**.

1.1.2 Overview of metal nitride thin films

Nowadays, metal nitride thin films play inevitable role in development of optical, decorative and corrosion resistance coatings, solar energy conversion devices and informatics quantum engineering **[7]**. The reason for the rise in importance of metal nitride thin films is ability to tune the properties according to application by optimizing their parameters. Undoubtedly, modification of most of the physical parameters of thin film such as structural, morphological, mechanical and optical properties play a vital role in an over widening sphere of scientific and technical applications.

In metal nitride thin films, the relative contents of metal and nitrogen are also accountable for the properties such as electrical property and surface morphology. Therefore, tuning the

electrical properties of thin films with nitrogen content is beneficial for the enhanced performance of electronic devices. However the surface morphology of thin film depends upon the film thickness and morphology of the substrate. The films with different surface morphology can provide a range of surface to volume ratio. Thus, it can be used for different applications such as gas sensing and catalyst. Metal nitride thin films possess high hardness, chemical inertness, good electrical properties and excellent wear resistance due to their bond structure i. e., mixture of covalent, metallic and ionic components. Therefore, metal nitride thin films are extensively used to improve the life span and performance of the tools. Among several metal nitride thin films, chromium nitride (CrN) thin film is extensively used in industry to coat cutting tools. Face-centred cubic (FCC) structured CrN thin film is the base material for advanced coatings such as chromium aluminium nitride (CrAlN) and chromium tungsten nitride (CrWN) **[12-15]**. Addition of another metal in CrN can enhance hardness, toughness, wear resistance and low friction. The most commonly used techniques to deposit the metal nitride thin films are chemical vapour deposition (CVD) and physical vapour deposition (PVD).

1.1.3 Aluminium nitride

Aluminium nitride (AlN) material has widespread applications as it reflects excellent properties such as high thermal conductivity, wide band gap (6.2 eV), better chemical stability, good electrical isolation and a high acoustic velocity **[16-19]**. AlN exhibits excellent field-emission property in vacuum microelectronic devices because of its small electron affinity value (0.6 eV). Thin films of AlN are utilized for surface passivation of insulators and semiconductors, optical devices in the ultraviolet spectral region and surface acoustic wave (SAW) devices **[20]**. AlN in its wurtzite phase is an extremely wide band gap (6.2 eV) semiconductor material which has potential applications in deep UV optoelectronics **[17, 20]**. AlN can withstand a very high temperature in inert atmosphere. In air, surface oxide layer of 5 - 10 nm on AlN thin film has been detected due to surface oxidation at temperature above 700 ˚C. Moreover, AlN is stable in H_2 and CO_2 atmospheres up to 980 ˚C. AlN with transition metal doping can find its application in multiferroic sprinonics due to its high curie temperature. The properties of AlN is listed in **Table. 1.1**. The AlN thin film can be an important nanostructure for extending our knowledge on the potential applications. In general, AlN thin films can be deposited by various deposition techniques such as atomic layer deposition, cathodic arc evaporation, electron beam deposition and magnetron sputtering **[18, 19]**. Among these deposition techniques, the magnetron sputtering have the advantage of uniform deposition, low temperature process, large area deposition etc. In

sputtering, the metastable cubic AlN can transformed into hexagonal AlN easily with the progress of nitrogen gas flow.

Table 1.1 Properties of aluminium nitride material.

Chemical Formula	AlN
Density	3.3g/cm^3
Colour	Black
Structure	Cubic/Hexagonal
Melting point	>2200 ˚C
Boiling point	2517 ˚C
Hardness	12.5 GPa
Elastic modulus	310 Gpa
Compressive strength	1000 MPa
Thermal conductivity	140-177 Wm^{-1}k^{-1}
Refractive index	2.11
Dielectric constant	8.8 @ 1MHz
Band gap	6.2 eV
Resistivity	>10^{10} ohm-cm

In cubic AlN, the nitrogen distribution is cubic and closely packed. Hexagonal AlN phase is achieved via crystalline transition of metastable cubic AlN. The crystal structure of wurtzite AlN is shown in **Fig. 1.1**

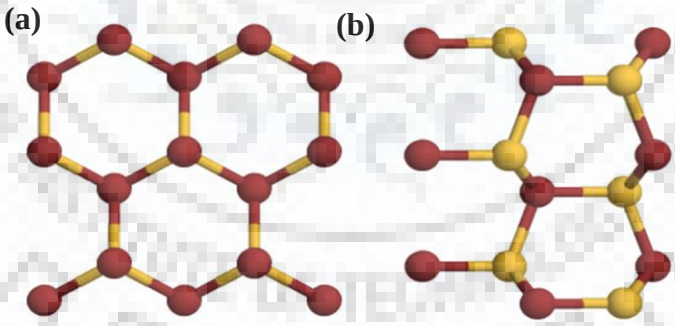

Figure 1.1 The crystal structure of wurtzite AlN, **(a)** top view, **(b)** side view. Red spheres are aluminium and yellow spheres are nitrogen.

1.1.4 Tungsten nitride (WN)

Tungsten nitride (WN) thin films have emerged as very promising applicant in various fields such as engineering, microelectronics and aeronautics. It exhibits good electrical property along with better mechanical and chemical stability due to highly directional nature of the metal non-metal p-d hybrid bonding **[21-24]**. Its potential applications are electrode in semiconductor devices and diffusion barrier, which can reduce the intermixing of active material with metalized

contact in microelectronics **[25-27]**. Compared to other metal nitrides, electrical resistivity of WN single crystal is lowest and does not reacts with copper, indicating its suitability as a barrier material. WN exhibits a higher work function and is widely used as the metal gate of p-channel bulk MOS field effect transistors (MOSFETs). Recent study shows that the tungsten nitride with W_2N phase is a good electro-catalyst for oxygen reduction reaction **[28]**. WN thin film has also been investigated as a gate metal for III–V based field-effect transistors and hard wear resistant protective coatings for cutting tools **[29, 30]**. There have been various studies that reports basic material properties of WN films such as, crystalline structure, resistivity, residual stress effects of nitrogen composition and thermal stability **[26]**. The properties of WN thin films are summarized in **Table 1.2.**

Table 1.2 Properties of tungsten nitride material.

Chemical Formula	WN
Density	17.8g/cm^3
Colour	Gray
Structure	Cubic
Melting point	~800 ˚C
Boiling point	2517 ˚C
Hardness	29-39 GPa
Elastic modulus	300-390 Gpa
Molecular mass	197.8467
Resistivity	>1322-2438μ ohm-cm

WN thin films with various phase and structure have been reported in literature. The WN thin films can have three different phases; cubic W_2N, hexagonal and tetragonal WN, rhombohedral WN_2 according to different nitrogen content. Among all the phases, W_2N phase is the most equilibrium phase with cubic structure which has favourable thermodynamic conditions. The cubic W_2N crystal structure is shown in **Fig. 1.2 [28]**. This phase exhibits high hardness at room temperature with low content of nitrogen.

In literature, several deposition techniques have been deployed to deposit WN thin films **[23, 27, 30]**. Each deposition technique with its related parameters, yield films of different properties, since optical and electrical properties strictly depend on their stoichiometry, microstructure and nature of impurities present. Magnetron sputtered deposited WN thin films requires optimization of parameters such as nitrogen partial pressure, deposition pressure and substrate temperature for better performance. In contrast, the work on oxidation kinetics,

electrical and optical properties of WN thin film upon their stability towards extreme environmental conditions, is still comparatively limited.

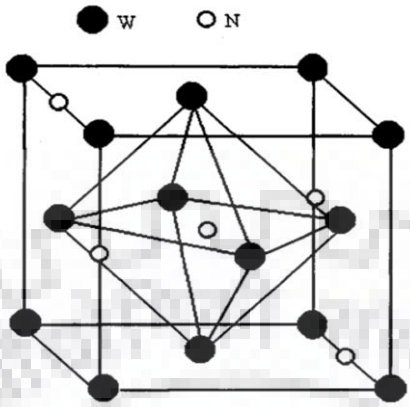

Figure 1.2 Crystal structure of the tungsten nitride.

1.1.5 Chromium tungsten nitride (CrWN)

CrWN is a ternary compound system which is composed of CrN phase and solid-solution of tungsten (W) **[31-33]**. Ternary compound system provides the opportunity to modify parameters such as lattice constant, hardness, thermal expansion and corrosion stability for optimization of total performance **[31]**. CrWN is synthesized by alloying W in CrN matrix. $Cr_{1-x}W_xN$ thin films with small W content (x) provides high hardness of tungsten nitride (WN) along with the high toughness of chromium nitride (CrN) as reported by Hones *et. al.* **[34-36]**. In literature, focus is primarily on the relation between phenomenological properties e.g., surface morphology and mechanical properties of the $Cr_{1-x}W_xN$ thin film **[37-39]**. Only few reports deal with further important parameters such as binding energy, bonding character and lattice constant. The XPS study suggests that the properties of $Cr_{1-x}W_xN$ thin film are greatly influenced by variation in charge distribution between Chromium, tungsten and nitrogen ions **[35]**.

$Cr_{1-x}W_xN$ thin films exhibit the hardness ranging from 22 to 30 GPa **[40]**. The addition of W into CrN matrix increase the hardness, which is credited to the Hall-Petch effect as a result of crystal or grain size refinement. Moreover, formation of highly covalent bonded W-N secondary phase in CrN thin film is also responsible for high hardness **[34]**. Sputtered deposited $Cr_{1-x}W_xN$ thin films are extremely capable for industrial applications such as machine parts, sliding parts, cutting tools and hydraulic tools **[37-40]**.

1.2 Resistive switching behaviour

1.2.1 Overview of resistive switching

A current-voltage (I-V) hysteresis exhibits resistive switching behaviour when the resistance state switches between mainly binary states **[41, 42]**. Generally, the first resistance state is high resistance state (HRS) and the second is low resistance state (LRS). These resistance states corresponding to HRS and LRS are achieved by varying the applied voltage. The change in resistance state from HRS to LRS is called SET condition/process and the applied voltage is considered as SET voltage (V_{SET}) while the switching from LRS to HRS is called RESET condition/process and the applied voltage is called RESET voltage (V_{RESET}). The resistance state will change only if the applied voltage is high enough that of switching voltage (V_{SET} or V_{RESET}). Further increase in applied voltage does not affect the resistance state. Therefore, this non-volatile resistive switching behaviour can be utilized for non-volatile memory storage device application **[41]**.

A resistive switching memory cell is usually fabricated as a capacitor-like MIM structure which consist of resistive or an insulating material 'I' sandwiched between two metals 'M' **[42-44]**. The memory cell can be electrically switched between two or more different resistance states, after the initial electroforming process which is essential to activate the switching phenomenon. Formation/disruption of a conducting path across top and bottom electrode is accountable for resistive switching behaviour. The schematic of MIM structure is shown in **Fig. 1.3.**

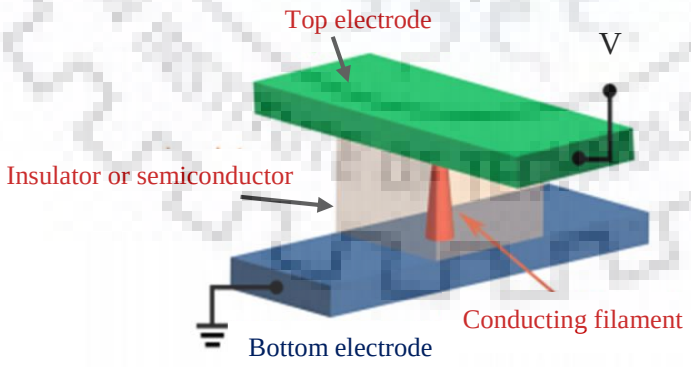

Figure 1.3 Schematic of MIM structure of resistive switching memory cell.

There are two type of resistive switching, first is unipolar resistive switching (URS) and other one is the bipolar resistive switching (BRS). In URS resistive switching, the state change is independent to the polarity of applied voltage **[45]**. If SET condition takes place under particular voltage polarity, the RESET condition can occur under both voltage polarities. Thus,

for the URS, the amplitude of applied voltage is more important rather than the polarity of applied voltage. In BRS operation, the amplitude and as well as polarity of applied voltage play a very significant role. Therefore, the SET and RESET switching in BRS takes place at opposite voltage to each other **[44-46]**. If the SET switching occurs under one specific voltage polarity, the following RESET switching will takes place under the voltage with opposite polarity unlike the URS. Schematic of I-V characteristics of the URS and the BRS are illustrated in **Fig. 1.4.**

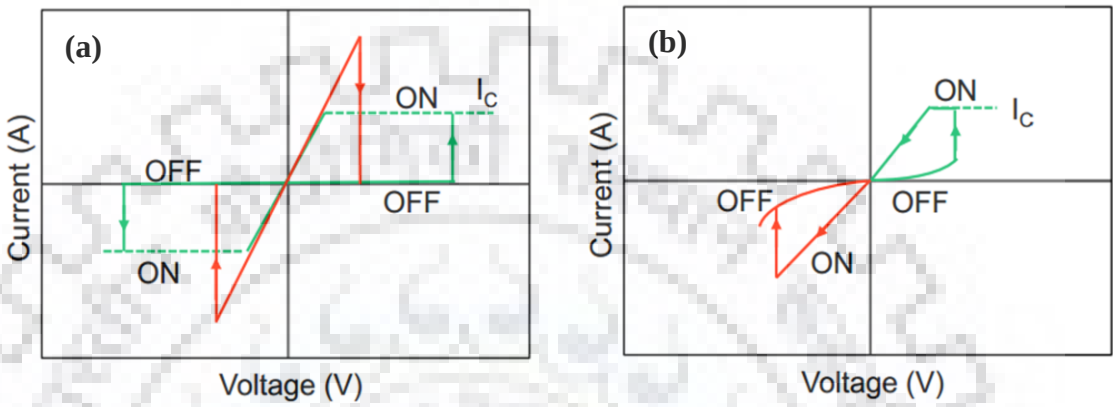

Figure 1.4 I-V characteristics of **(a)** unipolar switching and **(b)** bipolar switching.

Compliance current (I_C) is also an important parameter in resistive switching operation. During SET switching, the current abruptly increases and the switching cell may undergo a permanent dielectric breakdown without applying compliance current. Therefore, I_C protects the switching cell from electrical damage during the SET switching. In RESET switching, the I_C used for SET process can be deactivated as the RESET current (I_{RESET}) is normally greater than the I_C **[47].**

1.2.2 Literature survey

Although, the resistive switching property was discovered and identified in metal oxides in the early 1960s. Hickmott and Hiatt at General Electric and Gibbons and Beadle at Stanford University were the first to report the hysteretic resistive switching phenomenon **[48, 49]**. However, the resistive switching memories are passionately studied after 1990s for application in next generation solid state memories. Resistive switches were also being considered for more than Moore scaling. Therefore, the physical mechanism behind restive switching attracted great attention from scientific community. The initial study on resistive switching and its discussions was presented in a review by Dearnaley, Stonehom and Morgan **[50]**. The research in 21st century on resistive switching was triggered by Akihito Sawa et. al. **[51]**. In the early 2000s, resistive switching was thought as a possible candidate for conventional complementary metal oxide semiconductor (CMOS) technology with nanoscale crossbar circuits and novel computing

architecture applications. After that, some researchers demonstrated resistive switching behaviour in various oxides. The reported switching devices had operating voltage below 3V, programming current around 2 mA with 10^6 cycles of endurance **[51]**. Ever since, resistive switching has become one of the hottest research topics in both academia and industry for non-volatile resistive random access memory (ReRAM) application. Resistive switching behaviour of various materials are extensively studied for their non-volatile memory application due to its scalability, fast switching speed, 3D integrability, low power consumption, long retention time and CMOS compatibility. Resistive switching characteristic of large variety of metal oxides as well as other dielectrics such as some metal-nitrides, sulphides, fluorides, carbides and phosphides are thoroughly investigated **[52-55]**.

1.2.3 Resistive switching performance of metal nitride thin films

Metal nitride thin films are known to exhibit many excellent features such as good electrical properties and high thermal conductivity for resistive random access memory application. Hong. et. al. have reported resistive switching behaviour in aluminium nitride (AlN) thin film **[55]**. Furthermore, some researchers have recently reported the resistive switching behaviour of metal nitride thin films such as CuN, WN and ZrN, all of which demonstrate low voltage operation and full compatibility with CMOS technology along with prevention of surface contamination during device processing **[54, 56]**. These studies exhibit a low voltage/current operation and full compatibility CMOS technology as compared to oxide thin films. Resistive switching behaviour and exact physical mechanism in metal nitrides have not been fully investigated yet. Therefore, still it is an attention-grabbing subject to search for adequate methods to improve resistive switching performance of metal nitride thin films as well as to inspect their working mechanism.

1.3 Hydrogen gas sensing

1.3.1 Overview of hydrogen gas sensing

Recently, research of futuristic clean fuel has been going on with tremendous speed. The futuristic fuel should be abundant in nature and efficient with zero hazardous emission. Hydrogen (H_2) can perfectly fulfil the criteria required for such fuel. For example, NASA has been using H_2 gas to launch the space shuttles and liquid H_2 for launch the rockets since past three decades. H_2 gives the advantage of being eco-friendly fuel as the by-products are O_2 and water on combustion. Monitoring of H_2 content in molten metal is required to restrict the porosity which created due to dissolved gas. Moreover, H_2 has a Lower Explosive Limit (LEL) of 4% in air,

which means the accumulation of 4% H_2 in air could be dangerous and even a small spark can burn the mixture. Thus, it become necessary to sense the presence of H_2 in environment to avoid from any explosion. Apart from the capability to detect the H_2 leakage, the gas sensor must identify low level ambient sources of H_2 which can be beneficial for H_2 production. Safety during storage has become prior concern in all aspects of sensing H_2 leaks **[57]**. As H_2 gas is an odourless and colourless gas, therefore its detection is almost impossible without using any sensor. Hence, the dependence on sensors is an imperative alternative that allows H_2 concentration to be precisely measured.

1.3.2 Basic characteristics of gas sensors

The performance of a sensor is mainly characterized by following five parameters as: (i) Sensor Response (ii) Sensitivity (iii) Selectivity (iv) Response and recovery time (v) Long term stability and reproducibility which are defined below:

(i) Sensor Response (S.R.)

During gas sensing, the surface reaction would take place by adsorption and desorption of analyte gas molecules on top surface of the sensor and therefore the changes in electrical properties (resistance or conductance) are observed **[58]**. The sensor response of the sensor can be estimated by the following equation.

$$Sensor\ Response\ (\%) = \frac{R_a - R_g}{R_a} \times 100$$

where, R_a and R_g are the resistance in air and analyte gas respectively.

(ii) Sensitivity (S)

Sensitivity is defined as the rate of change of sensor response per unit change in gas concentration **[58]**. If 'C' is the target gas concentration, then mathematically it can be expressed as:

$$Sensitivity\ (\%) = \frac{R_a - R_g}{R_a * C} \times 10$$

(iii) Response and recovery time

The response time of gas sensor is defined as the required time to achieve the sensor signal up to atleast 90 % of the maximum constant signal at the time of adsorption of target gas

molecules. Though, the recovery time is the time required during desorption process to retrieve the sensor signal up to 10 % of the maximum stable signal.

(iv) Selectivity

Usually, the chemiresistive sensors are sensitive to many other interfering gases at same operating conditions. For gas sensors, the term 'selectivity' to analyte gas molecules is defined as the ratio of sensitivity for other interfering gas to sensitivity towards the target gas **[59]**.

$$Selectivity = \frac{Sensitivity\ of\ the\ sensor\ for\ interfering\ gas}{Sensitivity\ towards\ the\ desired\ gas}$$

(v) Long term reproducibility and stability

It refers to the ability of the device to retain its performance when performed constantly for a long time in harsh environment **[60, 61]**.

1.3.3 Metal nitride thin films for hydrogen gas sensing application

Nowadays, the thin film based chemiresistive gas sensors have attracted a notable attention of the researchers for sensing application owing to its low cost, high sensitivity towards various gases, fast response along with excellent reliability and compatibility. Basically, chemiresistive sensor is a transducer which can detect the gas molecules and responds into a measurable change in resistance. In chemiresistive sensor, the resistance of thin film changes sharply upon exposure to the target gas molecules on the surface of sensing element. It can be observed that the change in the resistance (or conductance) significantly depends on the type of thin film (either 'n' or 'p' type) and the nature of target gas (reducing or oxidizing). In order to design the chemiresistive sensors, various metal nitride thin films have been widely investigated. Metal nitride thin films have been developed as a potential candidate for realistic gas sensing applications due to their ease of use, a wide range of physical and chemical properties, simple fabrication process and robustness. Thin films of aluminium nitride (AlN), gallium nitride (GaN) and Indium nitride (InN) have been studied by the researchers for detection of hazardous gas species at low concentration level **[62-64]**. It has been reported that the performance of the gas sensor is noticeable enhanced when active sensing nanostructure are decorated with 0D catalytic noble metals (Pt, Pd and Au). These configurations can considerably change the surface as well as the electronic properties due to enhancement of the depletion layer at interface.

1.4 Ternary metal nitride based thin films

1.4.1 Overview of ternary metal nitrides

Ternary metal nitrides are of $M1_{1-x}M2_xN$ system, where M1 and M2 are different metals. These systems are achieved by alloying an appropriate metal into binary metal nitride matrix. The alloying of different metal in binary nitrides can lead to improved functionality as a consequence of fine tuning of the microstructure and properties of the final material. Generally, the ternary metal nitrides show a unique combination of refractory character, electron conductivity, chemical inertness, good wear resistance and high hardness. Thin films of ternary metal nitrides give the freedom to adjust the properties such as microstructure, corrosion stability and thermal expansion coefficient to enhance the all over performance. The composition of third element in ternary metal nitrides can be used to tailor the properties of system according to particular application.

TiN and CrN are widely used binary matrix to synthesize the ternary metal nitride by alloying another metal **[65-67]**. The technological advance in recent decades allowed the use of coatings at the nanometre scale for the improvement of functionality and endurance. Ternary metal nitride in the form of thin films are used as protection coatings, due the high hardness or for decorative purpose as they exhibit gold-like colour. Various thin film deposition techniques allow to coat ternary metal nitride thin film on every possible surface available.

1.4.2 General properties of ternary metal nitrides

Ternary metal nitrides have an incredible combination of features. These compounds are used as refractory materials due to high melting point (T_m) and chemical inertness and they can be stable in hostile environment. The excellent refractory performance is achieved due to partial occupation of bonding and anti-bonding states.

The electrical properties of ternary metal nitride can be also elucidated in terms of the valence electronic configuration of the composing metal. The mechanical properties of ternary metal nitrides are identical to that of ceramic materials, which feature high bulk modulus, high hardness and low plasticity **[68, 69]**. Presence of covalent bond between metals and nitrogen is responsible of above mentioned properties. Due to high directionality of covalent bonds give rise to a large bulk modulus which is an intrinsic property. Whereas the hardness of the material is the extrinsic mechanical property which depends on the microstructure.

1.4.3 Application of ternary metal nitride thin films

Ternary metal nitrides have been a part of main interest as they can afford a broad range of microstructure and are capable to retune the electronic and mechanical properties. Thus, ternary metal nitrides are utilized in industry, metallization, electronics and protective coating for cutting tools. Moreover, ternary metal nitride thin films provide multiphase structures which frequently results in distorted structures with high hardness. Recently, chromium nitride (CrN) based ternary systems has gained a significant attention as a hard protective coating for corrosion and wear protection.

Ternary metal nitride thin films are fabricated using by addition of a metals such as Aluminium (Al), Tungsten (W) and Zirconium (Zr) into binary metal nitride (e.g. TiN, MoN, CrN, SiN, etc.) **[69-73].** A number of research article have been reported on ternary nitride thin films fabricated using reactive co-sputtering of two metals [**32, 34, 71, 72].** The incorporation of other metal in Si_3N_4 and CrN results in a new nanocomposite film with potential application in field emission devices, anti-oxidation coatings, UV light emitters, glass molding and optical films **[65, 69, 70]**.

1.5 References

[1] https://www.britannica.com/science/nitride.

[2] Salamat A., Hector A. L., Kroll P., McMillan P. F., "Nitrogen-rich transition metal nitrides", *Coord. Chem. Rev*., **257**, 2063– 2072 (2013).

[3] Hultman L., "Thermal stability of nitride thin films", Vacuum, **57,** 1-30 (2000).

[4] Balogun M. S., Huang Y., Qiu W., Yang H., Ji H., Tong Y., "Updates on the development of nanostructured transition metal nitrides for electrochemical energy storage and water splitting", Materials Today, **20**, 8, **(**2017).

[5] Barnett S. A., Madan A., "Hardness and stability of metal–nitride nanoscale multilayers", *Scripta Mater.*, **50**, 739–744 (2004).

[6] Wittmer M., "Properties and microelectronic applications of thin films of refractory metal nitrides", *J. Vac. Sci. Technol. A*, **3**, 1797 (1985).

[7] Kim H., "Atomic layer deposition of metal and nitride thin films: Current research efforts and applications for semiconductor device processing", *J. Vac. Sci. Technol. B*, **21**, 2231 (2003).

[8] Ningthoujam R. S., Gajbhiye N. S., "Synthesis, electron transport properties of transition metal nitrides and applications", *Prog. Mater. Sci.*, **70**, 50–154 (2015).

[9] Martinez G., Shutthanandan V., Thevuthasan S., Chessa J.F., Ramana C. V., "Effect of thickness on the structure, composition and properties of titanium nitride nano-coatings", *Ceram. Int.*, **40(4)**, 5757-5764 (2014).

[10] Kostoglou N., Lukovic J., Babic B., Matovic B., Photiou D., Constantinides G., Ryzhkov V., Grossmann B., Mitterer C., Rebholz C., "Few-step synthesis, thermal purification and structural characterization of porous boron nitride nanoplatelets", *Mater. & Design*, **110**, 540-548 (2016).

[11] Ramana C. V., White S., Esparza N., Rangel V., Campbell A. L., "Crystal structure and morphology of nanocrystalline TiN thin films", *J. Elec. Mater.*, **41(11)**, 3139-3144 (2012).

[12] Sabitzer C., Paulitsch J., Kolozsvári S., Rachbauer R., Mayrhofer P. H., "Influence of bias potential and layer arrangement on structure and mechanical properties of arc evaporated AlCrN coatings", *Vacuum*, **106**, 49-52 (2014).

[13] Nunez O. R., Moreno T. A. J., Murphy N. R., Phinney L. C., Hossain K., Ramana C. V., "Physical characterization of sputter-deposited amorphous tungsten oxynitride thin films", *Thin Solid Films*, **596**, 160-166 (2015).

[14] Hollerweger R., Zhou L., Holec D., Koller C. M., Rachbauer R., Polcik P., Mayrhofer P. H., "Controlling microstructure, preferred orientation, and mechanical properties of Cr-Al-N by bombardment and alloying with Ta", *J. Appl. Phys.*, **119**, 065304 (2016).

[15] Wu W. Y., Wu C. H., Xiao B. H., Yang T. X., Lin S. Y., Chen P. H., Chang C. L., "Microstructure, mechanical and tribological properties of CrWN films deposited by DC magnetron sputtering", *Vacuum*, **87**, 209-212 (2013).

[16] Pandey A., Prakash R., Dutta S., Dalal S., Raman R., Kapoor A. K., Kaur D., "Growth and evolution of residual stress of AlN films on silicon (100) wafer", *Mater. Sci. Semicond. Process*, **52**, 16–23 (2016).

[17] Pandey A., Dutta S., Prakash R., Raman R., Kapoor A. K., Kaur D., "Growth and Comparison of Residual Stress of AlN Films on Silicon (100), (110) and (111) Substrates", *J. Elec. Mater.*, **47**, 1405-1413 (2018).

[18] Panda P., Ramaseshan R., Ravi N., Mangamma G., Jose F., Dash S., Suzuki K., Suematsu H., "Reduction of residual stress in AlN thin films synthesized by magnetron sputtering technique", *Mater. Chem. Physics.*, **200**, 78-84 (2017).

[19] Kim Y., Kim M. S., Yun H. J., Ryu S. Y., Choi B. J., "Effect of growth temperature on AlN thin films fabricated by atomic layer deposition", *Ceram. Int.*, **44**, 17447–17452 (2018).

[20] Fei C., Liu X., Zhu B., Li D., Yang X., Yang Y., Zhou Q., "AlN piezoelectric thin films for energy harvesting and acoustic devices", *Nano Energy*, **51**, 146–161 (2018).

[21] Shen Y. G., Mai Y. W., McKenzie D. R., Zhang Q. C., McFall W. D., McBride W. E., "Composition, residual stress, and structural properties of thin tungsten nitride films deposited by reactive magnetron sputtering", *J. Appl. Phys.*, **88**, 1 (2000).

[22] Baker C. C., Shah S. I., "Reactive sputter deposition of tungsten nitride thin films", *J. Vac. Sci. Technol. A*, **20**, 1699 (2002).

[23] Becker J. S., Gordon R. G., "Diffusion barrier properties of tungsten nitride films grown by atomic layer deposition from bis(tert-butylimido)bis(dimethylamido)tungsten and ammonia", *Appl. Phys. Lett.*, **82**, 2240 (2003).

[24] Addonizio M. L., Castaldo A., Antonaia A., Gambale E., Iemmo L., "Influence of process parameters on properties of reactively sputtered tungsten nitride thin films", *J. Vac. Sci. Technol. A*, **30(3)**, 031506 (2012).

[25] Wena M., Meng Q. N., Yu W. X., Zheng W. T., Mao S. X., Hua M. J., "Growth, stress and hardness of reactively sputtered tungsten nitride thin films", *Surf. Coat. Technol.*, **205**, 1953–1961 (2010).

[26] Mateusa R., Sequeira M. C., Porosnicu C., Lungu C. P., Hakolac A., Alves E., "Thermal and chemical stability of the β-W_2N nitride phase" *Nucl. Mater. Energy*, **12**, 462–467 (2017).

[27] Lee C. W., Kim Y. T., Min S. K., "Characteristics of plasma enhanced chemical vapour deposited tungsten nitride thin films", *Appl. Phys. Lett.*, **62 (25)**, 3312 (1993).

[28] Ozsdolay B. D., Mulligan C. P., Balasubramanian K., Huang L., Khare S. V., Gall D., "Cubic β-WN_x layers: Growth and properties vs N-to-W ratio", *Surf. Coat. Technol.*, **304**, 98–107 (2016).

[29] Polcar T., Parreira N. M. G., Cavaleiro. A., "Tribological characterization of tungsten nitride coatings deposited by reactive magnetron sputtering", *Wear*, **262**, 655–665 (2007).

[30] Samano E. C., Clemente A., Díaz J. A., Soto G., "Mechanical properties optimization of tungsten nitride thin films grown by reactive sputtering and laser ablation" , *Vacuum*, **85**, 69-77 (2010).

[31] Hsieh T. H., Zhu Y. J., Yu Z. H., Tang C. Y., Hsu C. H., Hsu C. Y., "Mechanical and tribological properties of CrWN nanostructured hard films", *J. Nanosci. Nanotechnol.*, **16**, 1–6 (2016).

[32] Chen Y. I., Cheng Y. R., Chang L. C., Lee J. W., "Chemical inertness of Cr–W–N coatings in glass molding", *Thin Solid Films*, **593**, 102–109 (2015).

[33] Chen G. C., Hu C. C., Wang C. H., Lu T. W., Hsu C. Y., "Direct current reactive co-sputter deposition of CrWN films to enhance cutting tool performance", *Int. J. Refract. Met. Hard Mater.*, **37**, 82–89 (2013).

[34] Wu F. B., Tien S. K., Lee J. W., Duh J. G., "Comparison in microstructure and mechanical properties of nanocomposite CrWN and nano layered CrN/WN coatings", *Surf. Coat. Technol.*, **200**, 3194 – 3198 (2006).

[35] Hones P., Diserens M., Sanjinés R., Lévy F., "Electronic structure and mechanical properties of hard coatings from the chromium– tungsten nitride system", *J. Vac. Sci. Technol. B*, **18**, 2851 (2000).

[36] Hones P., Sanjinés R., Lévy F., "Sputter deposited chromium nitride based ternary compounds for hard coatings", *Thin Solid Films*, **332**, 240-246 (1998).

[37] Wu F. B., Tien S. K., Lee J. W., Duh J. G., "Manufacture, microstructure and mechanical properties of CrWN and CrN/WN nano layered coatings", *Surf. Coat. Technol.*, **200**, 1514 – 1518 (2005).

[38] Lin C. H., Duh J. G., Yau B. S., "Processing of chromium tungsten nitride hard coatings for glass molding", *Surf. Coat. Technol.*, **201**, 1316–1322 (2006).

[39] Yau B. S., Chu C. W., Lin D., Lee W., Duh J. G., Lin C. H., "Tungsten doped chromium nitride coatings", *Thin Solid Films*, **516**, 1877–1882 (2008).

[40] Lin T. N., Han S., Weng K. W., Lee C. T., "Investigation on the structural and mechanical properties of anti-sticking sputtered tungsten chromium nitride films", *Thin Solid Films*, **529**, 333–337(2013).

[41] Waser R., Dittmann R., Staikov G., Szot K., "Redox-based resistive switching memories – nanoionic mechanisms, prospects and challenges", *Adv. Mater.*, **21**, 2632–2663 (2009).

[42] Pan F., Gao S., Chen C., Song C., Zeng F., "Recent progress in resistive random access memories: Materials, switching mechanisms, and performance", *Mater. Sci. Eng. R.*, **83**, 1–59 (2014).

[43] Chang T. C., Chang K. C., Tsai T. M., Chu T. J., Sze S. M., "Resistance random access memory", *Materials Today*, **19**, 5 (2016).

[44] Pan F., Chen C., Wang Z. S., Yang Y. C., Yang J., Zeng F., "Nonvolatile resistive switching memories-characteristics, mechanisms and challenges", *Prog. Nat. Sci. Mater. Int.*, **20**, 01−15 (2010).

[45] Atul T., Shukla A. K., Katiyar R. S., Ashok K., "Unipolar resistive switching in cobalt titanate thin films", *EPL (Europhysics Letters)*. **117(3)**, 37003 (2017).

[46] Misra P., Pavunny S. P., Sharma Y., Katiyar R. S., "Resistive switching and current conduction mechanisms in amorphous $LaLuO_3$ thin films grown by pulsed laser deposition", *Integ. Ferroelectrics*, **157(1)**, 47-56 (2014).

[47] Chen C., Yang Y. C., Zeng F., Pan F., "Bipolar resistive switching in Cu/AlN/Pt nonvolatile memory device", *Appl. Phys. Lett.*, **97**, 083502 (2010).

[48] Gibbons J. F., Beadle W. E., "Switching properties of thin NiO films", *Solid State Electronics*, **7**, 785-790 (1964).

[49] Hiatt W. R., Hickmott T. W., "Bistable switching in niobium oxide diodes", *Appl. Phys. Lett.*, **6**, 106 (1965).

[50] Dearnaley G., Morgan D. V., Stoneham A. M., "A model for filament growth and switching in amorphous oxide films", *J. Non-Crystal. Solids.*, **4**, 593-612 (1970).

[51] Sawa A., "Resistive switching in transition metal oxides", Materials Today, **11**, 28 (2008).

[52] Saini P., Singh M., Thakur J., Patil R., Ma Y. R., Tandon R. P., "Probing the mechanism for bipolar resistive switching in annealed graphene oxide thin films", *ACS Appl. Mater. Interf.*, **10(7)**, 6521-6530 (2018).

[53] Tseng Z. L., Chen L. C., Li W. Y., Chu S. Y., "Resistive switching characteristics of sputtered AlN thin films", *Ceram. Int.*, **42**, 9496–9503 (2016).

[54] Du X., Zhou Q., Yan Z., Zhou Y. N., Wu X., "The effects of oxygen plasma implantation on bipolar resistive-switching properties of copper nitride thin films", *Thin Solid Films*, **625**, 100-5 (2017).

[55] Hong S. M., Kim H. D., An H. M., Kim T. G., "Resistive switching phenomena of tungsten nitride thin films with excellent CMOS compatibility", *Mater. Res. Bull.*, **48**, 5080–5083 (2013).

[56] Kim H. D., An H. M., Sung Y. M., Im H., Kim T. G., "Bipolar resistive-switching phenomena and resistive-switching mechanisms observed in zirconium nitride-based resistive-switching memory cells", *IEEE Trans. Dev. Mater. Rel.*, **13**, 252 (2013).

[57] Kostoglou N., Tarat A., Walters I., Ryzhkov V., Tampaxis C., Charalambopoulou G., Steriotis T., Mitterer C., Rebholz C., "Few-layer graphene-like flakes derived by plasma treatment: A potential material for hydrogen adsorption and storage", *Micro. Meso. Mater.*, **225**, 482-487 (2016).

[58] Kumar D., Chaturvedi P., Saho P., Jha P., Chouksey A., Lal M., Rawat J. S. B. S., Tandon R. P., Chaudhury P. K., "Effect of single wall carbon nanotube networks on gas sensor response and detection limit", *Sens. Actuators B-Chem.*, **240**,1134-1140 (2017).

[59] Kostoglou N., Constantinides G., Charalambopoulou G., Steriotis T., Polychronopoulou K., Li Y., Liao K., Ryzhkov V., Mitterer C., Rebholz C., "Nanoporous spongy graphene: Potential applications for hydrogen adsorption and selective gas separation", *Thin Solid Films*, **596**, 242-249 (2015).

[60] Tripathy M. R., Joshi R., Mehra N. C., Kumar S., Tandon R. P., "Electrical conduction and gas sensing characteristics of $15Fe_2O_3$–5ZnO–$80TeO_2$", *Mater. Lett.*, **61(2)**, 585-587 (2007).

[61] Tyagi S., Batra N., Paul A. K., "Influence of temperature on reducing gas sensing performance of nanocrystalline zinc ferrite", *Trans. Ind. Inst. Metals*, **68(5)**, 707-713 (2015).

[62] Rahmana Md H., Thakur J. S., Rimai L., Perooly S., Naik R., Zhang L., Auner G. W., Newaz G., "Dual-mode operation of a Pd/AlN/SiC device for hydrogen sensing", *Sens. Actuators, B-Chem*, **129**, 35-39 (2008).

[63] Lee D. S., Lee J. H., Lee Y. H., Lee D. D., "GaN thin films as gas sensors", *Sens. Actuators B-Chem.*, **6989**, 1–6 (2003).

[64] Kryliouk O., Park H. J., Wang H. T., Kang B. S., Anderson T. J., Ren F., "Pt-coated InN nanorods for selective detection of hydrogen at room temperature", *J. Vac. Sci. Technol. B*, **23**, 5 (2005).

[65] Knotek O., Münz W. D., Leyendecker T., "Industrial deposition of binary, ternary, and quaternary nitrides of titanium, zirconium and aluminium", *J. Vac. Sci. Technol. A*, **5 (4)**, 2173 (1987).

[66] Huang L., Zou C., Xie W., Peng F., Shao L., "Influence of Si contents on the microstructure, mechanical and tribological properties of Cr–Si–N coatings", *Ceram. Int.*, **42**, 5062–5067 (2016).

[67] Shah H. N., Jayaganthan R., "Influence of Al contents on the microstructure, mechanical and wear properties of magnetron sputtered CrAlN coatings", *J. Mater. Eng. Perform.*, **21(9)**, 2002-2009 (2012).

[68] Abadias G., "Reactive magnetron co sputtering of hard and conductive ternary nitride thin films: Ti–Zr–N and Ti–Ta–N", *J. Vac. Sci. Technol. A*, **28**, 541 (2010).

[69] Veprek S., Zhang R. F., Veprek-Heijman M. G. J., Sheng S. H., Argon A. S., "Superhard nanocomposites: Origin of hardness enhancement, properties and applications", *Surf. Coat. Technol*., **204**, 1898–1906 (2010).

[70] Lin H. H., Chou C. C., Lee J. W., "Tribological properties of Cr–Si–N nanocomposite film adherent silicon under various environments", *Thin Solid Films*, **518**, 7509–7514 (2010).

[71] Sandu C. S., Sanjinés R., Benkahoul M., Medjani F., Lévy F., "Formation of composite ternary nitride thin films by magnetron sputtering co-deposition", *Surf. Coat. Technol.*, **201**, 4083–4089 (2006).

[72] Beliardouh N. E., Bouzid K., Nouveau C., Tlili B., Walock M. J., "Tribological and electrochemical performances of Cr/CrN and Cr/CrN/CrAlN multilayer coatings deposited by RF magnetron sputtering", *Tribol. Int.*, **82**, 443–452 (2015).

[73] Uhlmann E., Fuentes J. A. O., Gerstenberger R., Frank H., "nc-AlTiN/a-Si_3N_4 and nc-AlCrN/a-Si_3N_4 nanocomposite coatings as protection layer for PCBN tools in hard machining", *Surf. Coat. Technol.*, **237,** 142–148 (2013).

Chapter 2

Synthesis and Characterization Techniques

CHAPTER 2

SYNTHESIS AND CHARACTERIZATION TECHNIQUES

2.1 Introduction to thin film

2.2 Synthesis of thin film

- **2.2.1** Magnetron sputtering
- **2.2.2** DC magnetron sputtering
- **2.2.3** Reactive magnetron sputtering

2.3 Basic characterization techniques

- **2.3.1** X-ray Diffraction
- **2.3.2** Field emission scanning electron microscopy
- **2.3.3** Atomic force microscopy
- **2.3.4** Raman spectroscopy
- **2.3.5** X-Ray photoelectron spectroscopy

2.4 Measurement of electrical, electrochemical and mechanical properties

- **2.4.1** Current-Voltage (I-V) characteristics
- **2.4.2** Gas sensing measurements
- **2.4.3** Electrochemical potentiostat
- **2.4.4** Nanoindentation

2.5 References

2.1 Introduction to thin film

The thin films provide a large window of applications in several field such as electronics, optics, microwave, space science, information technology, communication, nanotechnology, sensors, defence and other commercial needs **[1-5]**. Therefore, a hike in thin film growth technology is observed. Thin films are formed due to abundantly homogenous growth of solid material in two (x, y) dimensions while restricted in remaining normal (z) direction. The film thickness (t) illustrates by the thickness of solid material along the (z) direction that can fluctuates between few micrometres to fractions of nanometres. To date, the manipulation of the thin films using various deposition techniques with desired thickness are utilized in micro miniaturized devices with controllable properties.

In this chapter, the synthesis of thin films and their characterization techniques which were used throughout the research work are discussed. First of all, the mechanisms of thin film growth are explained with details. Subsequently, the techniques which were involved for the thin films characterization for various applications are also described.

2.2 Synthesis of thin film

Synthesis process of thin film involves with nucleation of the species onto substrate and followed by coalescence and then thickness growth. These steps can be modified by the various deposition parameters **[6]**. Initially, synthesis process depends upon the interaction energy of thin film material and surface energy of the substrate. In nucleation, the islands of the atom or ions deliver a fraction or whole of its kinetic energy to the substrate and get adsorbed at the surface of the substrate. Vander-Waals or covalent bonds are responsible for sticking of the atoms or adatoms onto the substrate. Thin film growth takes place with the time after nucleation process. On the basis of surface energy term, there are three growth modes.

- **Layer by layer or Frank-van-der-Marwe mode: -** In this mode the interaction between adsorbate-adsorbate is less than the adsorbate-surface which results layers of material growth on top of one another as shown in **Fig. 2.1 (a)**. This growth requires a less lattice matching between the material and substrate.
- **Island or Volmer-Weber mode**: - This model involves the growth of "isolated island" on to the substrate surface due to a stronger interaction between adsorbate-adsorbate compared to adsorbate-surface as shown in **Fig. 2.1 (b)**.

- **Layer plus island or Stranski-Krastanov mode: -** This mode involves the layer (two dimensional) and island (three dimensional) growth simultaneously. It occurs when the interaction between adsorbate-surface is stronger than adsorbate-adsorbate. This mode consists of two steps in which, first the formation of two-dimensional layers and second is formation of three-dimensional islands upon layer as shown in **Fig. 2.1 (c)**.

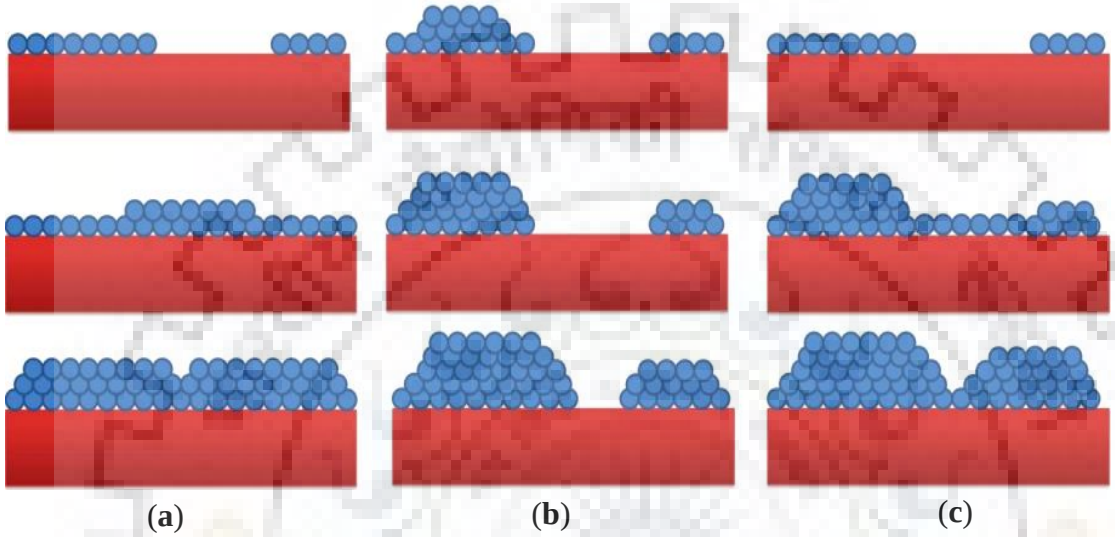

Figure 2.1. Schematic of the models for growth of thin films **(a)** Frank-ven-der-Marwe Mode, **(b)** Volmer-Weber Mode and **(c)** Stranski-Krastanov mode.

The above three growth modes can be explained in terms of surface energy using **Young's equation,**

$$\gamma_B = \gamma^* + \gamma_A \cos\phi \quad .$$

where γ_B is the surface energy of substrate, γ^* is the interface energy of film-substrate, γ_A is the surface energy of thin film material and ϕ is the wetting angle of a liquid nucleus on a substrate.

Layer to layer growth ($\phi = 0$) satisfies the $\gamma_B > \gamma^* + \gamma_A$ condition, whereas island growth ($\phi > 0$) requires $\gamma_B < \gamma^* + \gamma_A$. The Layer-plus-island growth takes place due to the increase in interface energy with film thickness; usually the top layer on the substrate is strained to fit the substrate **[2, 7]**. The schematic diagram of surface energy of substrate and thin film is shown in **Fig. 2.2**.

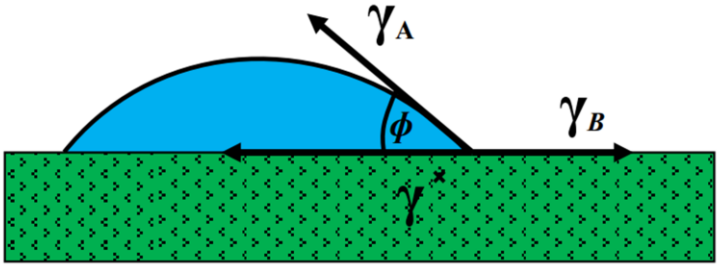

Figure 2.2. Schematic diagram of surface energy of substrate (γ_B), thin film material (γ_A) and interface energy of film-substrate (γ^*).

Thin film synthesis is a process in which a thin layer of material is applied onto the desired substrate that also called thin film deposition. The properties and performance of thin films are controlled by the purity of the material, deposition temperature, deposition rate, nature of substrate and deposition technique. There are two main techniques for thin film deposition, physical vapour deposition (PVD) and chemical vapour deposition (CVD). In PVD, initially the target material vaporized by physical means and then the vapour is transferred towards substrate surface after that vapour condensed onto the substrate and form a thin layer or thin film of the material. Since, in CVD techniques the material vaporized by chemical means. Each deposition technique having some additional advantages along with few disadvantages. The selection of deposition techniques depends upon the application and specific characterization of the thin film. In order to avoid contamination and free motion of particles, the deposition process performed in a vacuum chamber. A good vacuum inside deposition chamber ensured that the particle follow a straight path thus thin film deposition was found to be directional instead of conformal. PVD techniques provide a stoichiometric deposition but large area deposition is still a challenge. Among several PVD techniques the sputtering reflects many advantages along with any material can be deposited using suitable deposition modes. The advantages of sputtering technique are given as following:

(i) High uniformity during deposition.

(ii) Good adhesion of film onto substrate.

(iii) Easy deposition of materials with high melting points and high reactivity.

(iv) Better film thickness control.

(v) High deposition rate.

(vi) High flexibility of large-scale as well as complex geometry shape production.

(vii) Better reproducibility of deposited films.

In this present work, the metal nitride thin films were deposited using reactive magnetron sputtering which is a physical vapour deposition (PVD) technique. The following section describes the details about the sputtering process for thin film deposition.

2.2.1 Magnetron sputtering

Magnetron sputtering is a PVD technique which is widely used for fabricating a variety of thin films and coating from metal to insulator including semiconductor by erosion of the material from target surface **[8-13]**. Initially, the sputtering gas (here we used Argon gas) react with the cosmic electron in vacuum chamber and become argon ion, the reaction can be written as following,

$$A_r + e^- = A_r^+ + 2\,e^-.$$

The sputtering is caused by the bombarding of Ar ions onto target material and transferring the momentum to the target atoms. Therefore, some atoms come out from the surface and produced glow discharged plasma. **Fig. 2.3** shows the presence of different particles during sputtering process.

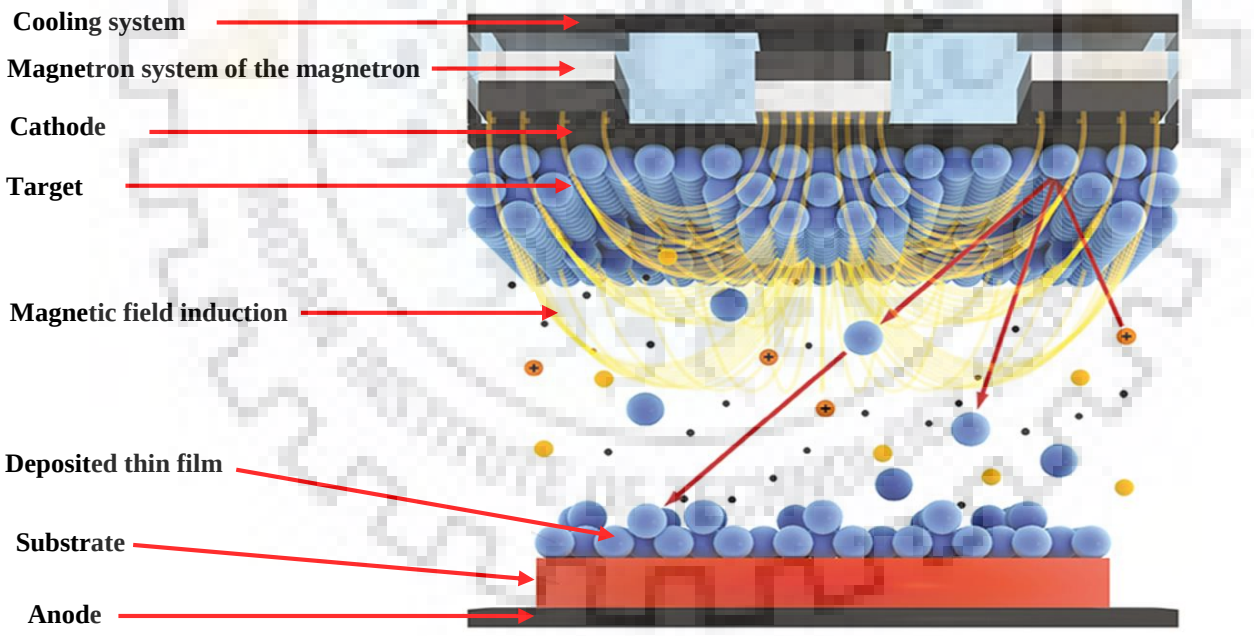

Figure 2.3 Schematic diagram of different particles involved in the magnetron sputtering process.

Due to ion bombarding on the target material, the secondary electrons also produced which helps in maintaining the continuous plasma. The arrangement of magnets in the magnetron are kept in such a way that one pole is placed on-axis to the target while second pole is designated around the outer edge of target in the form of a ring. This type of arrangement of magnets during

sputtering process constructs magnetic field parallel to the target surface, thus it restrict the motion of secondary electrons only in the territory of target. Moreover, the trapping of electron in an annular region near to target surface enhances the possibility to ionizing inert gas atoms. The enhanced ionizing capability causes a cascade of atom-electron collision which ensuing in dense plasma in front of the target. This accelerated process boosts ion bombardment on the target surface that resulting in higher sputtering rates and consequently, elevated deposition rates at the substrate.

Magnetron sputtering techniques ranges from radio frequency (RF) to direct current (DC) glow discharge sputtering. Another type of sputtering in which thin film deposition process performed in presence of a reactive gas called reactive magnetron sputtering. **Fig. 2.4** shows the schematic of DC/RF magnetron sputtering system in which more than one sputtering target can be sputtered on-axis or off-axis by placing sputtering guns inside the sputtering chamber.

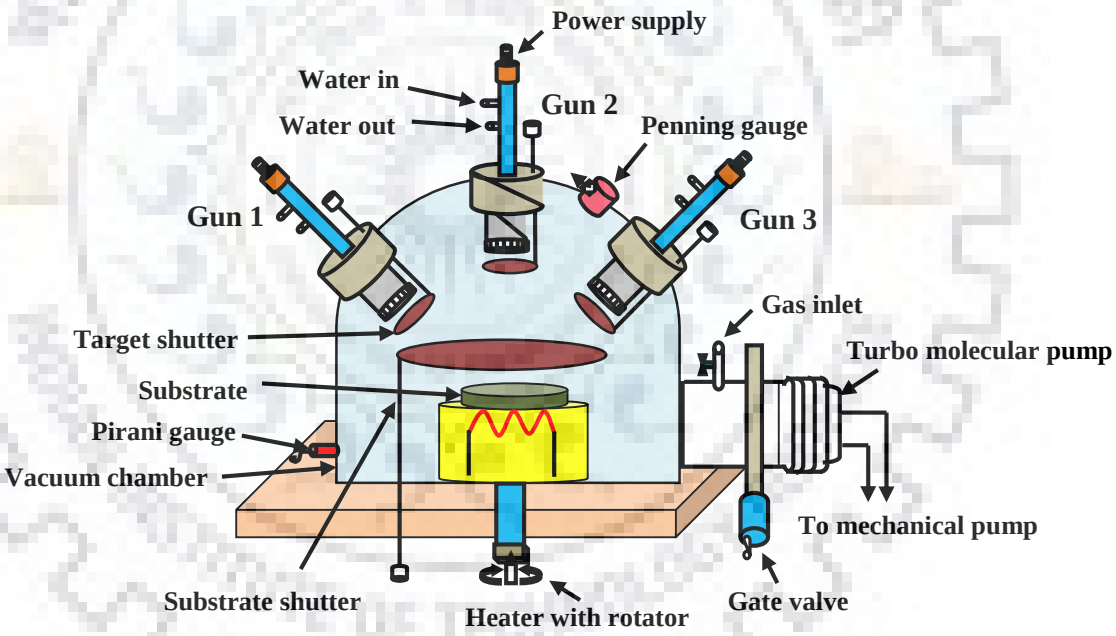

Figure 2.4 Schematic of the sputtering system.

2.2.2 DC magnetron sputtering

In DC sputtering technique a direct current bias was applied between cathode (target) and anode (substrate). Only metal and semiconductor targets can be sputtered using this technique. RF sputtering is used for depositing insulating thin films.

2.2.3 Reactive magnetron sputtering

Moreover, the reacting sputtering is used to deposit the thin films by chemical reactions between the target material and reactive gasses such as oxygen and nitrogen. The chemical reactions take place at the surface of substrate and where the reactive gas atoms inserted into target material matrix. For example, nitride based thin films synthesized by reactive sputtering in the presence of nitrogen and argon gas with different gas ratio. In our present work AlN, WN and $Cr_{1-x}W_xN$, thin films were deposited using reactive DC magnetron sputtering of respective targets.

Fig. 2.5 (a) shows the image of sputtering system assembled in our laboratory (Functional Nanomaterial Research Lab, Department of Physics, IIT Roorkee). **Fig. 2.5 (b)** shows the sputtering gun in which sputtering target was placed. The magnetron and developed plasma during sputtering process are depicted in **Fig. 2.5 (c)** and **Fig. 2.5 (d)** respectively.

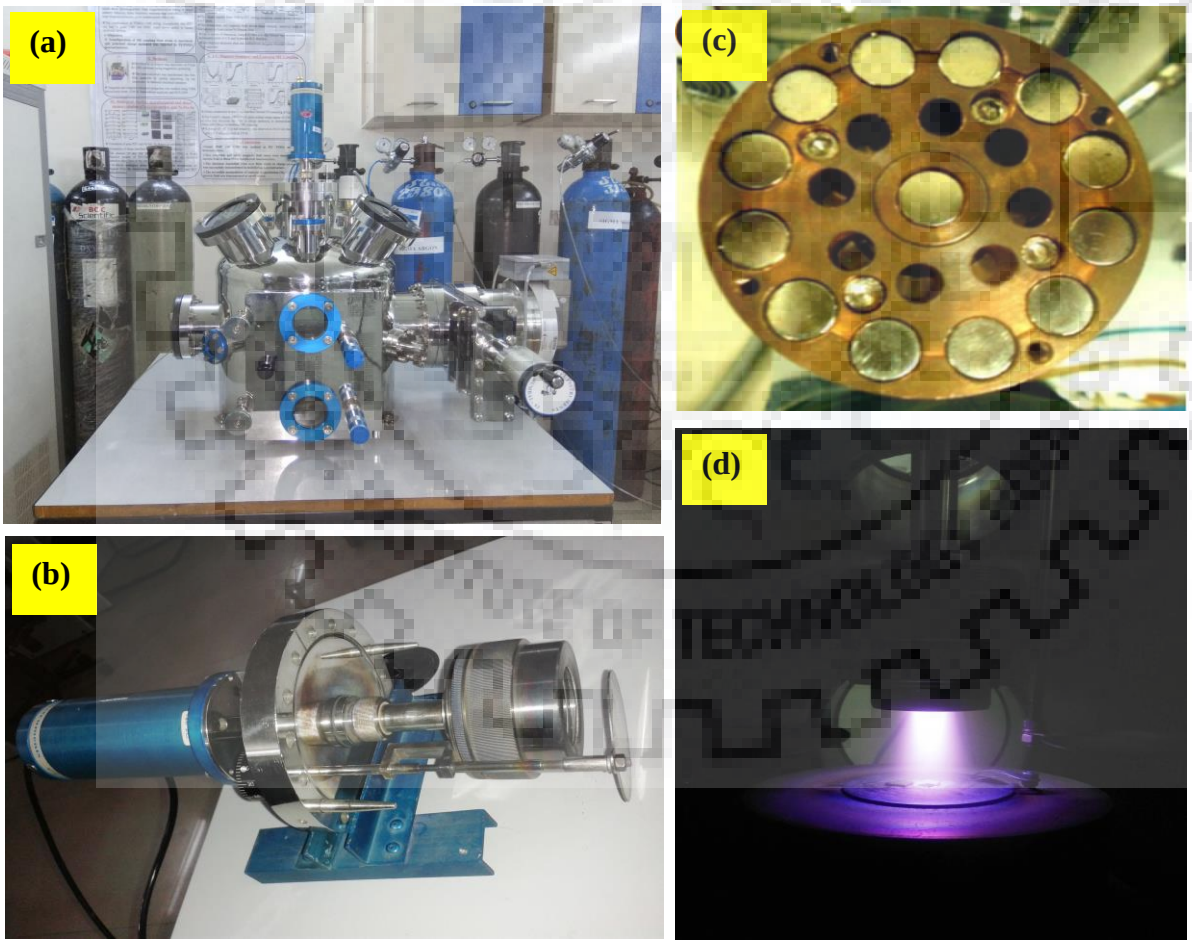

Figure 2.5 (a) Photograph of magnetron sputtering system assembled in our research laboratory, **(b)** Sputtering gun, **(c)** magnetron arrangement and **(d)** Plasma formation during sputtering process.

The vacuum pumps and pressure measuring gauges attached to the sputtering chamber are bought from Pfeiffer vacuum. The targets which were used for sputtering have the dimensions of 2 inch in diameter and 3-5 mm in thickness. Aplab high voltage DC power supply (50-1000 V, 0 - 1 A) was used for DC magnetron sputtering. For the deposition of thin films, the substrate such as silicon and porous silicon were fixed on a substrate holder, using silver paste and clips. A heater (Range: Room temperature – 1123 K) is also attached under the substrate holder. After substrates mounting, the chamber was evacuated with the help of a turbo molecular pump attached with a rotary pump up to relatively high vacuum of the order of $\leq 2 \times 10^{-6}$ Torr. After achieving required vacuum, an inert gas such as Argon (99.99% purity) was inserted into the deposition chamber through gas valve. The gate valve was kept nearly closed state (throttling) to maintain the incoming gas flux and pumping-out rate simultaneously. The inert gas pressure and flow rate inside vacuum chamber can remain stable by proper throttling. Then the negative potential was applied to the target and the sputtering process starts. During this process, the sputtered atoms get deposited on the substrate leading to thin film format.

2.3 Basic characterization techniques

2.3.1 X-ray diffraction

X-Ray diffraction (XRD) is considered as the widely used non-destructive technique for the identification of crystal structure, phase, orientation, lattice parameters and stress in a solid crystalline material **[14-18]**. X-Rays are electromagnetic radiations with wavelength ranging from 0.01 nm to 10 nm. As a monochromatic X-ray beam falls onto a crystalline material, the interference (constructive or destructive) from parallel planes of atoms with inter-planar spacing (d) takes place as Bragg's law is satisfied $2d \sin\theta = n \times \lambda$. Here n is integer which denotes the order of the reflection, θ is the diffraction angle between the incident ray and scattering plane also called as Bragg angle and λ is the X-ray beam wavelength **[19]**.

In a crystalline structure, the periodic arrangement of the atoms could be considered as scattering centres for X-Rays. The X-Rays could be easily diffracted by these atomic planes of crystal as their wavelength is comparable to the inter-planar spacing between the adjacent atomic planes which is of the order of few Å. Diffraction takes place between the waves as they encounter an obstacle whose dimension is comparable to their wavelength. If we consider a crystal structure with periodic arrangement of atoms as shown in **Fig. 2.6**, then there are two geometrical factors which are to be considered: firstly, the incident beam, the normal to the diffracting plane and the diffracted beam, all lie in a same plane. Secondly, the angle between the incident and the diffracted beam is always 2θ, which is the diffraction angle usually measured

experimentally. For an incident X-ray falling on a periodic structure making an angle θ with the plane, constructive interference for atomic planes of the crystal structure parallel to the sample plane takes place when the following condition is satisfied the Bragg equation.

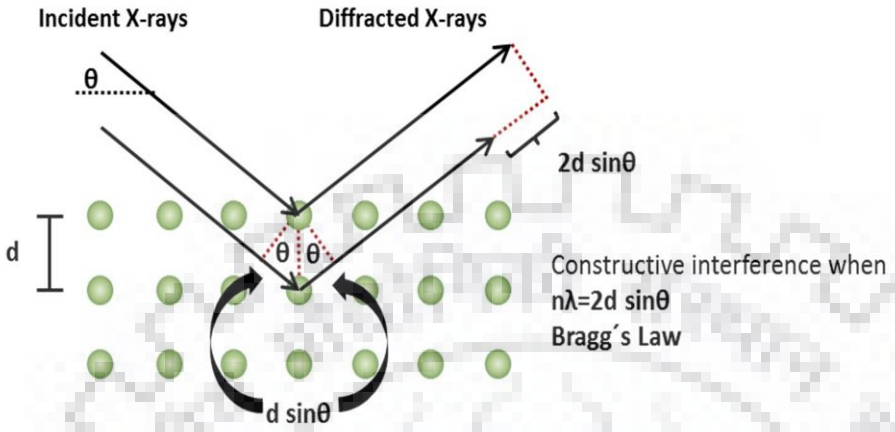

Figure 2.6 Schematic diagram for diffraction of X-Rays from a crystalline material.

The crystallographic information is realized by calculating inter planner spacing values and indexing of reflections. The characteristic diffraction pattern can be obtained for pure or doped material also. The Bragg's angle 2θ and intensities (I) are used to characterize the X-ray diffraction pattern. The angular position of lines depends on the inter planner spacing d of the lattice planes. For nanocrystalline materials, the crystallite size is a vital parameter that calculated from the width of the Bragg angle and is known as the Scherrer's formula **[19]**.

$$T = \frac{0.9\lambda}{\beta \cos\theta}$$

where, T is the crystallite size, β is the full width at half maximum (FWHM) of the Bragg angle on 2θ scale. However, subtract the instrumental line width from the measured line width to get an accurate result of broadening due to small particle size.

Fig. 2.7 (a) and **(b)** shows the schematic and photograph of Bruker D8 Advance X-ray Diffractometer, used in the present study to characterize the solid crystalline samples. Diffractometer, consists of an X-ray tube, an X-ray detector and a sample holder. The radiation of λ = 1.54 Å (Cu K_α) produced from the X-ray tube using copper target are collimated and focused onto the sample.

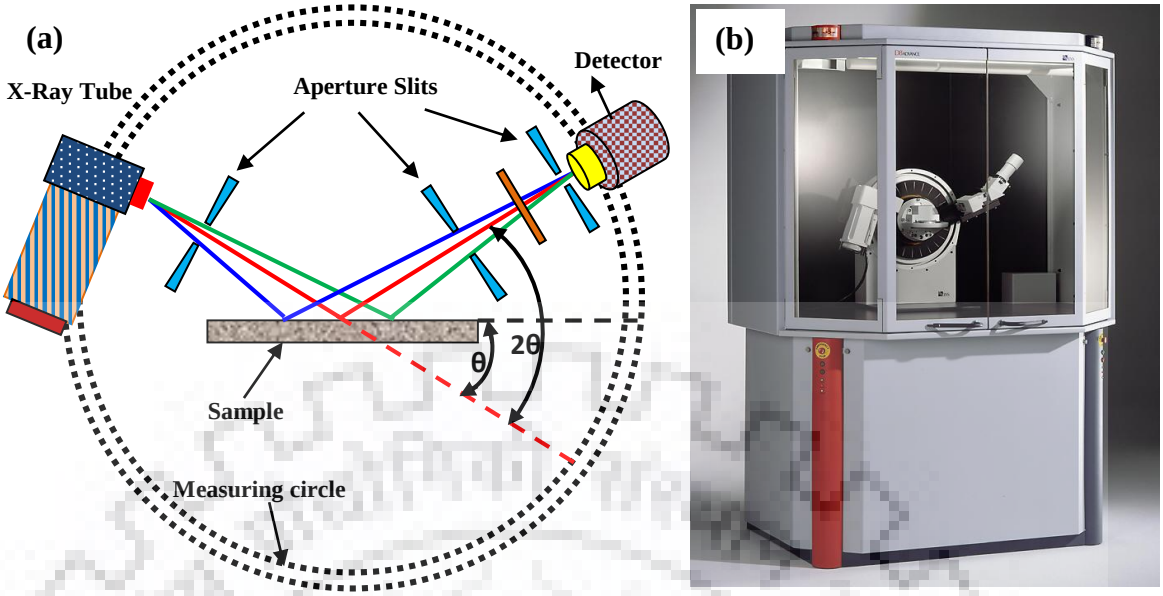

Figure 2.7 (a) Schematic diagram of beam path and **(b)** Photograph of Bruker D8 Advance X-ray Diffractometer.

The intensity of the reflected X-rays is measured with the rotation of the sample and detector. As the incident X-rays hit some appropriate set of parallel planes at Bragg's angle 'θ', satisfying Bragg equation, and then intensity peaks corresponding to constructive interference comes into picture. Suitable detector is employed to records diffracted X-rays that are further converted into appropriate signal and sent to printer or monitor as an output signal. The geometry of diffractometer allows sample to rotate in the path of the focussed X-ray beam at θ angle and the X-ray detector collects the signals and rotates at 2θ angle relative to the direction of incident X-ray beam. The hardware assembly used to control the angles and provide mechanism of rotation to the sample and detector which is called goniometer. NaI scintillation counter is used as detector in Bruker D8 Advance Diffractometer. It can detect the diffracted radiations for the wavelength which ranging from 0.5-3 Å. Monochromators are arranged in the path of X-rays to suppress the undesired part of X-rays. First aperture diaphragm is placed between specimen and tube to restrict the irradiated specimen area. A second aperture diaphragm is used to suppress scattered radiation coming from first aperture. The resolution of the signal is controlled by detector diaphragm.

2.3.2 Field emission scanning electron microscopy

Field emission electron microscopy (FE-SEM) is an adaptable and non-destructive technique for studying the morphology, microstructure and chemical composition of various materials by scanning it with a focused beam of electrons **[20]**. FE-SEM technique uses field

emission gun to produce clear images of the specimens, with spatial resolution < 2 nm. In present case the surface morphology of the deposited thin films was studied by field emission scanning electron microscope (FEI Quanta 200F model) with resolution of 2 nm and 80000X magnification. **Fig. 2.8 (a)** and **(b)** shows the schematic diagram of the optical column of FE-SEM and image of the FE-SEM setup respectively.

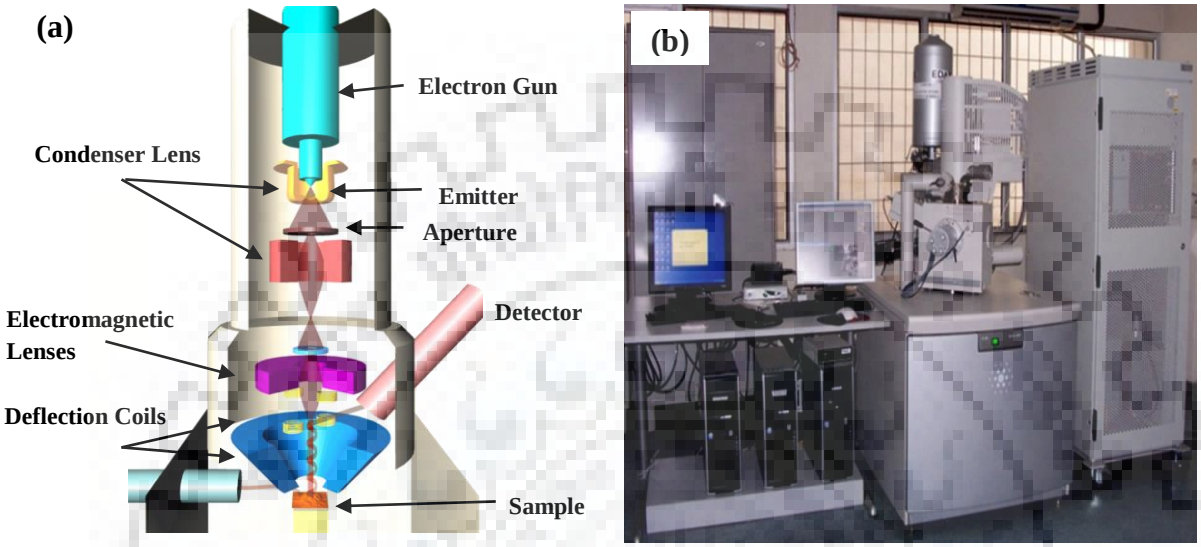

Figure 2.8 (a) Schematic diagram of FE-SEM and **(b)** Photograph of FE-SEM (FEI Quanta 200F).

The first part of FE-SEM is electron gun which produces electron beam, with an energy ranging from a few hundred eV to 50 keV by field emission. The Field emission gun (FEG) is mostly a wire of tungsten (W) shaped into a sharp tip of 100 nm radius. Using such a small radii tip, the electric filed can be concentrated to an intense level, therefore that work function of material can be lowered and electrons can leave the cathode. The electron beam emitted from the gun is focused with help of two condenser lenses into a very fine focal spot size beam. The two condenser lenses demagnify the electron beam until it hits the specimen surface. The first condenser lens helps to narrow the beam and also limit its current while second one makes the electron beam coherent and narrow. Finally, the objective lens focuses the beam onto thin film sample and then electron beam scans the specimen in the raster form.

The secondary or backscattered electrons emitted with certain velocity from the specimen's surface are attracted by the Corona, and then strike the scintillator (flourcent mirror) that produces photons. The intensity and location of illumination of the mirror varied and depending on the properties of the secondary electrons. This is due to the fact that greater is the number of secondary electrons that reach the detector, the higher is intensity in the image. The scintillator produces the final signal which is amplified and converted to a video signal. The

video signal is sent to a cathode ray tube to produce the image. The FE-SEM system also contains the energy dispersive x-ray analysis (EDAX) set up used for elemental composition analysis. The peaks observed in EDAX spectrum, represent different energy levels for which the most X-rays were received. Every peak is related to an atom therefore it corresponds to a particular element. The intensity of peak in a spectrum determines the concentration of element in the specimen.

2.3.3 Atomic force microscopy

Atomic force microscopy (AFM) is one type of scanning probe microscope which provides 3D profile of the surface at nanoscale by sensing the forces of interaction between the atoms belonging to the sample surface and the ones on the tip of the probe **[21]**. **Fig. 2.9 (a)** shows the schematic of AFM. In the present study, atomic force microscope from NT-MDT: NTEGRA was used and the photograph is shown in **Fig. 2.9 (b)**.

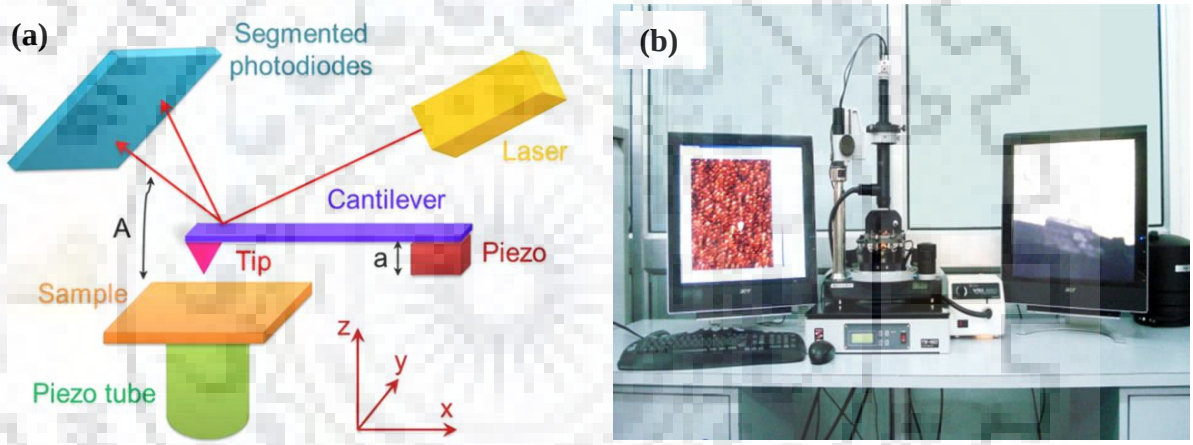

Figure 2.9 (a) Schematic diagram of AFM and **(b)** Photograph of AFM (NT-MDT: NTEGRA)

One of the advantages of the AFM compared to conventional microscopes such as the optical or scanning electron microscope is the capability to magnify in the x, y and z axis. A specially designed table to isolate mechanical and acoustical vibrations is required to perform high resolution (atomic scale) work. To image the surface features, the sample is scanned by an atomically sharp tip (< 10 nm), generally made of Si or Si_3N_4. This tip is fixed to the lower side of a reflective cantilever. Light from a diode laser is focused on the cantilever and reflected to a segmented photodiode. If the sample is scanned below the tip, the cantilever moves up and down which changes the ratio of light falling on the four elements of the photodiode. The difference in the intensity falling on the four elements is changed into a proportional voltage by the photodiode. This voltage acts as a feedback signal enabling the tip to manage either a constant force or a constant height over the sample. Then, the image of surface is reconstructed by observing the accurate motion of the probe as it is scanned over the surface.

2.3.4 Raman spectroscopy

In order to study vibrational, rotational and other low-frequency modes of a system Raman spectroscopy technique is used which is a non-destructive technique. Raman Spectroscopy technique is based on the Raman Effect, which is the inelastic scattering of photons by molecules. In 1924, Dr. C. V. Raman had discovered the fact that when a radiation of light incident on a chemical molecule, a fraction of the incident light is scattered by the molecule and its wavelength differs from that of the incident light**.** Photons interact with molecules and induce transitions between energy states. Most photons are scattered elastically and this process is called Rayleigh scattering. The emitted photons and absorbing photon have the same wavelength in Rayleigh scattering. In Raman scattering, the energies of the scattered photons and incident photon are found to be different. **Fig. 2.10 (a)** shows the schematic for a Raman scattering set-up.

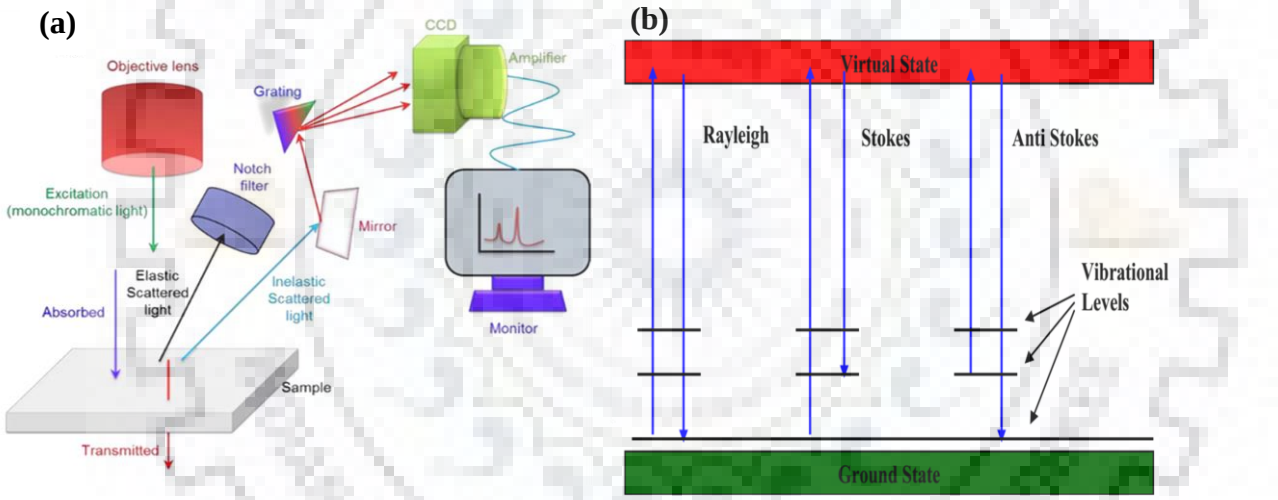

Figure 2.10 (a) Schematic of a Raman spectroscopy set-up and **(b)** Energy level diagram of Rayleigh scattering, Stokes Raman scattering and anti-Stoke Raman scattering.

The Raman spectra can be obtained by irradiating a sample with a powerful laser source or near infra-red monochromatic radiation. A spectrometer placed at some angle with the sample can collect the scattered radiation in a range of angles. The emitted radiation spectrum is of three types: Stokes, anti-Stokes and Rayleigh scattering as shown in **Fig. 2.10 (b)**. In Raman scattering, the incident light interacts with the molecule and polarizes the electron cloud around the nuclei thereby exciting the electrons to a short-lived virtual state. At room temperature, most of the molecules are in their lowest energy states. When the scattering occurs by electron cloud distortion, the photons are scattered with very small change in their frequency. Such kind of scattering process occurs due to elastic scattering and is most dominant in most of the

compounds. This scattering is known as Rayleigh scattering. However, when the scattering creates a nuclear motion, either the energy is transferred from the incident photon to the molecule (Stokes) or the molecule gives some energy to the scattered photon (anti-Stokes). This scattering process is inelastic and the energy of the scattered photon will differ by the energy of the incident photon by one vibrational unit. This is known as Raman scattering. The X-axis on a Raman spectrum is shift in wave number $\Delta\nu$, which is the difference in wave number of incident (source) and scattered (out coming) radiation **[22]**.

In the present study, Raman spectroscopy (Horiba Jobin Yvon Lab Ram HR 800 UV) was used for acquiring the Raman spectra of the samples at room temperature. The excitation source was an Argon ion laser with an excitation wavelength of 514 nm.

2.3.5 X-ray photoelectron spectroscopy

X-ray photoelectron spectroscopy (XPS) is a surface sensitive technique which can inspect the valence-state of atom/ion species at the solid surface. The XPS spectrum is obtained by irradiating monochromatic X-rays on the sample of known energy, under ultra-high vacuum and examines the energies of the emitted electrons from the occupied energy levels of the atoms/ions in the solid **[23]**.

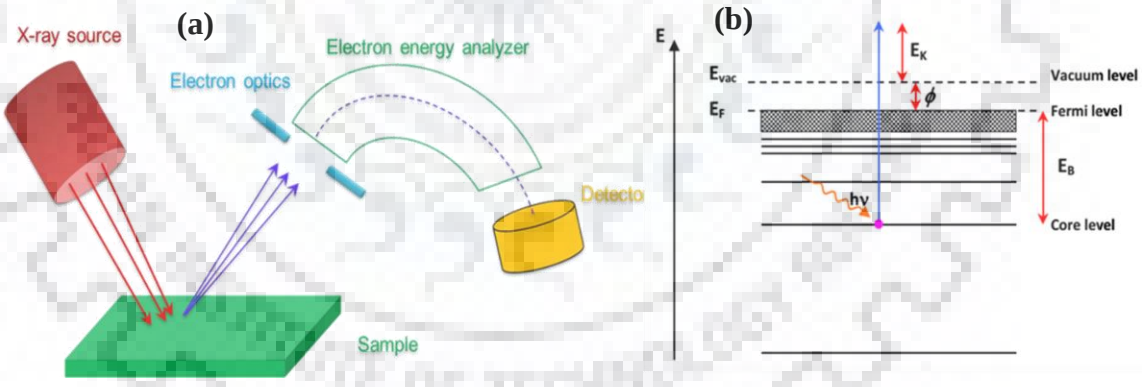

Figure 2.11 (a) Schematic of X-Ray photoelectron spectroscopy and **(b)** Energy core level diagram

Fig. 2.11 (a) shows a block diagram of XPS. To eject the photoelectron, the energy ($h\nu$, where h is the Planck constant and ν is the photon frequency) should be larger than the binding energy (B.E.) of a certain state of the atom/ion as shown in **Fig. 2.11 (b)**. The ejected electrons will have a kinetic energy, E_K

$$B.E. = h\nu - E_K - \varphi$$

where φ the work function, which is defined as the potential difference between the Fermi level of the solid and the vacuum level. In the present work, thin film samples were analysed using XPS (Perkin Elmer model 1257) spectrometer with Mg K_α X-ray source (hν=1253.6 eV) and the electron analyser set at a constant pass energy of 20 eV. The peak position of C 1s spectrum with a B.E. is equal to 284.6 eV, which is always present due to carbon contamination in small quantity on the sample surface which generally used for calibration purpose. The energy resolution of the spectrometer is 0.05 eV.

2.4 Measurement of electrical, electrochemical and mechanical properties

2.4.1 Current-Voltage (I-V) characteristics

In this study, the resistive switching properties were studied using Keithley 4200 Semiconductor Characterization System (SCS). The SCS is used for electrical characterization of semiconducting materials and devices as it can measure basic current-voltage (I-V) and capacitance-voltage (C-V). Ultra-fast pulsed I-V and transient I-V measurements can also be done using Keithley 4200 SCS **[24]**. For data collection, Microsoft windows based graphical user interface (GUI) is used that minimizes the set-up time during measurements.

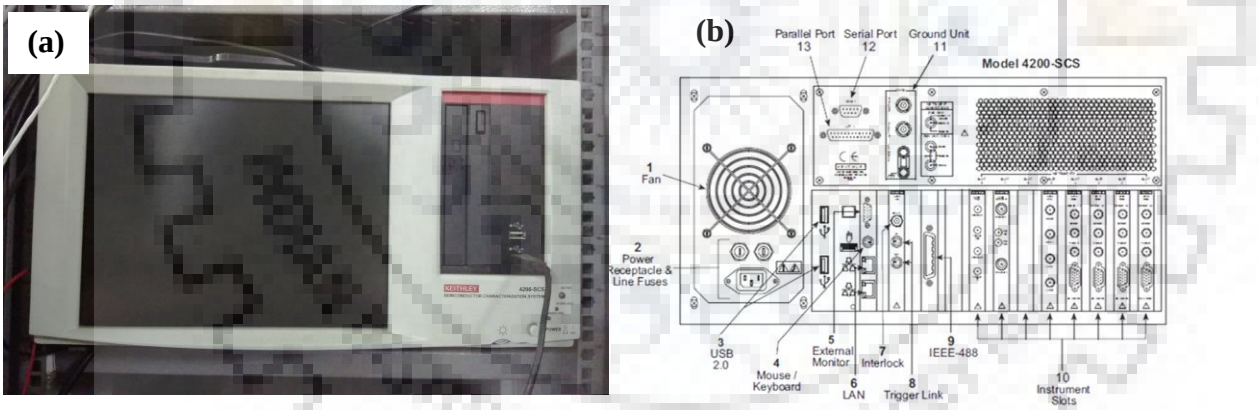

Figure 2.12 (a) The 4200 SCS showing interfaces in front panel and **(b)** The 4200 SCS showing interfaces in rear panel.

As shown in **Fig. 2.12 (a)** and **(b)**, Keithley 4200 SCS is installed with a large number of slots and interface ports that can connect to the computers with GPIB interface for further characterize the device. There are several USB ports in the front and at the back to connect flash drives or keyboards or any peripheral.

Fig. 2.13 shows the connections diagram for testing of a device with SMU (Source Measure Unit). One terminal of the device under test is connected to the Force of the SMU. Second terminal can be connected to the ground of the same SMU, or Force terminal of ground unit or Force terminal of another SMU.

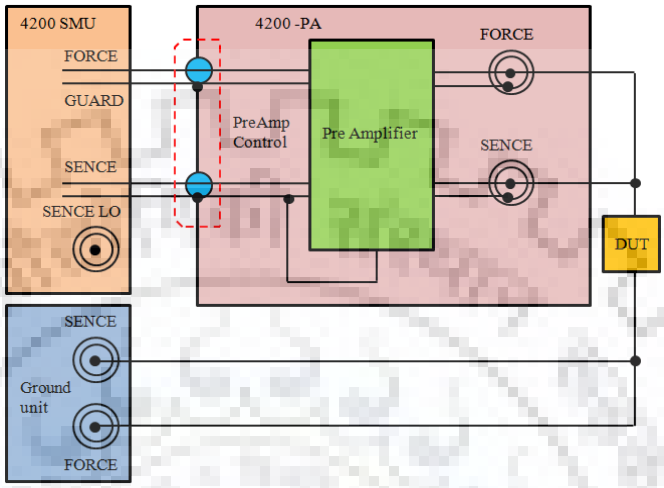

Figure 2.13: Connecting device under test (DUT) to SMU/Pre Amp.

All electrical measurement using 4200 SCS are performed using Keithley Interactive Test Environment (KITE) software. KITE is an interface with some built in sample projects which is very user friendly. This set up includes electrical characterization for the devices such as resistor, transistors, capacitors or MIM structures, FET, diode etc. The test results can be seen both graphically and numerically as the KITE software contains built-in long list of formulae for characterization and computation. 4200 SCS provides the liberty to control external instruments such as semiconductor probe stations, temperature controllers etc.

2.4.2 Gas sensing measurements

The custom-made sensing setup attached with a PID controlled electric heater of 500 cm^3 volume was used to carry out the sensing measurements and shown in **Fig. 2.14.** In setup, a vacuum chamber of stainless steel is equipped with one circular bottom heater with 800 °C maximum temperature. The samples are mounted on the heater surface using silver paste. Filling and draining of the gas insider sensing chamber were performed using two separate valves. In order to create the vacuum inside chamber a valve was opened to rotary pump. The top part of the measurement chamber has a dual gauge, which monitor the gas pressure and vacuum inside chamber. The volume of the measuring chamber is approximately 500 cm^3. Under the sample

holder a Kanthal Constantan thermocouple is used for the temperature measurement. Before introducing the sensing gas the chamber was evacuated to 6×10^{-1} Torr pressure.

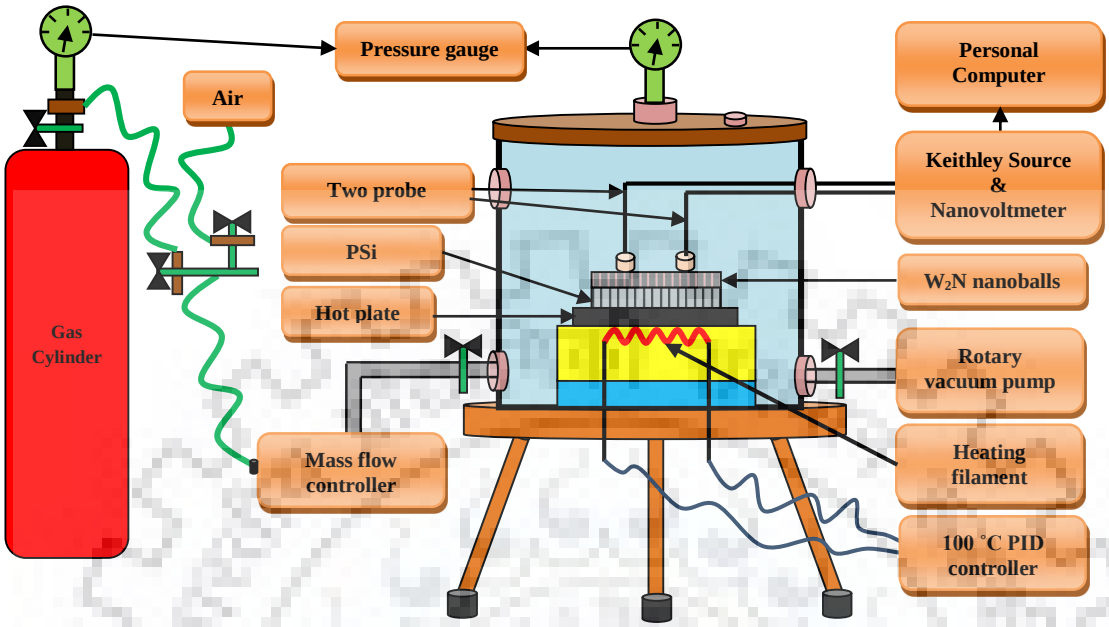

Figure 2.14 The schematic of hydrogen gas sensing set up.

Consequently, pure hydrogen (99.99 %) gas mixed with synthetic air (99.99 %) introduced at low rate of 50 cm^3/min into sensing chamber utilising mass flow controller at different humidity condition. Mass flow controllers were used to observe and control the flow of gases inside the sensing setup. An electrical feed-through, the top of the sample holder has been used for the electrical resistance measurement. In order to perform the in-situ gas sensing measurements, two probe resistivity technique was used along with Kiethley 2400 source meter and Kiethley 2181 A nanovoltmeter.

2.4.3 Electrochemical potentiostat

Electrochemical techniques widely used for the kinetics study of the electrochemical process in a specific environment **[25-27]**. The electrochemical measurements were performed in a 3.5 wt. % NaCl aqueous solution in double distilled water at room temperature by a Gamry instrument; model PCI 4, interface 1000 potentiostat as shown in **Fig. 2.15 (a)**. A corrosion cell with 0.79 cm^2 exposed area is used in which the electrolyte is exposed to thin film. There are three electrodes in which thin film operated as a working electrode, while a standard calomel electrode and a platinum rod acted as reference and counter electrodes, respectively as shown in **Fig. 2.15 (b)**.

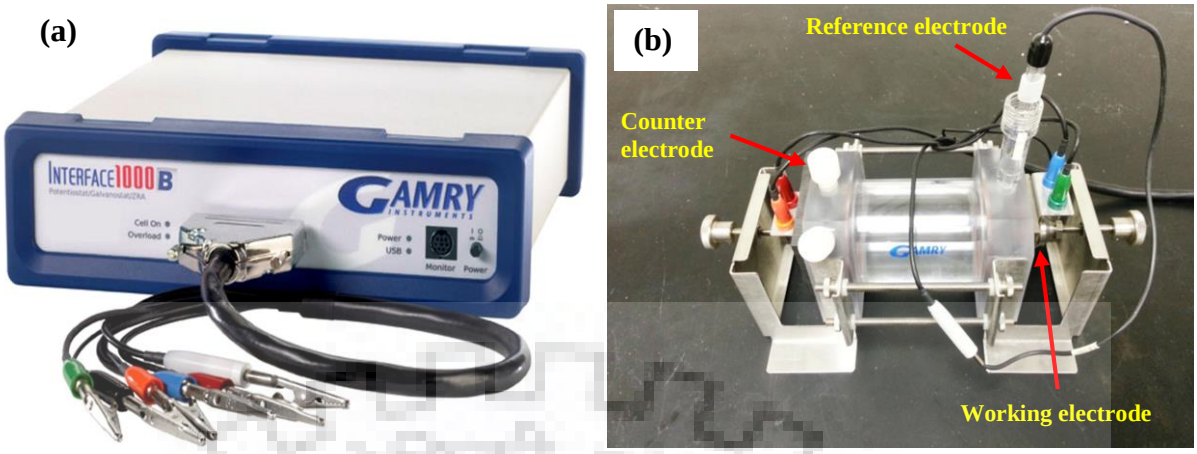

Figure 2.15 (a) Gamry instrument; model PCI 4, interface 1000 potentiostat and **(b)** Three electrode system for electrochemical measurements.

The types of electrodes used in CV are explained below:

(i) Reference electrode: The potential across the reference electrode remains constant such that it can be used as the reference standard for measuring the potentials of other two electrodes present in the electrochemical cell. The most frequently used reference electrodes for aqueous solutions are the calomel electrode and the silver/silver chloride electrode (Ag/AgCl).

(ii) Working electrode: During the experiment the electrochemical phenomena (reduction or oxidation) takes place at working electrode. In our experiments, the exposed part (in a circular shape) of deposited nanocomposite thin film samples was used as working electrodes.

(iii) Counter electrode: It acts as a source or sinks for electrons thus the current can be passed from external circuit through electrochemical cell. The potential of counter electrode is opposite in sign to that of the working electrode and neither its true potential nor current is ever measured or known. Commonly, it consists of a thin Pt/Au wire and sometimes graphite can be used.

The nanocomposite thin films were dipped in the solution for 2 hours until a constant open circuit potential (OCP) was reached. Potentiodynamic polarization test was then carried out with a scan rate of 1 mV/s. Diagrams for Tafel polarization curves were obtained at the voltage ranging from - 0.25 to + 0.25 V with respect to the OCP.

2.4.4 Nanoindentation

Nanoindentation is a powerful tool for measuring the mechanical properties of thin films **[28]**. Nanoindentation test includes indenting of a sample by a small load using a high precision instrument, which measures the load and displacement simultaneously.

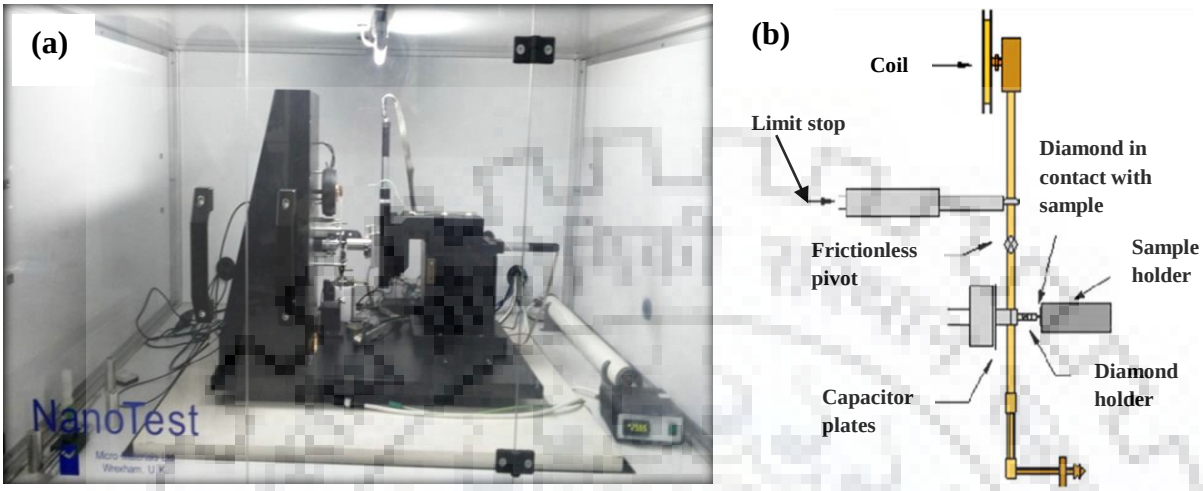

Figure 2.16 (a) Nanoindentation (Micromaterials, UK) **(b)** Schematic diagram of Nanotest system.

The load-depth curve along with the contact area of indenter versus the contact depth function determines hardness and elastic modulus. Nano Test system from Micro materials, Wrexham, U. K has been used in the present work as shown in **Fig. 2.16 (a)**. Nanoindentation is a pendulum-based depth sensing system where sample is mounted vertically and the load is applied electromagnetically as shown in **Fig. 2.16 (b)**. To rotate the pendulum on its frictionless pivot current is passed through the coil and the diamond probe penetrates the film surface. Test probe displacement (h) into the sample with the applied load (P) is measured during the loading and unloading with a parallel plate capacitor **[29]**. **Fig. 2.17** shows a load versus displacement curve in which the load is increased at a constant rate to a desired value (loading), held for a particular time period, and then decreased to zero (unloading). In this curve, h_{max} is the maximum loading depth, P_{max} is the maximum load, h_f is the final unloading depth, S is the slope of the tangent line of unloading curve at the maximum loading (h_{max}, P_{max}) point and h_c is the intercept value of tangent line down to P = 0 and also known as the contact depth. The (h_{max}, P_{max}) point is called the system contact stiffness. The film hardness (H) and reduced elastic modulus (E_r) can then be determined from this load-displacement curve. All data were analyzed with the Oliver and Phar method **[30]**.

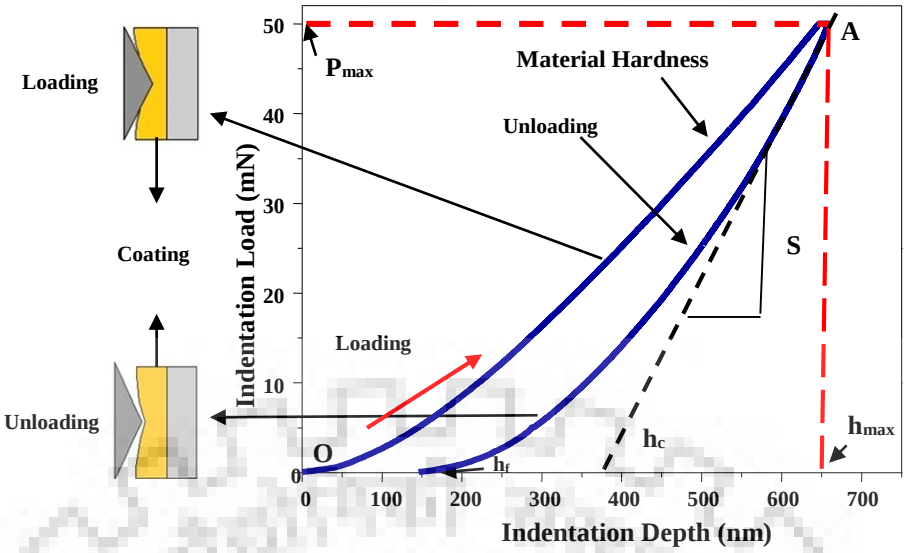

Figure 2.17 Load versus displacement curve.

In order to account for edge effects, the deflection of the surface at contact perimeter is estimated using geometric constant ε as 0.75. Area of contact at full load is measured by the depth of the impression and the known angle and radius of the indenter. The relation between load P and penetration depth h is,

$$P = k(h - h_f)^m.$$

where, k and m are power law fitting parameters related to geometric constants, elastic modulus and poison's ratio of the sample and indenter. The hardness (H) is a measure of a material's resistance to surface penetration by an indenter with a force applied to it and illustrated by the ratio of the maximum load P_{max} to the projected contact area A_c,

$$H = \frac{\in P_{max}}{A_c}.$$

where, $\in$ is constant depending upon the geometry of the indenter used. The reduced elastic modulus E_r is defined by the given equation,

$$\frac{1}{E_r} = \frac{(1-\nu_i^2)}{E_i} + \frac{(1-\nu_s^2)}{E_S}.$$

where, E_i, ν_i and E_s, ν_s are the elastic modulus and poisson ratio of the indenter and sample material respectively. For a diamond indenter probe, E_i is 1140 GPa and ν_i is 0.07 **[31].** The reduced elastic modulus takes into account the fact that elastic displacement occurs in both the thin film specimen and indenter. Reduced elastic modulus attributed by thin film only. The hardness of the thin film coating can be affected by the substrate also. Therefore, to avoid the

substrate influence the penetration depth should be limited to 1/10 of the total film thickness **[32-36]**. Thus, the film deformed by the indenter tip up to an elastic limit, as a result the indentation data measured the thin film properties with accuracy.

2.5 References

[1] West A. R., "*Solid state chemistry*", John willey & Sons, Singapore (2003).

[2] Chopra K. L., "Thin film phenomena", New York: McGraw-Hill (1969).

[3] Sharma G. N., Dutta S., Pandey A., Singh S. K., Chatterjee R., "Influence of nickel doping on structural, morphological and mechanical properties of $BiFeO_3$ thin films", *Mater. Chem. Phys.*, **216**, 47-50 (2018).

[4] Tyagi S., Baskey H. B., Agarwala R. C., Agarwala V., Shami T. C., "Synthesis and characterization of microwave absorbing $SrFe_{12}O_{19}/ZnFe_2O_4$ nanocomposite", *Trans. Ind. Inst. Met.*, **64(6)**, 607-614 (2011).

[5] Tyagi S., Baskey H. B., Agarwala R. C., Agarwala V., Shami T. C., "Development of hard/soft ferrite nanocomposite for enhanced microwave absorption", *Ceram. Int.*, **37(7)**, 2631-41 (2011).

[6] Kaiser N., "Review of the fundamentals of thin-film growth", *Appl. Opt*., **41**, 3053 (2002).

[7] Ohring M., "Materials science of thin films", Academic Press, New York (2006).

[8] Sahadevan A., Kalitsov A., Bhatia C. S., Velev J., Yang H., "Electric-field-induced magnetization changes in Co/Al_2O_3 granular multilayers", *Phys. Rev. B*, **87**, 014425 (2013).

[9] Lee W. C., Wang H. L., Wong M. S., "Phase transformation and structures of pure and carbon containing titania thin films annealed in air and in hydrogen", *Thin Solid Films*, **528**, 2-9 (2013).

[10] Peng C. J., Krupanidhi S. B., "Structures and electrical properties of barium strontium titanate thin films grown by multi-ion-beam reactive sputtering technique", *J. Mater. Res*., **10**, 708 (1995).

[11] Anders A., Brown J., "A plasma lens for magnetron sputtering", *IEEE T. Plasma Sci*., **39**, 2528 (2011).

[12] Shen S. J., Yang T. S., Wong M. S., "Co-sputtered boron-doped titanium dioxide films as photocatalysts", *Surf. Coat. Technol.*, **303**, 184-190 (2016).

[13] Wibowo E., Kwok C. Y., "Fabrication and characterization of sputtered NiTi shape memory thin films", *J. Micromech. Microeng*. **16**, 101 (2006).

[14] Yang Y. P, Wong M. S., "Structural and mechanical properties of annealed thin films of pure and carbon doped titania", *Surf. Coat. Technol.*, **259**, 129-35 (2014).

[15] Singh S. K., "Structural and electrical properties of Sm-substituted $BiFeO_3$ thin films prepared by chemical solution deposition", *Thin Solid Films*, **527**, 126-132 (2013).

[16] Sharma G. N., Dutta S., Pandey A., Singh S. K., Chatterjee R., "Microstructure and improved electrical properties of Ti-substituted $BiFeO_3$ thin films", *Mater. Res. Bull.*, **95**, 223-228 (2017).

[17] Jood P., Mehta R. J., Zhang Y., Peleckis G., Wang X., Siegel R. W., Tasciuc T. B., Dou S. X., Ramanath G., "Al-doped zinc oxide nanocomposites with enhanced thermoelectric properties", *Nano Letters*, **11(10)**, 4337-4342 (2011).

[18] Agrawal S., Raghuveer M. S., Kröger R., Ramanath G., "Electrical current-induced structural changes and chemical functionalization of carbon nanotubes", *J. Appl. Phys.* **100(9)**, 094314 (2006).

[19] Cullity B. D., "Elements of X-ray diffraction", 2nd Ed., Addison-Wesley Publishing Company (1978).

[20] Tarrant R., "The scanning electron microscope", Experiment 31, (2009-2011).

[21] https://en.wikipedia.org/wiki/Atomic_force_microscopy.

[22] Smith E., Dent G., "Modern raman spectroscopy—A Practical Approach", (2005).

[23] https://en.wikipedia.org/wiki/X-ray_photoelectron_spectroscopy.

[24] https://www.imperial.ac.uk/media/imperial-college/research-centes-and-groups/centre-for-bio-inspired-technology/7290999.PDF.

[25] Rajesh S., Sethy N. K., Bhargava K., Ilavazhagan G., Singh S. K., Karunakaran C., "Electrochemical sensor for simultaneous measurement of nitrite and superoxide anion radical using superoxide dismutase-mimetic manganese(III) tetrakis(1-methyl-4-pyridyl)porphyrin on polypyrrole matrix", *Sens. Lett.*, **9(5)**, 1682-1688 (2011).

[26] Castro L. T., Sepulveda M. A. A., Katiyar R. S., Manivannan A., "Electrochemical investigations on the effect of Mg-substitution in Li_2MnO_3 cathode", *J. Electrochem. Soc.*, **164(7)**, A1464 - A73 (2017).

[27] Sundarajan, T., Rajeswari, S., Subbaiyan M., Mudali U. K., Nair K. G. M., "Electrochemical studies on nitrogen ion implanted Ti_6Al_4V alloy", *Anti-Corros Method M.*, **45**, 162 (1998).

[28] Shaw G. A., Stone D. S., Johnson A. D., Ellis A. B., Crone W. C., "Shape memory effect in nanoindentation of nickel–titanium thin films", *Appl. Phys. Lett.*, **83**, 257 (2003).

[29] Nano test manual version P3, Micro Materials, Wrexham UK, September (2010).

[30] Oliver W. C., Pharr G. M., "An improved technique for determining hardness and elastic modulus using load and displacement sensing indentation experiments", *J. Mater. Res.*, **7**, 1564 (1992).

[31] Dhara S., Das C. R., Hsu H. C., Raj B., Bhaduri A. K., Chen L. C., Chen K. H., Albert S. K., Ray A., "Recrystallization of epitaxial GaN under indentation", *Appl. Phys. Lett.*, **92**, 143114 (2008).

[32] Oliver G. M., Pharr W. C., "Measurement of hardness and elastic modulus by instrumented indentation: Advances in understanding and refinements to methodology", *J. Mater. Res*., **19**, 3 (2004).

[33] Seshadri I., Esquenazi G. L., Tasciuc T. B., Keblinski P., Ramanath G., "Softening in silver-nanowire-filled polydimethylsiloxane nanocomposites", *Appl. Phys. Lett.*, **105(1)**, 013110 (2014).

[34] Bhardwaj V, Kumar A., Chowdhury R., Jayaganthan R., "Nanoindentation and nanoscratch behavior of ZnO: Pr thin films deposited by DC sputtering", *J. Mater. Res.*, **33(17)**, 2533-2544 (2018).

[35] Kumar N., Jayaganthan R., Brokmeier H. G., "Effect of deformation temperature on precipitation, microstructural evolution, mechanical and corrosion behavior of 6082 Al alloy", *Trans. Nonfer. Met. Soc. China*, **27(3)**, 475-492 (2017).

[36] Battu A. K., Ramana C. V., "Mechanical Properties of Nanocrystalline and Amorphous Gallium Oxide Thin Films", Adv. Eng. Mater., **1(0)**, 1701033 (2018).

Chapter 3

Growth and Characterization of AlN and WN Thin Films

CHAPTER 3

GROWTH AND CHARECTERIZATION OF AlN AND WN THIN FILMS

3.1 Bipolar resistive switching behavior in Cu/AlN/Pt structure for ReRAM application

- **3.1.1** Introduction
- **3.1.2** Experimental details
- **3.1.3** Results and discussion
- **3.1.4** Conclusions

3.2 Effect of top electrode material on resistive switching properties of WN based thin films for non-volatile memory application

- **3.2.1** Introduction
- **3.2.2** Experimental details
- **3.2.3** Results and discussion
- **3.2.4** Conclusions

3.3 References

3.1 Bipolar resistive switching behaviour in Cu/AlN/Pt structure for ReRAM application

3.1.1 Introduction

The conventional non-volatile memory storage technologies such as ferroelectric random access memory (FeRAM) and flash memory, are based on Si charge storage. In current digital era to achieve greater data storage, present memory technologies are required to be further scaled down. This requirement is facing a significant challenge due to technical and physical limitations, which also support by the well-known quote of Richard Feynman, "There is not plenty of room at the bottom anymore". A resistive random access memory (ReRAM) with a Metal-Insulator-Metal (MIM) structure could be pledged as next generation non-volatile memory. The MIM structure based ReRAMs reflect the advantages of excellent endurance, fast speed, low power consumption, compatibility with Complimentary Metal-Oxide-Semiconductor (CMOS) technology and back-end of line (BEOL) compatibility including down scalability **[1, 2]**. In MIM structure, the resistive switching (RS) behavior results from the periodic change in resistance between high resistance state (HRS) and low resistance state (LRS) on applying a voltage sequence across metal electrodes.

RS behavior has been reported in numerous materials including solid electrolytes, perovskites, metal nitrides and carbon-iron composite **[3-5]**. Recently, nitride thin films such as AlN, NiN and Si_3N_4 have been strong candidates for resistive switching application, having emphasized on their low voltage/current operation including full compatibility with CMOS technology **[6-7]**. Nitride thin films bestow additional properties such as high hardness, excellent thermal conductance and high dielectric constant as compared to other conventional material **[8]**. Among many nitrides, AlN possesses wide band gap (6.2 eV), very high thermal conductivity (180 $Wm^{-1}K^{-1}$), good electrical insulating properties ($\rho=10^9$ - 10^{11} Ω-m) and high dielectric constant (12.4), could result in excellent switching performance of AlN thin film. In general, AlN thin films can be deposited by various deposition techniques such as atomic layer deposition, cathodic arc evaporation and magnetron sputtering. Due to having precise thickness control, lower deposition temperature and large area uniformity, the magnetron sputtering have been established as a remarkable deposition technique for thin film fabrication. The sputtering technique provides good step coverage, hence the interfaces of the layers in MIM structure are of good quality. Therefore, the study of AlN thin film fabricated using sputtering technique would be of great interest for ReRAM application **[6]**.

In this work, we report the reproducible bipolar RS behavior of sputtered deposited AlN thin film sandwiched between Cu & Pt electrodes and discussed the possible physical mechanism of the observed bipolar RS behavior. The high HRS/LRS ratio, endurance and retention are also investigated in order to propose AlN thin film for reliable non-volatile ReRAM application.

3.1.2 Experimental details

In this study, the AlN thin film was deposited on Pt/Ti/SiO_2/Si substrate using DC reactive magnetron sputtering (Excel Instruments, India) at the temperature of 400 ºC. At lower temperature, the film was found to be amorphous while higher temperature results as polycrystalline AlN thin film. For electrical measurement, the Cu top electrodes (TE) with diameter of 300 µm were also deposited by sputtering at room temperature with a shadow mask. Prior to deposition, the sputtering chamber was evacuated using a turbo molecular pump attached with a rotary pump to achieve a high vacuum of the order of 10^{-7} Torr. This order of high vacuum inside the sputtering chamber assured the thin film growth with minimum contamination. For the deposition of AlN thin film and Cu TE, 99.99 % pure Al and Cu targets were sputtered in (Ar+N_2) and Ar atmosphere respectively at the deposition pressure of 5 m Torr. The gas ratio (Ar:N_2) during AlN thin film deposition was kept 1:1. Here, nitrogen gas flow plays a crucial role during AlN thin film deposition. It was found that the crystallinity and orientation of the film are strongly depend upon nitrogen flow amount. The target power was set to 80 Watt for both AlN thin film and Cu TE deposition.

The orientation and crystallinity of the sputtered AlN thin film were studied using X-ray diffractometer (XRD) (Bruker AXS, D8 advanced model) with CuK_α (1.54 Å) radiation in θ-2θ range. Thickness of AlN film was measured using field emission scanning electron microscopy (FE-SEM) FEI Quanta 200F and it found to be ~70 nm. The RS behaviour of Cu/AlN/Pt structure was examined by performing a direct current-voltage (I-V) measurement in a double sweep using Keithley 4200 semiconductor characterization system (SCS).

3.1.3 Results and discussion

Fig. 3.1 shows the XRD pattern, that exhibits the presence of a dominant wurtzite c-axis (002) reflection along with (101) and (102) of AlN. Additional XRD peak is related to Pt with (111) orientation. The insets **(I)** and **(II)** of **Fig. 3.1** show the schematic for electrical measurement and cross sectional FE-SEM image of the AlN/Pt/Ti/SiO_2/Si, respectively. Inset **(II)** of **Fig. 3.1** indicates that the upper most layer (AlN) is dense, uniform and having a good

quality interface along with columnar structure. Cheng et al. recommended that columnar structure with grain boundaries are favourable to develop a conducting path which is essential for RS behaviour **[9]**.

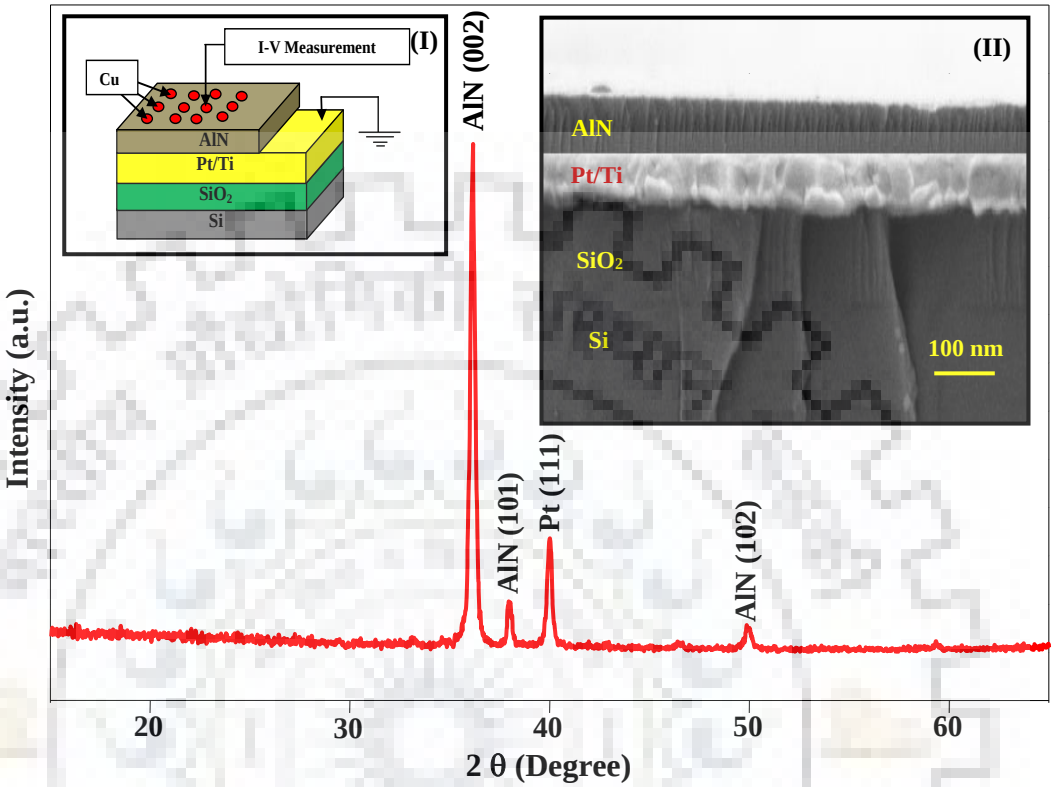

Figure 3.1. X-ray diffraction pattern of AlN film. The insets (I) and (II) show the schematic and cross section of the Cu/AlN/Pt structure.

In order to investigate the RS properties in Cu/AlN/Pt structure, a current-voltage (I-V) measurement was performed. The Cu/AlN/Pt cell exhibits excellent bipolar RS behaviour according to 0 V→ + 4 V→ 0 V→ - 4 V→ 0 V DC sweeping sequence. A typical switching cycle is also indicated by arrows in **Fig. 3.2**. For the I-V characteristics, the voltage is applied to the Cu TE while Pt bottom electrode (BE) was connected to ground. Before applying the positive voltage, the fresh Cu/AlN/Pt cell was found in OFF state or high resistance state (HRS). As a positive voltage **(Step A)** was applied to the Cu TE, the Cu/AlN/Pt memory cell shows a linear increase in current on log-linear scale. At + 5.8 V (forming voltage), an electroforming process takes place, as a result the current is abruptly increased and the memory cell switches from HRS to LRS as depicted in the inset of **Fig. 3.2**. Subsequent to electroforming process, due to formation of conducting paths the observed SET voltage V_{SET} is found to be + 2.4 V **(Step B)**. At + 2.4 V, the memory cell switches to LRS from HRS. A compliance current (I_c) of 10 mA was fixed to prevent the device from breakdown during SET

process while no I_c was given for RESET process. Higher than 10 mA I_c causes significant leakage current and the memory cell may alters to LRS permanently. As the negative voltage sweep (0V→ - 4 V) applied to memory cell, a gradual decrease in the current was observed at -1.7 V (RESET voltage V_{RESET}). It implies that the memory cell switches back to HRS (OFF state) from LRS (ON state) at -1.7 V.

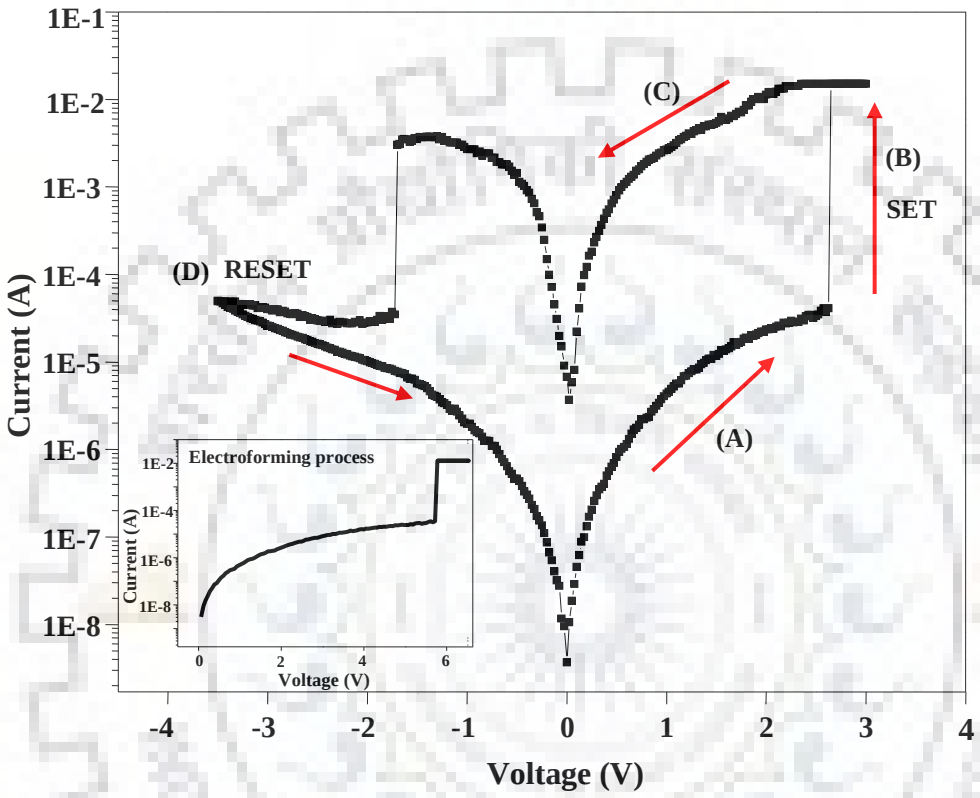

Figure 3.2. Bipolar current-voltage curves of Cu/AlN/Pt memory cell on semi log scale and the inset shows irreversible forming process.

To explore the conduction and bipolar resistive switching mechanism in Cu/AlN/Pt memory cell, we re-plot the I-V curve in double logarithm scale. **Fig. 3.3 (a)** and **(b)** show, the logarithmic plot and linear fitting, for both HRS and LRS in positive voltage region respectively. The log (I) - log (V) plot for HRS exhibits considerable deviation from linearity (non ohmic) at high voltage region ($V < V_{SET}$), while it is ohmic at low voltage ($V << V_{SET}$). On the basis of the slope, charge transport behaviour in HRS can be divided into four parts as shown in **Fig. 3.3 (a)**, first ohmic region ($I \propto V$) in low voltage regime (~ 0.15) with slope 0.99, which follows the equation: $J= qn_0\mu V/L$, where q is charge and n_0 is the density of free electron which are thermally generated. In the middle of HRS curve, in high voltage regime (0.15 - 0.78) the measured slope is 1.92 ($I \propto V^2$), this current transport mechanism is governed according to Mott-Gurney law ($J = 9/8\varepsilon\mu V^2/L^3$ where ε is the permittivity of free space).

Subsequent to this, the current is steeply increased with the voltage ($I \propto V^3$) in voltage regime (0.78 - 1.9) with the slope 3.4. After the steeply increased current region, the conduction transport mechanism again follows the Mott-Gurney law ($I \propto V^2$) in the voltage regime (1.9 - 2.6).

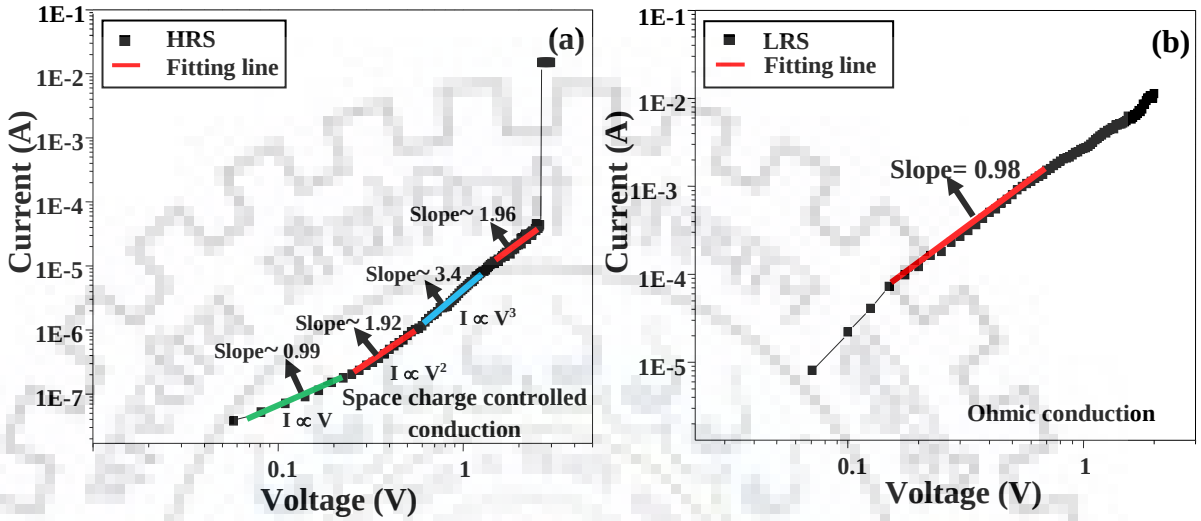

Figure 3.3 (a)-(b) The I-V curves on double logarithmic scale and the fitting corresponding slopes for HRS and LRS respectively.

This pattern of current conduction can be elucidating by classical space charge limited conduction (SCLC) which also covers above mentioned four current conduction regions **[6, 10]**. Apart from the SCLC, the conduction mechanism in HRS can also be illustrated by a weak filamentary model which possess two main regions. In first region, the weak filamentary channels ($I_{filament}$) and in second region the current in bulk (I_i) are responsible for current conduction. $I_{filament}$ dominates only when the measurement is carried out at temperature below 250 K while our measurement was performed at room temperature. Thus the current is flowing by only I_i, hence SCLC governs the current conduction in HRS. **Fig. 3.3 (b)** shows the slope of log(I) - log(V) curve for LRS is 0.98 which is near to 1 i.e. ($I \propto V$). This ($I \propto V$) dependency indicates that the current conduction mechanism in LRS is dominated by Ohmic law.

The relation between compliance current I_c and maximum current in RESET process (I_{RESET}) of SET-RESET cycle for 5 iteration in Cu/AlN/Pt memory cell are plotted in **Fig. 3.4**. From the data given in **Fig. 3.4**, it can be seen that I_{RESET} increases as I_c increases i.e. I_{RESET} is proportional to I_c.

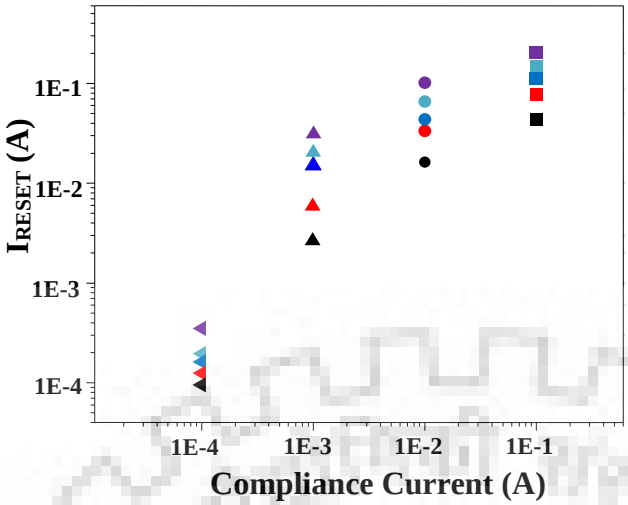

Figure 3.4 I_{RESET} as a function of compliance current I_c for 5 SET-RESET test cycle of Cu/AlN/Pt memory cell.

Therefore, the I_{RESET} can restrict for a desired magnitude by varying the I_c and it is promising to lower down the power consumption by just lowering the I_c. Optimization of I_c is frequently used to improve the endurance and depress the power consumption, which is necessary for better performance in future advances.

To examine the mechanisms of the RS behaviour, a localized conductive filamentary (CFs) model has been widely accepted. As the positive voltage is applied on Cu TE which is an electrochemical active metal, oxidation in Cu take place and as a result Cu ions are generated. These Cu ions approaches towards Pt BE via grain boundary or crystal defects presented in AlN thin film. The oxidation event can be depicted by chemical reaction as written below,

$$Cu \longleftrightarrow Cu^{n+} + ne^{-} \ (n = 1, 2).$$

As the sufficient Cu ions reach at Pt BE and here Cu ions become Cu atoms which form a filament type conducting path that interconnects the TE and BE as shown in **Fig. 3.5**. Therefore, the memory cell changes its resistance state from HRS to LRS **[11]**. However, as the voltage polarity on Cu TE reverses, an electrochemical dissolution near the Cu filament occurs. Thus, the conducting filament is ruptured from its weakest part and the memory cell switches back to HRS. It was noticed that a high voltage needed for a fresh Cu/AlN/Pt device due to defect free AlN layer. After completing electroforming and RESET process, many ruptured Cu filaments are presented in the AlN film. Therefore, most of the time SET voltage found lower then forming voltage which is also shown in the inset of **Fig. 3.2.**

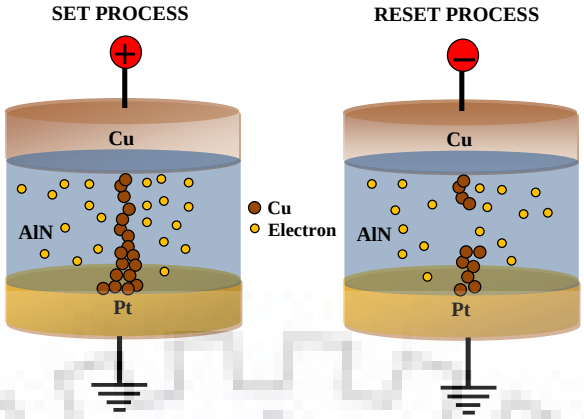

Figure 3.5. Schematic diagram for switching mechanism of Cu/AlN/Pt memory cell. The SET process indicates the formation of Cu conductive filament whereas the RESET process indicates the rapture of conductive filament.

Initially the conducting filament is small but it becomes larger with increasing current and I_c. **Fig. 3.4** also shows that the I_{RESET} follow I_c, thus the larger conducting filament favours to the large I_{RESET} which rupture the filament. Apart from formation of conductive metallic filament, the electron migration in nitride related vacancies in AlN layer may also responsible for resistive switching behaviour **[12]**.

To examine the reliability of Cu/AlN/Pt structure for resistive memory application, the endurance and retention properties are further investigated using a + 4V, 100 ns pulse for SET condition (LRS) and - 4V, 100 ns pulse for the RESET condition (HRS) at 85 ℃. The LRS and HRS states were measured at read voltage of 0.1 V repetitively as shown in **Fig. 3.6 (a)** and **(b)**.

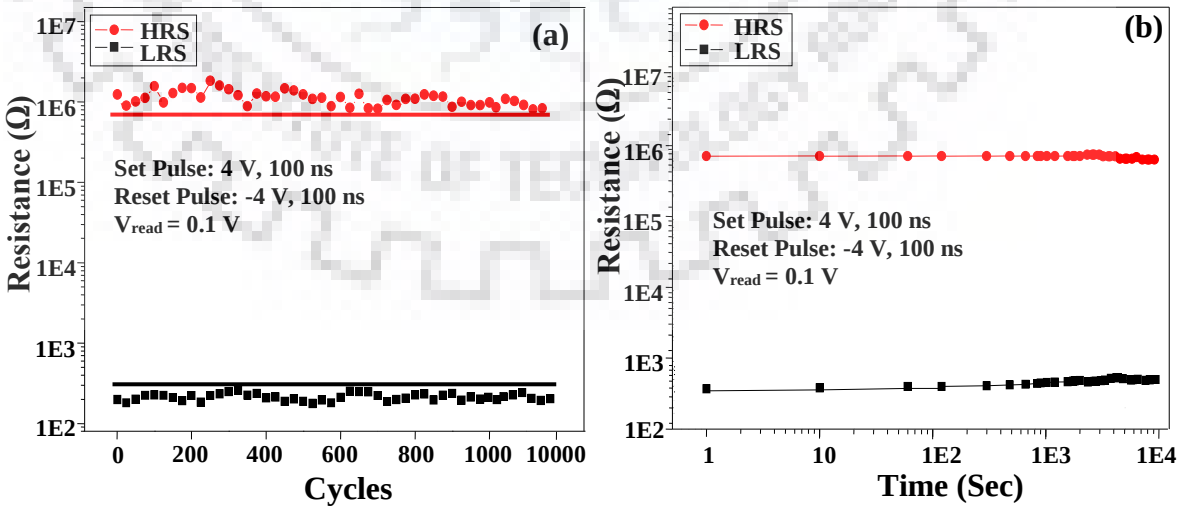

Figure 3.6. The SET process indicates the formation of Cu conductive filament whereas the RESET process indicates the rapture of conductive filament. **(b)** and **(c)** Endurance performance and retention of the Cu/AlN/Pt memory cell respectively.

The resistance in HRS and LRS in Cu/AlN/Pt configuration exhibits little bit degradation after 10000 cycles, it indicates that memory window stable upto 10^4 cycles as shown in **Fig. 3.6 (a)**. This stability strongly suggest that the resistive switching in our Cu/AlN/Pt configuration is reliable, reproducible and no need of additional electrical power to sustain the resistance in a determined state. The resistance ratio between HRS and LRS was found close to 10^4. From the retention property which is plotted in **Fig. 3.6 (b)**, it was observed that there is no significant deviation in resistances for 10^4 s of experiment. Thus, it is recommended that the data stored in Cu/AlN/Pt memory cell saved extended to 10^4 s.

3.1.4 Conclusions

In summary, the sputtered AlN thin film was used to construct Cu/AlN/Pt memory cells to study the bipolar resistive switching properties. Formation/disruption of conducting filament is confirmed as the main cause for exhibiting the resistive switching properties. Trap controlled space charged limited current (SCLC) and ohmic behaviour are dominated conduction mechanisms at HRS and LRS respectively. The resistance ratio of HRS/LRS (~ 10^4), excellent write/erase endurance (10^4) and non-volatile long retention (10^4 s) are also measured. This study proposed that the Cu/AlN/Pt configuration could be a considerable candidate for next generation non-volatile ReRAM application.

3.2 Effect of top electrode material on resistive switching properties of WN based thin films for non-volatile memory application

3.2.1 Introduction

In recent time, the conventional Si charge storage based semiconductor memory device technology needed to be shrunk down to accomplish huge data storage for reliable performance **[13-15]**. This requirement is facing many obstacles due to the physical and technical restriction during fabrication of memory devices. Currently, bipolar resistive switching (BRS) behaviour in Metal-Insulator-Metal (MIM) structure attracts a great deal of attention to serve as a next generation non-volatile Resistive Random Access Memory (ReRAM) **[1, 16-17]**. The resistance states in insulating layer of MIM structure are achieved due to the formation/disruption of conducting filament and/or ion migration on application of a voltage between both top and bottom metal electrodes **[18-20]**. The MIM structure based ReRAMs possesses the advantage of high speed performance, low power consumption, easier scaling down and full complimentary metal-oxide-semiconductor (CMOS) compatibility **[1, 21-22]**. These ReRAMs can be divided into two groups i.e. cation based (metal cation) and anion based (oxygen or nitrogen anions) **[16]**. Cation based ReRAMs usually consist of an electrochemically active top electrode (such as Cu, Ag, etc.) **[23, 24]**, while the bottom electrode is made of electrochemically inert metal (e.g. Pt, Au etc.) **[25, 26]**. The selection of both top and bottom electrode material also plays a significant role on resistive switching performance due to their chemical reactivity and work function **[27-29]**. Excluded to the binary (two levels) resistance switching, the multilevel resistive switching could provide improved data storage density and low cost per bit, hence effective memory circuits can be obtained by adjusting the creation and annihilation of conductive filaments **[3-4]**.

There are several thin films of perovskites, solid electrolytes, binary transition metal oxides and ferromagnetic materials in which resistive switching (RS) behaviour has been reported **[26-27]**. However, large RESET current, slow RESET time and enormous variation in resistance between different states are still challenges for the researchers **[12]**. Recently, thin films of aluminium nitride (AlN), nickel nitride (NiN), silicon nitride (Si_3N_4) and tungsten nitride (WN) material are greatly used as active switching layer due to possessing a wide spectrum of advantages such as fast speed, long retention, low voltage operation, high hardness and excellent thermal conductance **[10, 30-31]**.

In order to improve the complementary-metal-oxide-semiconductor (CMOS) compatible integration under backend-of-line (BEOL) process, transition metal nitrides such as TiN, WN and TaN, have been investigated as resistive switching layer and electrode materials **[32-34]**. WN has attracted a great interest as it reflects excellent characteristics like good chemical inertness, high thermal stability and superior diffusion barrier properties along with high CMOS BEOL compatibility **[35-37]**. To date, the related studies on resistive switching of WN thin film are very rare **[31]**. Here we fabricate TE (Ti, Al and Cu)/WN/Pt structure and proposed a more convenient and strong way to improve the resistive switching performance of WN thin film by electrode engineering.

3.2.2 Experimental details

The tungsten nitride (WN) thin films were fabricated on Pt/Ti/SiO_2/Si substrate using DC reactive magnetron sputtering at 200 ºC. For WN thin film deposition, argon (Ar) and nitrogen (N_2) gases were used as sputtering gas and reactive gas respectively with 1:1 ratio. Prior to sputtered deposition, the Pt/Ti/SiO_2/Si substrates were thoroughly cleaned using boiled acetone. To attain the essential MIM structure for electrical measurement, top electrodes (TE) of (Ti, Al and Cu) with a diameter of 100 µm were deposited on WN thin film by shadow mask sputtering of respective targets at room temperature. The DC sputtering power for deposition of the WN thin film was set to 60 watt, while 40 watt power was kept for deposition of all three TE. The sputtering chamber was evacuated to 2×10^{-6} Torr base pressure and the deposition pressure was maintained to 10 m Torr for all sputtering depositions.

The crystallographic orientation and phase formation of the WN thin films were inspected using Bruker advanced diffractometer (D8) CuK_α (1.54 Å) with θ-2θ geometry. Cross sectional FE-SEM (FEI Quanta 200F) was used to measure the thickness of WN thin film and to ensure about the interfaces of MIM structure. To investigate the resistive switching properties, the electrical characterizations of (Ti, Al and Cu)/WN/Pt memory cells were carried out using the Keithley 4200 SCS (semiconductor characterization system). During the measurements in voltage sweeping and pulse programming/erasing modes, the DC voltage polarity was set to positive for TE and the bottom electrode (BE) was connected to ground. In order to protect the structure from permanent breakdown, a compliance current of 10 mA was also applied during the I-V measurements.

3.2.3 Results and discussion

The XRD pattern of deposited WN thin film on Pt/Ti/SiO_2/Si substrate is depicted in **Fig. 3.7**. The single (111) orientation of W_2N phase is observed, which is closed packed face centred cubic (FCC) with the minimum surface energy [32].

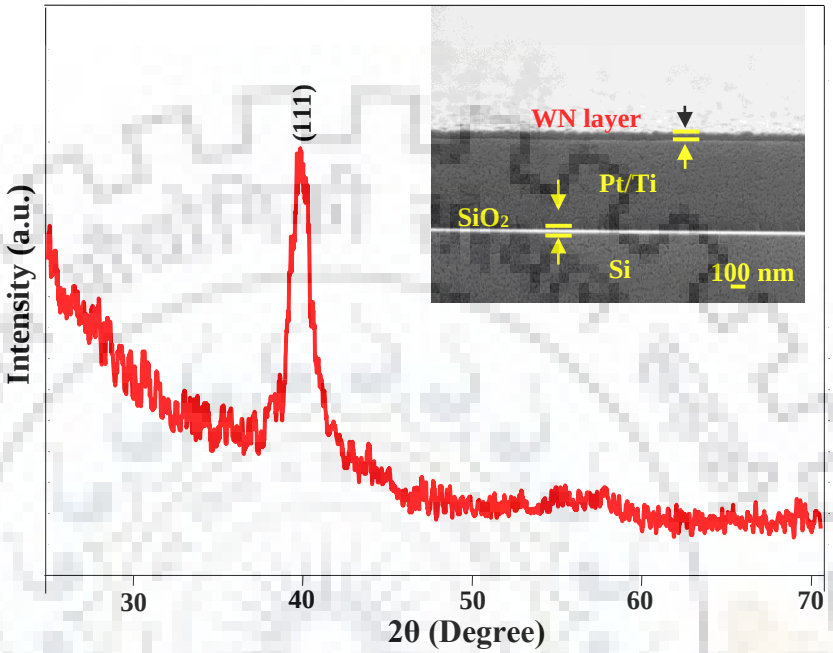

Figure 3.7. XRD pattern of WN thin film on Pt coated Si substrate. The inset shows the cross-sectional FE-SEM image of WN/Pt/Ti/SiO_2/Si stack configuration.

Inset of **Fig. 3.7** displays the cross sectional FE-SEM image of typical WN/Pt/Ti/SiO_2/Si stack configuration, which reveals that the thickness of WN thin film is approximately 65 nm.

Initially, the nature of all three pristine (Ti, Al and Cu)/WN/Pt memory cells was found insulating. To switch the memory cell into low resistance states (LRS) from high resistance state (HRS) an electroforming process is mostly required. This forming process was carried out by applying a positive voltage on the top electrode of memory cells and it was found to be almost similar for all TE (Ti, Al and Cu)/WN/Pt memory cells. **Fig. 3.8** shows the characteristic reproducible current-voltage (I-V) curves in a semi-log scale for all the three (Ti, Al and Cu)/WN/Pt configurations. A DC voltage sequence 0 V → + 2.5 V → 0 V → - 2.5 V → 0 V was swept on the TE with 10 mA compliance current while the BE was always connected to ground for all memory cells.

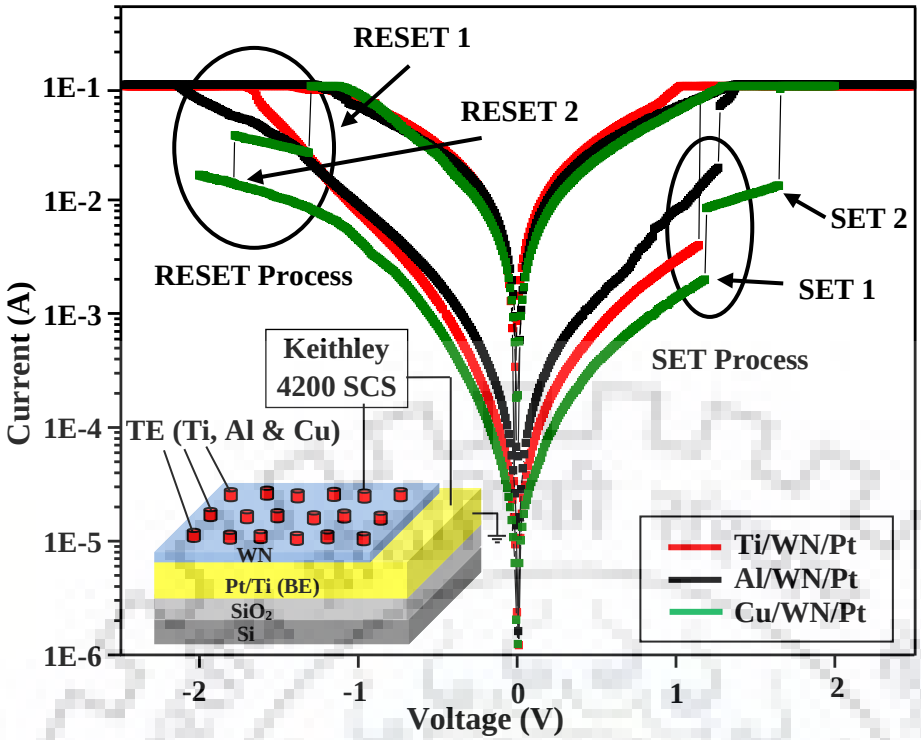

Figure 3.8. Typical I-V characteristics of (Ti, Al and Cu)/WN/Pt/Ti/SiO_2/Si memory cells in a semi-log scale. The inset shows the schematics diagram of (Ti, Al and Cu)/WN/Pt/Ti/SiO_2/Si memory cells.

As the positive bias swept from 0 to a critical value of about 1.1 V (the circle marked in **Fig. 3.8**), the current is abruptly increased and as a result the memory cells were switched to LRS from HRS. The transition of memory cell from HRS to LRS is called "SET" process. The LRS was continued in applied voltage regime from + 2.5 V to 0 V. When the voltage was sweeping from 0 V to - 2.5 V, a "RESET" process takes place and the current was dramatically decreased as indicated in circle. Then, the HRS was maintained for voltage sweep from -2.5 V to 0 V. These results confirm the presence of bipolar resistive switching.

(Ti and Al)/WN/Pt memory cells show more or less similar resistive switching behaviour. The SET voltages (V_{SET}) for Ti and Al TE were observed at 1.14 V and 1.28 V, respectively. RESET voltages (V_{RESET}) were observed at - 1.6 V and - 2.1 V. The current levels of LRS and HRS were 10^{-2} and 10^{-4} A respectively for both Ti and Al TE, thus the resistance ratio between HRS and LRS is found to be 10^{-2}. Moreover, despite of two resistance states for Ti and Al TE, three distinguishable resistance states are achieved with the Cu TE, as depicted in **Fig. 3.8**. These three (multilevel) resistance states are noted as low resistive state (LRS), middle resistive state (MRS) and high resistive state (HRS) with current levels of approximately 10^{-2}, 10^{-3} and 10^{-4} A, respectively. The resistance ratio value between MRS:

LRS and HRS: MRS is measured to be 10, therefore the resistance levels can be identified individually.

In order to examine the reliability of the WN thin films with different TE for resistive switching memory application, the endurance and retention properties were investigated at 85˚ C. A + 2.5 V 100 ns pulse and - 2.5 V 100 ns pulse with a read voltage of 0.1 V were used for SET condition (LRS) and RESET condition (HRS) respectively for Ti and Al TE as shown in **Fig. 3.9 (a)**. Further, the additional pulses of +1.3 V 100 ns and -1.3 V 100 ns were given to read the MRS of the memory cell with Cu TE as shown in **Fig. 3.9 (b)**. The resistance in HRS, MRS and LRS little bit degrade after 10^5 cycles, which implies that the memory window is stable up to 10^5 cycles as shown in **Fig. 3.9 (a)-(b)**.

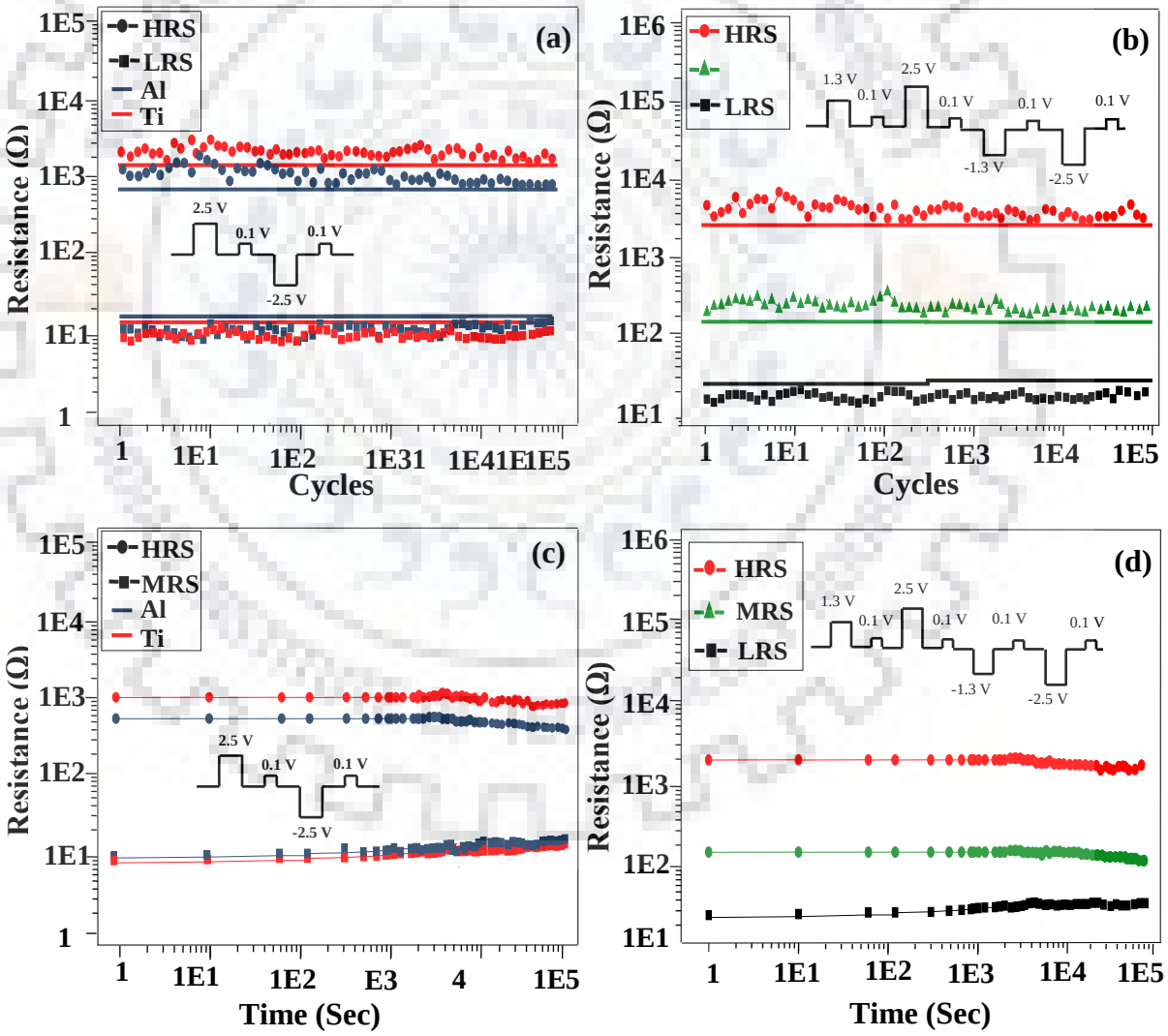

Figure 3.9 (a)-(b) Endurance characteristics of (Ti and Al)/WN/Pt and Cu/WN/Pt memory cells respectively at read voltage of 0.1 V. **(c)-(d)** Retention characteristics of (Ti and Al)/WN/Pt and Cu/WN/Pt memory cells respectively at read voltage of 0.1 V.

In addition, **Fig. 3.9 (c)-(d)** show the retention characteristic for each resistive level for Ti, Al, and Cu TE respectively. From the measured data of **Fig. 3.9 (c)-(d)**, it is clear that non-volatile retention is maintained up to 10^5 sec for LRS and HRS with Ti and Al TE and LRS, MRS and HRS for the Cu/WN/Pt memory cell, with some small degradation in the end. Thus, it demonstrates the potential of Cu/WN/Pt configuration for multilevel non-volatile ReRAM application.

In order to explore the switching and conduction mechanism in (Ti, Al and Cu)/WN/Pt memory cells, the I-V curves have been re-plotted on double-logarithmic scale and reveal the analogy with power law relation ($I \propto V$). The linear fitting results of the positive voltage region are shown in **Fig. 3.10**.

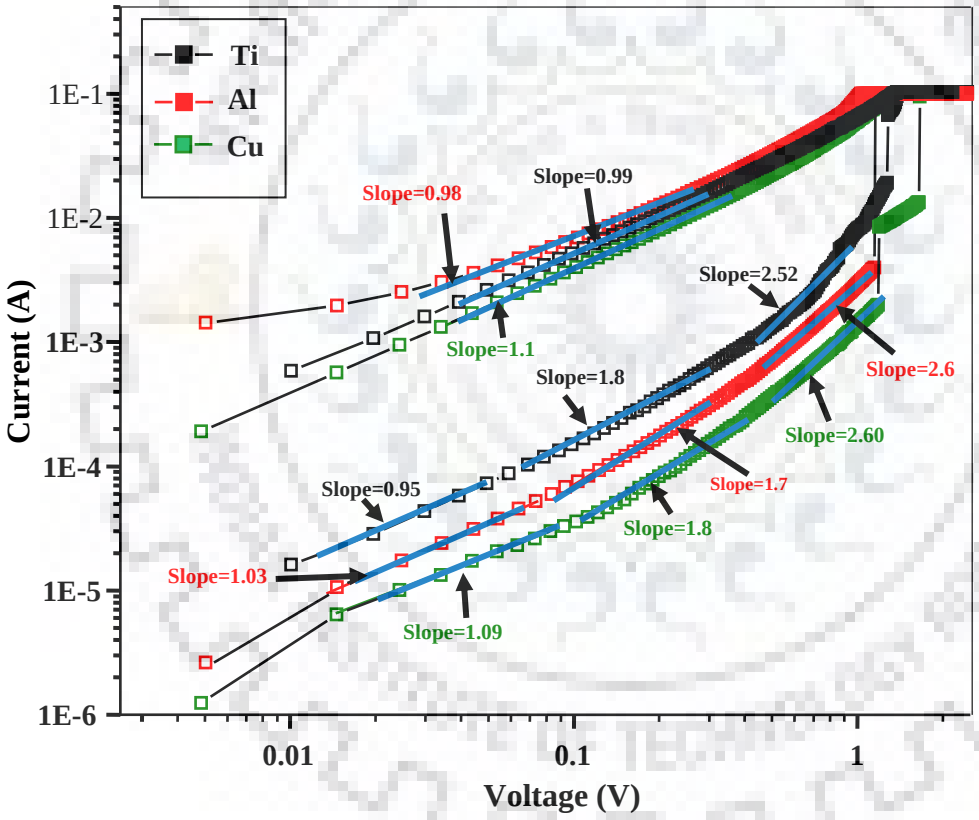

Figure 3.10. The I-V plots and their respective slopes for the LRS, MRS and HRS on double log scale.

In LRS region, the slope for all three (Ti, Al and Cu)/WN/Pt memory cells are measured as 1.09, 0.95 and 0.97 respectively, which are close to 1. Thus, the current conduction mechanism in memory cells during LRS is dominated according to Ohmic law ($I \propto V^1$) by virtue of the formation of conducting filaments. However, the HRS consists of at least three voltage regions, which endorse that the current conduction mechanism is much more

complex in OFF state. First is Ohmic region at low voltage (V= 0 V to 0.1 V), as the measured slops are 1.03, 0.95 and 1.09 for Ti, Al and Cu TE respectively, which are close to 1. Thus, the current conduction at low voltage follows the equation $J=qn_0\mu V/L$, where q is charge and n_0 is the thermally generated free electrons. Thereafter, at voltage regime 0.1 V to 0.6 V, the current follows the square dependence ($I \propto V^2$) with voltage, that corresponds to Mott-Gurney law ($J=9/8\varepsilon\mu V^2/L^3$, where ε is the permittivity of free space). In last, the current in HRS is steeply increase with the voltage for all memory cells at higher voltage range (0.6 V to V_{SET}). This kind of charge transport behaviour is accompanied with the trap-controlled space charge limited conduction (SCLC) mechanism in which the current conduction also follows Ohm law ($I \propto V^1$), Mott-Gurney law and steep increase region **[38]**.

The RS behaviour can be elucidated by a conductive filamentary model. In accordance with most of the previous reports, the conduction filament in nitride based thin films is formed by means of electron hopping process in nitride-related electron traps (vacancies) **[12, 30]**. Thus, the generation and recombination of nitrogen vacancies are accountable for the formation/disruption of the conductive filament (ionic filament). As the positive voltage is applied on TE, the nitrogen vacancies are created in active switching layer due to the removal of nitrogen from lattice, which can be write with the following relation,

$$WN \longleftrightarrow W^{n+} + N^{n-} \qquad (n = 1, 2).$$

Subsequently, as spacious positive voltage was employed on TE, the negatively charged N^{n-} ions drifted towards TE, since W^{n+} ions moves towards BE. These drifted N^{n-} ions leave behind nitride-related traps in the active switching layer and get accumulate near the TE interface. As most of these traps are filled inwardly due to electron trapping which is also known as trap-to-trap hopping phenomena, a conduction path is fomed and SET condition occurs. For RESET condition, as negative voltage was applied onto TE, nitrogen ions wander back to the switching layer and recombine with their nitride related traps which disrupt the conducting filament. Therefore, the switching mechanism in binary states for Al and Ti top electrodes can be explained due to formation and disruption of ionic filaments as shown in **Fig. 3.11 (a)-(b)**.

Apart from this, some reports aslo recommonded that if the TE material is an electrochemically active material such as Cu and Ag then, on applying a positive voltage, a redox reaction takes palce and the metal ions are generated like following equation,

$$M \longleftrightarrow M^{n+} + ne^{-} \ (M = Cu \text{ or } Ag).$$

Thereafter, these M^{n+} metal ions migrate towards BE via grain boundries or crystal defects which always present in crystal lattice of thin film and turns into metal atoms by accepting electron at BE surface. As adequate metal atoms are accumulated over the BE surface, they form a metallic filament which interconnects the TE and BE, thus the memory cell switches to LRS from HRS. As the voltage polarity reverses, the metal filament disrupt from its weakest part due to elecrochemical dissolution and the memory cell comes back into HRS from the LRS **[6]**.

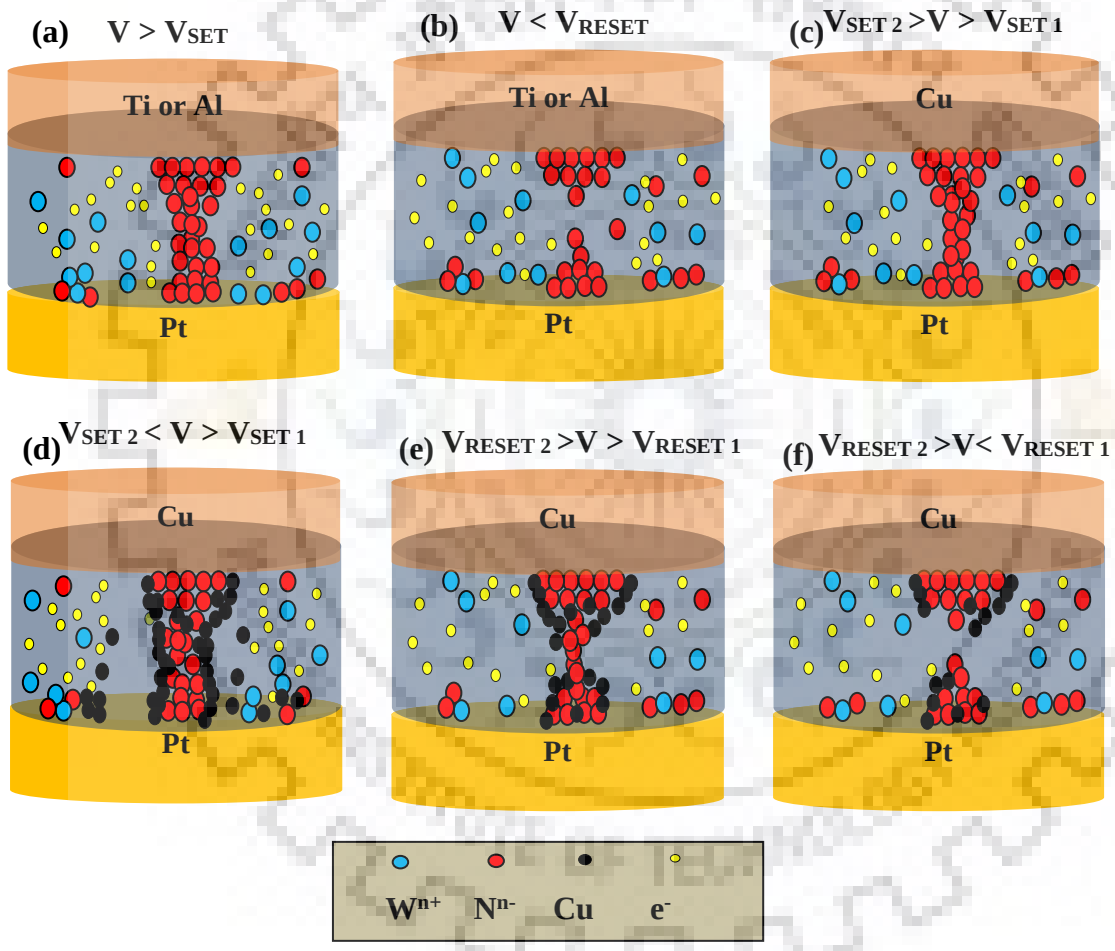

Figure 3.11. (a)-(b) Schematic of both the formation and the rupture process of ionic conducting filament within (Ti and Al)/WN/Pt memory cells. **(c)-(f)** formation and the rupture process of ionic and metallic conducting filament in Cu/WN/Pt memory cells.

In multilevel (three levels) resistive switching with Cu TE, two SET processes (MRS and LRS) appears, as can be seen in **Fig. 3.8**. The resitance of these three levels correspond to HRS, MRS and LRS were measured at 0.1 V read voltage and considered as R_{HRS} (2.85 KΩ), $R_{SET\ 1}$ (138 Ω) and $R_{SET\ 2}$ (25 Ω).

In order to understand this multilevel switching mechanism in memory cells with Cu TE, temperature vs resistance experiments were performed after the SET 1 ($V_{SET\ 1}$ = 1.1 V) and SET 2 ($V_{SET\ 2}$ = 1.4 V), as shown in **Fig. 3.12.**

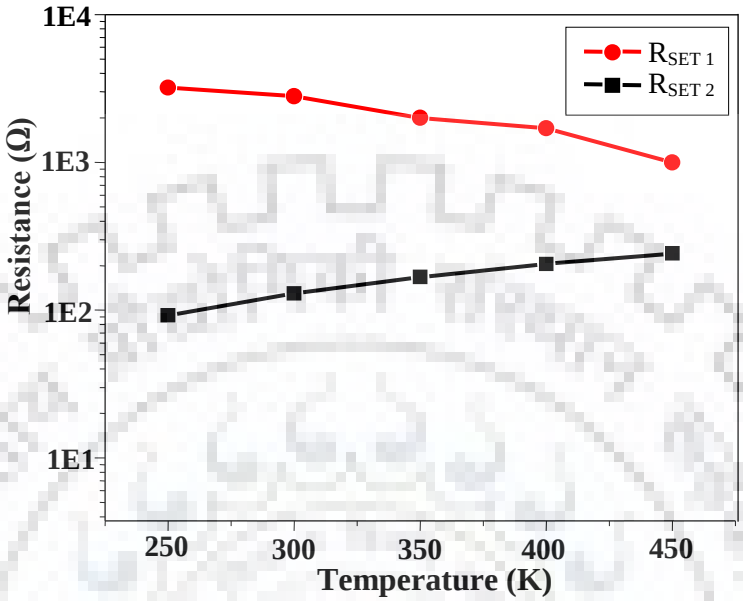

Figure 3.12. $R_{SET\ 1}$ and $R_{SET\ 2}$ as a function of temperature.

The curves of resistance as a function of the temperateure in 250 K - 450 K range, demonstrating that $R_{SET\ 1}$ is decreasing and $R_{SET\ 2}$ is increasing with the incresing tempreture. The decrease in $R_{SET\ 1}$ implies the formation of ionic filament after SET 1 process. The linear dependency of $R_{SET\ 2}$ on increasing tempreture is due to the formation of Cu metallic filament after the SET 2 process **[23]**. On comparison with ionic filament switching, the SET/RESET voltage for metellic filament are found to be at higher voltage due to the fact that the oxidation of Cu starts at higher voltage compared to the start of electron hopping process in nitride-related traps. In RESET process, the local joule heating disrupts this metallic filament from its weakest part, which has non polar nature. The mechenism process related to multilevel switching behavior in Cu/WN/Pt memory cell is depicted in **Fig. 3.11 (c), (d), (e)** and **(f)**.

3.2.4 Conclusions

In summary, we have fabricated TE (Ti, Al and Cu)/WN/Pt stack configurations using sputtering technique for non-volatile resistive random access memory (ReRAM) application. The binary resistance state switching is achieved with Ti and Al TE as a result of formation/disruption of the ionic filament. Apart from the ionic filament, the introduction of additional metallic filament with Cu TE is confirmed as the main cause of multiresistance states in Cu/WN/Pt structure. The dominant conduction mechanism for all the memory cell is SCLC

for HRS and MRS, while ohmic conduction governs the LRS. All three memory sturctures exhibit low operation voltage, good write/erase endurance and long non-volatile retention properties. It is recommonded that the electode engineering is a good approach to construct multilevel resistive random access memory devices for future memory application.

3.3 Reference

[1] Waser R., Aono M., "Nanoionics-based resistive switching memories", *Nat. Mater.*, **6,** 833 (2007).

[2] Linn E., Rosezin R., Kügeler C., Waser R., "Complementary resistive switches for passive nanocrossbar memories", *Nat. Mater.*, **9**, 403 (2010).

[3] Yan X. B., Yin J., Guo H. X., Su Y., Xu B., Li H. T., Yan D. W., Xia Y. D., Liu Z. G., "Bipolar resistive switching performance of the nonvolatile memory cells based on $(AgI)_{0.2}(Ag_2MoO_4)_{0.8}$ solid electrolyte films", *J. Appl. Phys.*, **106**, 054501 (2009).

[4] Chang W. Y., Liao J. H., Lo Y. S., Wu T. B., "Resistive switching characteristics in $Pr_{0.7}Ca_{0.3}MnO_3$ thin films on $LaNiO_3$-electrodized Si substrate", *Appl. Phys. Lett.*, **94**, 172107 (2009).

[5] Zhou J. W., Li T. R., Zhang D., Ren B., Zhang S. W., Huang J., Zhang J. M., Wang L., Jiang Y. C., Gao J., Wang L. J., "Abnormal bipolar resistive switching behavior in carbon-iron composite films with different thicknesses", *Vacuum*, **135**, 115-120 (2017).

[6] Chen C., Yang Y. C., Zeng F., Pan F., "Bipolar resistive switching in Cu/AlN/Pt nonvolatile memory device", *Appl. Phys. Lett.*, **97**, 083502 (2010).

[7] Kim H. D., An H. M., Kim T. G., "Resistive-switching behaviour in Ti/Si_3N_4/Ti memory structures for ReRAM applications", *Microelectron. Eng.*, **98**, 351–354 (2012).

[8] Choi D., Kumta P. N., "Chemically synthesized nanostructured VN for pseudocapacitor application", *Electrochem. Solid. St.*, **8(8)**, A 418-A 422 (2005).

[9] Chang W. Y., Lai Y. C., Wu T. B., Wang S. F., Chen F., Tsai M. J., "Unipolar resistive switching characteristics of ZnO thin films for nonvolatile memory applications", *Appl. Phys. Lett*. **92**, 022110 (2008).

[10] Kim S., Kim H., Jung S., Kim M. H., Lee S. H., Cho S., Park B. G., "Tuning resistive switching parameters in Si_3N_4-based RRAM for three-dimensional vertical resistive memory applications", *J. Alloys Compd*., **663**, 419-423 (2016).

[11] Zhang J., Zhang Q., Yang H., Wu H., Zhou J., Hu L., "Bipolar resistive switching properties of AlN films deposited by plasma-enhanced atomic layer deposition", *Appl. Surf. Sci*., **315**, 110–115 (2014).

[12] Kim H. D., An H. M., Lee E. B., Kim T. G., "Stable bipolar resistive switching characteristics and resistive switching mechanisms observed in aluminium nitride-based ReRAM devices", *IEEE T. Electron. Dev*., **58**, 10 (2011).

[13] Zheng Y., Cheng Y., Zhu M., Ji X., Wang Q., Song S., Song Z., Liu W., Feng S., "A candidate Zr-doped Sb_2Te alloy for phase change memory application", *Appl. Phys. Lett*., **108**, 052107 (2016).

[14] Gottwald M., Kan J. J., Lee K., Zhu X., Park C., Kang S. H., "Scalable and thermally robust perpendicular magnetic tunnel junctions for STT-MRAM", *Appl. Phys. Lett*., **106**, 032413 (2015).

[15] Kim Y., Seo J. Y., Lee S. H., Park B. G., "A new programming method to alleviate the program speed variation in three-dimensional stacked array NAND flash memory", *J. Semicond. Technol. Sci*., **14**, 566 (2014).

[16] Yang J. J., Pickett M. D., Li X. M., Ohlberg D., Stewart D. R., Williams R. S., "Memristive switching mechanism for metal/oxide/metal nanodevices", *Nat. Nanotechnol*., **3**, 429 (2008).

[17] Kim K. M., Jeong D. S., Hwang C. S., "Nanofilamentary resistive switching in binary oxide system; a review on the present status and outlook", *Nanotechnology*, **22**, 254002 (2011).

[18] Strukov D. B., Snider G. S., Stewart D. R., Williams R. S., "The missing memristor found", *Nature*, **453**, 80 (2008).

[19] Schindler C., Meier M., Waser R., Kozicki M. N., "Resistive switching in Ag-Ge-Se with extremely low write currents", *Proc IEEE Non-Volatile Memory Technol. Symp*. **1**, 82 (2007).

[20] Ke J. J., Liu Z. J., Kang C. F., Lin S. J., He J. H., "Surface effect on resistive switching behaviors of ZnO", *Appl. Phys. Lett*., **99**, 192106 (2011).

[21] Tsunoda K., Fukuzumi Y., Jameson J. R., Wang Z., Griffin P. B., Nishi Y., "Bipolar resistive switching in polycrystalline TiO_2 films", *Appl. Phys. Lett*., **90**, 113501 (2007).

[22] Meijer G. I., "Who wins the nonvolatile memory race?", *Science*, **319**, 1625 (2008).

[23] Yang Y. C., Pan F., Zeng F., "Bipolar resistance switching in high-performance Cu/ZnO: Mn/Pt nonvolatile memories: active region and influence of Joule heating", *New J. Phys*., **12**, 023008 (2010).

[24] Jo S. H., Kim K. H., Lu W., "Programmable resistance switching in nanoscale two-terminal devices", *Nano Lett.*, **9**, 496 (2009).

[25] Zhuge F., Dai W., He C. L., Wang A. Y., Liu Y. W., Li M., Wu Y. H., Cui P., Li R. W., "Nonvolatile resistive switching memory based on amorphous carbon", *Appl. Phys. Lett*., **96**, 163505 (2010).

[26] Bernard Y., Gonon P., Jousseaume V., "Resistance switching of Cu/SiO_2 memory cells studied under voltage and current-driven modes", *Appl. Phys. Lett*., **96**, 193502 (2010).

[27] Lee C. B., Kang B. S., Benayad A., Lee M. J., Ahn S. E., Kim K. H., Stefanovich G., Park Y., Yoo I. K., "Effects of metal electrodes on the resistive memory switching property of NiO thin films", *Appl. Phys. Lett*., **93**, 042115 (2008).

[28] Liao Z. L., Wang Z. Z., Meng Y., Liu Z. Y., Gao P., Gang J. L., Zhao H. W., Liang X. J., Bai X. D., Chen D. M., "Categorization of resistive switching of metal-$Pr_{0.7}Ca_{0.3}MnO_3$-metal devices", *Appl. Phys. Lett*., **94**, 253503 (2009).

[29] Shibuya K., Dittmann R., Mi S., Waser R., "Impact of defect distribution on resistive switching characteristics of Sr_2TiO_4 thin films", *Adv. Mater*., **22,** 411 (2010).

[30] Kim H. D., An H. M., Kim T. G., "Ultrafast resistive-switching phenomena observed in NiN-based ReRAM cells", *IEEE T. Electron. Dev*., **59**, 9 (2012).

[31] Hong S. M., Kim H. D., An H. M., Kim T. G., "Resistive switching phenomena of tungsten nitride thin films with excellent CMOS compatibility", *Mater. Res. Bull*., **48**, 5080 (2013).

[32] Kwak J. S., Do Y. H., Bae Y. C., Im H. S., Yoo J. H., Sung M. G., Hwang Y. T., Hong J. P., "Roles of interfacial TiO_xN_{1-x} layer and TiN electrode on bipolar resistive switching in $TiN/TiO_2/TiN$ frameworks", *Appl. Phys. Lett*., **96**, 223502 (2010).

[33] Zheng Z. W., Cheng C. H., Chou K. I., Liu M., Chin A., "Improved current distribution in resistive memory on flexible substrate using nitrogen-rich TaN electrode", *Appl. Phys. Lett*., **101**, 243507 (2012).

[34] Zhou Q., Zhai J., "The improved resistive switching properties of TaO_x-based RRAM devices by using WN_x as bottom electrode", *Physica B*, **410**, 85 (2013).

[35] Hones P., Martin N., Regula M., Le´vy F., "Structural and mechanical properties of chromium nitride, molybdenum nitride, and tungsten nitride thin films", *J. Phys. D: Appl. Phys*., **36**, 1023 (2003).

[36] Shen Y. G., Mai Y. W., Mckenzie D. R., Zhang Q. C., McFall W. D., "Composition, residual stress, and structural properties of thin tungsten nitride films deposited by reactive magnetron sputtering", *J. Appl. Phys*., **88**, 1380 (2000).

[37] Mohamed S. H., "Thermal stability of tungsten nitride films deposited by reactive magnetron sputtering", *Surf. Coat. Technol*., **202**, 2169 (2008).

[38] Çaldıran Z., Şinoforoğlu M., Metin Ö., Aydoğan Ş., Meral K., "Space charge limited current mechanism (SCLC) in the graphene oxide–Fe_3O_4 nanocomposites/n-Si heterojunctions", *J. Alloys Compd*., **631**, 261 (2015).

[39] Liu M., Abid Z., Wang W., He X. L., Liu Q., Guan W. H., "Multilevel resistive switching with ionic and metallic filaments", *Appl. Phys. Lett*., **94**, 233106 (2009).

Chapter 4

Pd Capped W_2N Nano Porous Thin Films for Remarkable Room Temperature Hydrogen Gas Sensing Performance

CHAPTER 4

Pd CAPPED W_2N NANO POROUS THIN FILMS FOR REMARKABLE ROOM TEMPERATURE HYDROGEN GAS SENSING PERFORMANCE

4.1 Introduction

Nowadays, hydrogen (H_2) gas has become a clean, renewable and potential environmental friendly zero emission carrier that can replace carbon based fossil fuels, which reduces global warming and air pollution **[1**, **2]**. Hydrogen gas has extensive applications in food products, space transportation, fuel cells and industrial chemicals. Moreover, the water (H_2O) is the combustion by-product of the hydrogen and it decomposes again into hydrogen and oxygen. It is well reported that H_2 has very low ignition energy (0.02 mJ) and forms an explosive mixture with air (under ambient condition) when its concentration exceeds beyond 4% by volume **[3]**. It cannot be detected by human senses due to its colorless, tasteless and odorless nature **[4]**. Hence, the monitoring of H_2 leakage is an essential issue in futuristic fuel cells and industries for safety purpose.

The research and development on the hydrogen concentration measurement are going on since early eighties.Over past decades, a large number of materials and structures have been investigated to be employed as hydrogen sensing application. In order to reduce the electric power consumption, the fabrication of highly selective and sensitive hydrogen gas sensor operated at room temperature is today's necessities. Although, many researchers have reported H_2 gas sensors which are able to operate even at room temperature (RT). Among several kinds of gas sensors, chemiresistive gas sensors based on change in electrical resistance of material with exciting diffusion and adsorption of analyte gas molecules on surface of material are in huge demand **[5-7]**. Chemiresistive gas sensors have advantages of low cost, high sensitivity, good selectivity, eco-friendly and long-term operations etc **[8-10]**. From the viewpoint of response time and sensitivity, the porous nanostructures are very promising candidates. Therefore, the special microstructure can provide a large surface-to-volume ratio which can notably make possible diffusion and mass transportation of gas molecules in sensing element **[11-13]**.

In this work, we have deposited the Pd/W_2N nanoballs (NBs) on metal assisted chemical etched porous silicon (PSi) substrate using DC reactive magnetron sputtering method. The PSi substrates basically act as a template to build up numerous nanostructures like nanoballs and nanocauliflowers etc. We have studied the variation in response under different humid ambient for H_2 gas at RT. This study suggests that the porous silicon template paves a new approach to fabricate palladium decorated W_2N NBs structure as a potential candidate for highly sensitive H_2 gas sensing at room RT. The investigations on reproducibility and gas selectivity along with sensing mechanism were also studied in detail.

4.2 Experimental details

4.2.1 Materials and chemicals

The functioning sensing material (W_2N) was extracted from the reactive sputtering (Excel Instruments, India) of tungsten (W) target (99.999 % pure) in Argon (A_2) and Nitrogen (N_2) atmosphere. Further, the palladium (Pd) target (99.999 % pure) was sputtered in only argon ambient. The sputtering targets were purchased from Kurt J. Lesker Company UK. The p-type silicon wafer purchased from Excel instruments, India which was used for making porous silicon substrate. Argon (Ar), nitrogen (N_2) and hydrogen (H_2) gas cylinders were bought from Sigma gases, India.

4.2.2 Sensor fabrication

In order to construct the porous silicon (PSi) substrate, the p-type silicon (100) wafer was cut into pieces of 1×1 cm^2 area using diamond cutter. To remove the grease from the substrates, an ultrasonically cleaning in a mixture of isopropyl alcohol and boiled acetone was done then followed by the washing with de-ionized (DI) water. A piranha solution that consists of H_2O_2 (97 %) and H_2SO_4 (35 %) in 1:3 ratio was prepared to remove the organic stuff and grow an oxide layer by dipping the substrates in solution for at least 20 minutes. Thereafter, to expel oxide layer, the oxidized substrates were kept in 1 % aqueous hydrogen fluoride (HF) solution for 5 minutes at room temperature. Furthermore, the substrates were immersed for 30 sec in the solution which consist of 0.005 M $AgNO_3$ and 4.8 M HF, it leaving the homogeneously dispersed Ag nanoparticles on the substrate surface. The surplus Ag^+ ions were taking out by rinsing the substrate in DI water. Thereafter, etchant solutions (0.15 M H_2O_2 + 4.8 M HF) were prepared and preserve Ag nanoparticles decorated substrates into it for one hour at atmospheric and lightless environment. Dilute HNO_3 solution was used to remove the remnant Ag nanoparticles and then rinsed several times in DI water. The prepared Si substrates upto this step may have some native oxide layer, therefore to remove it the substrates were socked in aqueous 4 % HF. In final step, DI water cleaning is repeated and then uniformly porous silicon substrates were successfully manufactured with one side (Si top surface) deep black while other side having deep gray colour. All of the employed steps are illustrated as a schematic in **Fig. 4.1**.

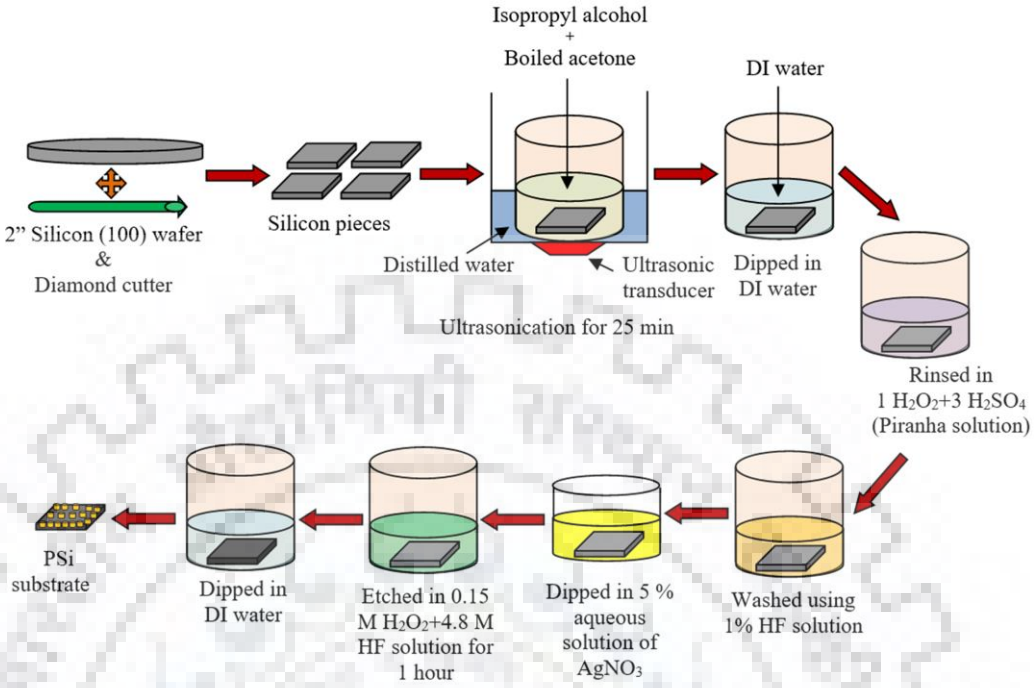

Figure 4.1 Schematic representation of fabrication steps for preparation of porous silicon (PSi) by the metal-assisted chemical etching process.

Subsequently, the tungsten nitride (W_2N) thin film was deposited directly on porous silicon (PSi) and bare silicon substrates using DC reactive magnetron sputtering technique at 100 ºC. At higher deposition temperature, the deposited thin film exhibits low resistance which is not favourable for gas sensing application. During fabrication of W_2N thin films, the DC power on tungsten target was set to 50 watt. The deposition pressure and time for sputtering process were maintained to 10 mTorr and 20 minutes respectively. Argon (Ar) and Nitrogen (N_2) gases were used as sputtering and reactive gas respectively with 4:1 ratio. High nitrogen gas flow leads to insulating film while at very low nitrogen flow the resistance of the film found to be very low. During sputtering process, the thin film formation takes place onto a substrate after nucleation and growth of the material species at the nucleation sites. It can be seen that the morphology of sputtered thin film predominantly depends upon the morphology of substrate used. In case of PSi substrates, material species comes out from the target and stuff the edges of pores along with non-etched (silicon pillar) area. Thereafter, the material deposited on silicon pillar restricts the further stuffing of pores due to self-shadowing effect **[14]**. Thus, the film growth on silicon pillar of PSi substrate was found in the form of nanoballs. However, for bigger pore diameter (of the order of few μm) the self-shadowing effect becomes less dominant and filling of the pores

becomes more, resulting to form a continuous film instead of W_2N nanoballs structure. The pore depth also plays a crucial role on the morphologies of deposited thin films. Moreover, a larger pore depth can promote a thin film with large porosity and affect the thin film morphology. Thus, on increasing the pore depth, a coarse grain structure of W_2N would be developed instead of nanoballs like structure **[14]**.

To ensure about the high quality film deposition, the native oxides and other contaminated species present on the surface of W target were removed by performing a pre sputtering run for 10 minutes. After that, an ultra-thin (~ 5 nm) film of palladium was also deposited on the W_2N structure surfaces using DC magnetron sputtering at RT. For Pd layer, deposition time, deposition pressure and deposition power were kept at 5 sec, 10 m Torr and 50 watt respectively.

4.2.3 Characterizations

The phase formation and orientation of the as deposited W_2N thin films on PSi substrate were studied using X-ray diffractometer at a scan rate of 1°/min. Crystal structural, surface morphology, cross section and elemental information of the Pd/W_2N/PSi structure were characterized by Raman spectroscopy (Horiba Jobin Yvon Lab Ram HR 800 UV), field emission scanning electron microscopy (Carl Zeiss, Ultra plus) and X-ray photoelectron spectroscopy (Perkin Elmer model 1257). In order to perform the in-situ gas sensing measurements, two probe resistivity technique was used along with Kiethley 2400 source meter and Kiethley 2181 A nanovoltmeter.

A custom designed sensing setup of 500 cm^3 volume was assembled with a PID controlled electric heater to carry out the sensing measurements as shown in **Fig. 2.14**. Before the sensing test, a vacuum of the order of 6×10^{-1} Torr was achieved inside the sensing chamber with a rotary pump. Consequently, pure hydrogen (99.99 %) gas was mixed with synthetic air at flow rate of 50 cm^3/min.

4.3. Results and discussion

4.3.1 Structural properties

The XRD pattern of active sensing material (W_2N) deposited onto porous silicon substrate is shown in **Fig. 4.2 (a)**. Presence of peaks at $2\theta = 37.02$ and $2\theta = 73.34$ along with Si substrate peak ($2\theta = 53.02$) confirm the polycrystalline nature of W_2N with (111) and 311 orientations respectively. This crystalline nature can demonstrates as face centred cubic (FCC)

B-1 NaCl type structure (Reference no: -00-025-1257) **[15, 16]**. For W_2N thin film, the dominant (111) orientation is closed packed FCC which having minimum surface energy. Although, the surface energy can be modulated by altering deposition parameters such as substrate temperature, target power and gas ratio. **Fig. 4.2 (b)** shows the Raman spectra of the W_2N thin film deposited on PSi substrate which exhibits the existence of predominant bands at 208, 698 and 800 cm^{-1}**[17]**.

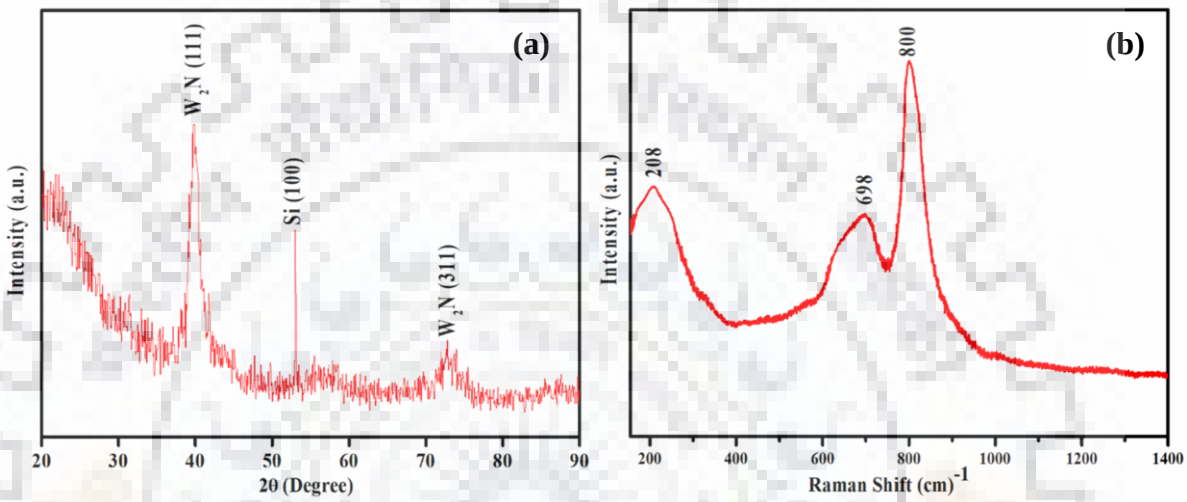

Figure 4.2 (a) XRD pattern at room temperature and **(b)** Raman spectra of W_2N thin film

Due to lacking of related study in literature, the detailed nature of the bonds cannot determine. The information about presence of elements such as tungsten (W), nitrogen (N) and palladium (Pd) in Pd/W_2N structure is deduced from the XPS measurement. A complete XPS estimation was done in the binding energy window 0-1000 eV as shown in **Fig. 4.3 (a)**. The spectral lines related to tungsten (W), nitrogen (N), palladium (Pd), carbon (C) and oxygen (O) are detected at different binding energy values which having a good agreement with the previously reported literature. Oxygen related peaks O 1s and O KLL are affirmed at the binding energy value 530.015 and 972.028 eV respectively which may be due to exposure of the film in atmosphere prior to XPS experiment. The presence of carbon is assigned as C1s electronic state. The characteristic peaks of W 4f, N 1s and Pd 3d are shown in **Fig. 4.3 (b), (c)** and **(d)** which demonstrated the high resolution core level spectra of Pd coated tungsten nitride thin film. **Fig. 4.3 (b)** displays that the spin orbital positions of the 4f electron for W were found at 30.90 eV, 32.97 eV and 35.98 eV which exhibits that W is present in W_2N form in the as-synthesized film. Moreover, the W-N bond in W_2N thin film is confirmed by the occurrence of two peaks at 30.95 and 32.97 eV **[18]**.

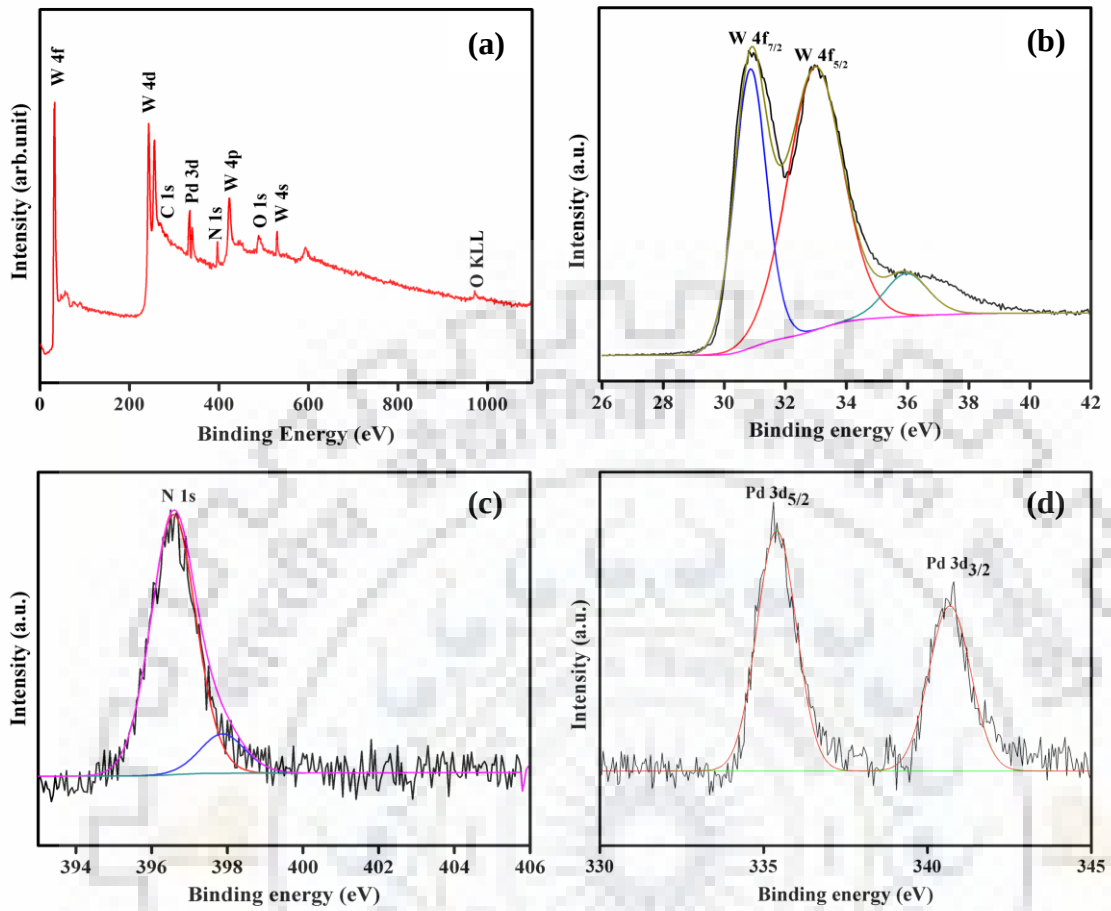

Figure 4.3 (a) X-ray photoelectron spectroscopy (XPS) full scan spectra of the Pd/W_2N thin film, **(b)** W 4f XPS, **(c)** N 1s XPS and **(d)** Pd 3d XPS.

At higher binding energy value the W-O bond related to W 4f are also approved. $W^{+\S}$ ($0 > \S > 4$) state of the tungsten in W_2N is certified by the position of W $4f_{7/2}$ which lies between little bit lower than the W^{+4} (31.2 ± 0.2) eV but higher than W^{+4} (29.8 ± 0.2) eV. The separation between two spins of W $4f_{7/2}$ and $4f_{5/2}$ electrons is found to be the binding energy difference of 2.1 eV. The position of the N1s electron at binding energy scale is at 396.59 eV, which correspond to the nitride ion ($N^{-\S}$) related with the W-N bond. Presence of a hump in N1s peak at 397.95 eV may be caused that nitrogen atoms or molecules exist at the interstitial site of the W_2N. The XPS spectrum of Pd depicts that peaks at 335.34 eV and 340.79 eV are corresponding to electronic transitions of Pd $3d_{5/2}$ and Pd $3d_{3/2}$, respectively **[19]**. The 5.45 eV gap between Pd $3d_{5/2}$ and Pd $3d_{3/2}$ indicates the value of separated spin-orbit doublet, which is in accordance with the literature.

4.3.2 Surface morphology

Fig. 4.4 (a) illustrates the FE-SEM image of as synthesized porous silicon (PSi) substrate and it can be seen that the pores of about 200 nm diameter are almost uniformly distributed all over the surface. For better visualization of pore depth, the cross sectional FE-SEM image of bare PSi substrate is shown in the inset of **Fig. 4.4 (a)**. The average pore depth of metal assisted chemically etched porous silicon substrate was found to be ~ 850 nm.

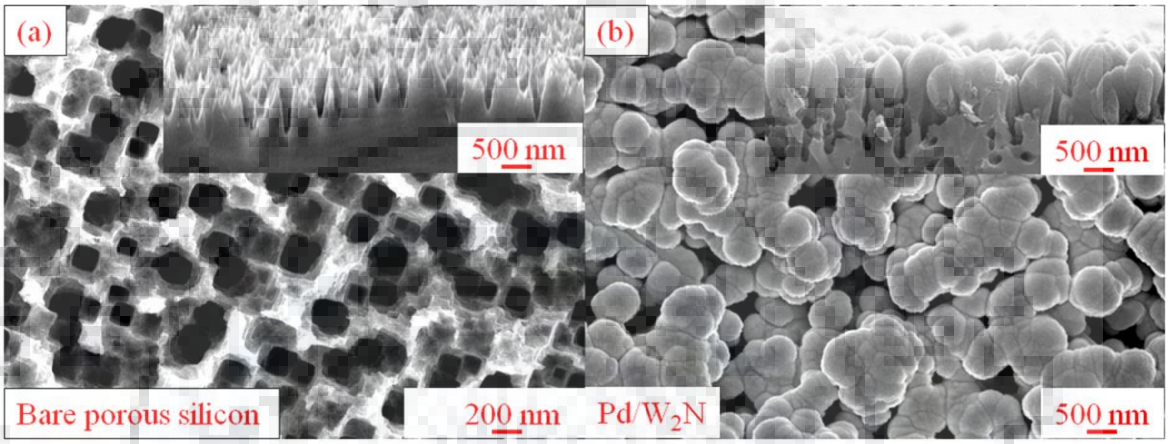

Figure 4.4 (a) FE-SEM surface morphology and inset shows cross-section view of bare porous silicon (PSi) substrate and **(b)** FE-SEM surface morphology of Pd-decorated W_2N sensing layer; inset shows cross-sectional FE-SEM image.

The FE-SEM surface imaging of Pd/W_2N/PSi NBs structure is shown in **Fig. 4.4 (b)**. The uniformly distributed grain growth of the W_2N active sensing material is indicating the porous structure. It can be seen that the nanoballs of W_2N were formed on PSi substrate. The cross-sectional view of Pd/W_2N/PSi displays the thickness of W_2N layer above the pores was estimated to be about ~ 940 nm {inset of **Fig. 4.4 (b)**}. It depicts that the silicon pores were not fully stuffed by W_2N nanoballs. During sputtered deposition, the species coming from the sputtering target follow the pattern of PSi and get deposited on the pore edges and silicon pillars. The stuffing of pores is reduced with time due to self-shadowing effect which caused by the deposited part on silicon pillars. Thus, as a result, the thin film growth takes place on silicon pillar and spherical or nanoballs like structure comes into the picture.

4.3.3 Sensing performance

The sensing performance of chemiresistive gas sensors can be estimated with the observed values of sensor response and response/recovery time which have been discussed in

chapter 1. It is widely accepted that the variation in electrical resistance after exposure to target gas will mainly depends upon the nature of the target gas molecules and nature of majority charge carriers present in the sensing element (thin film) **[20]**. Basically, the reducing gases behave like donors, that resulting to decrease the electrical resistance of the n-type sensing materials. Herein, the resistance starts to decrease after introduction of H_2 (reducing) gas molecules inside the sensing chamber, indicating the n-type nature of the proposed Pd/W_2N sensing device.

It is well recognized that the triggering in sensor response is due to interaction of analyte gas on the surface of active sensing material **[21]**. **Fig. 4.5 (a)** depicts the change in response with error bar for Pd/W_2N/PSi nanoballs (NBs) and the Pd/W_2N/Si thin film structures to different H_2 concentration regime (5-500 ppm) in the synthetic air at RT.

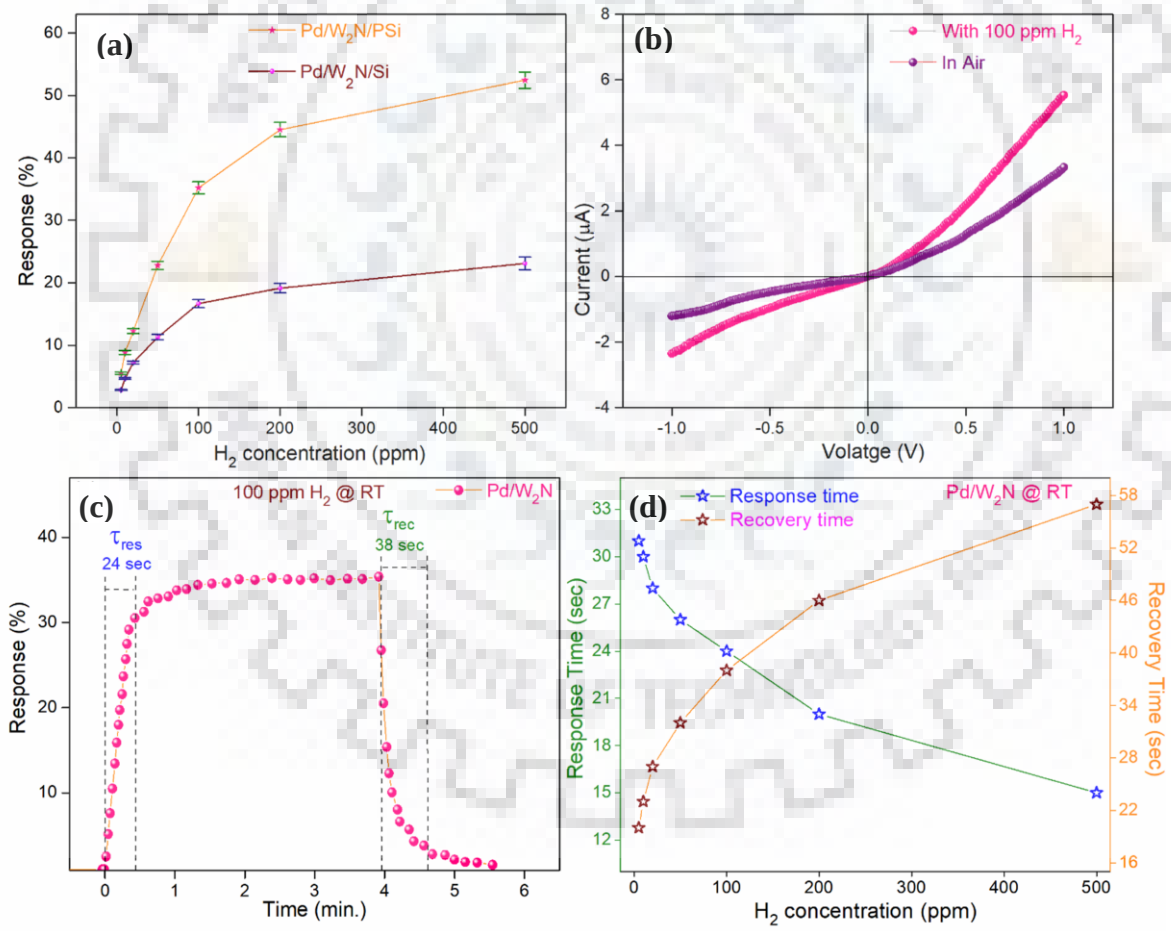

Figure 4.5 (a) Variation of response for Pd/W_2N/PSi and Pd/W_2N/Si structures towards hydrogen gas concentration (5–500 ppm) at RT, **(b)** current-voltage (I–V) characteristics curve of Pd/W_2N nanoballs structure at RT, **(c)** gas response vs. time curve for 100 ppm hydrogen gas at RT, **(d)** response and recovery time curve vs. H_2 gas concentration (5–500 ppm) at RT for Pd/W_2N nanoball structure.

It can be seen that the response value towards H_2 was found to be 35.20 ± 0.98 at 100 ppm level for Pd/W_2N/PSi NBs sensor. Moreover, both sensors are able to detect the trace quantity of H_2 gas down to 5 ppm. These results exhibit the obvious increase in the response with raising the concentration of analyte gas molecules. At RT, about 2 fold sensing response was observed for Pd/W_2N/PSi NBs structure compared to Pd/W_2N/Si thin film structure within the wide detection range (5- 500 ppm). Thus, such type of nanostructures may offer a rapid transfer of movable charge carriers and active sites at the time of adsorption and desorption process of target gas molecules. Therefore, the excellent response characteristic can be acknowledged to highly porous structure and large active surface area of Pd/W_2N NBs structure **[8, 22]**. In order to further explore the resistive characteristics, the I–V test of the Pd/W_2N/PSi NBs structure was accomplished in the absence and presence of 100 ppm H_2 gas in dry air at RT as shown in **Fig. 4.5 (b)**. Here, we observed that the proposed sensing structure reflects the rectifying diode properties such that the electrical conductivity improved after introducing the target gas molecules on top of the sensor surface. It may be due to enhancing the number of free charge carriers (i.e. electrons) upon exposure to hydrogen gas **[23]**. **Fig. 4.5 (c)** shows the sensor response versus time characteristics towards 100 ppm H_2 in dry synthetic air at RT. It can be seen that the response and recovery time were found to be 24 sec and 38 sec respectively. Here, the high active surface area of Pd/W_2N NBs provides a huge number of catalytically active reaction sites on the sensor surface, exhibiting the significant enhancement in detection rate of hydrogen gas **[24]**. For Pd/W_2N NBs sensor, the response and recovery time behavior at various H_2 concentrations (5-500 ppm) were also examined in dry synthetic air at RT {**Fig. 4.5 (d)**}. These results indicate that the response time reduces and recovery time enhances with increasing the exposed concentration of H_2 gas on the sensor surface. It can be documented to the diffusion limited kinetics at comparatively low analyte gas concentration **[25, 26]**. In addition, it may occur due to sluggish desorption rate on the sensor surface at high concentration level of analyte gas molecules. As huge number of target gas molecules can take an additional time to desorb from the top of sensing layer, resulting to improve the recovery time.

Fig. 4.6 (a) shows the sensing selectivity data for Pd/W_2N/PSi and W_2N/PSi sensors towards 100 ppm H_2, H_2S and NH_3 gases in dry synthetic air at RT. It can be seen that the after Pd deposition the sensor is highly selective for H_2 and relatively small change in the response was observed for H_2S and NH_3 gases. This may be due to high catalytic activity of Pd towards H_2 compared to other interfere gases. These results display that the Pd/W_2N/PSi sensor exhibits

the improved response (S.R ~ 35.2 %) to H_2 gas with respect to weak sensor response (S.R < 7 %) for other gases at RT. It can be seen that the proposed sensor is highly selective to H_2 gas at RT. It is well known that the effect of relative humidity (RH) on the device performance has been proposed to act as the critical factor for real field applications. Therefore, the variation of sensor response was examined towards 100 ppm H_2 in dry air for different humidity conditions (dry air -78 %) at RT {**Fig. 4.6 (b)**}.

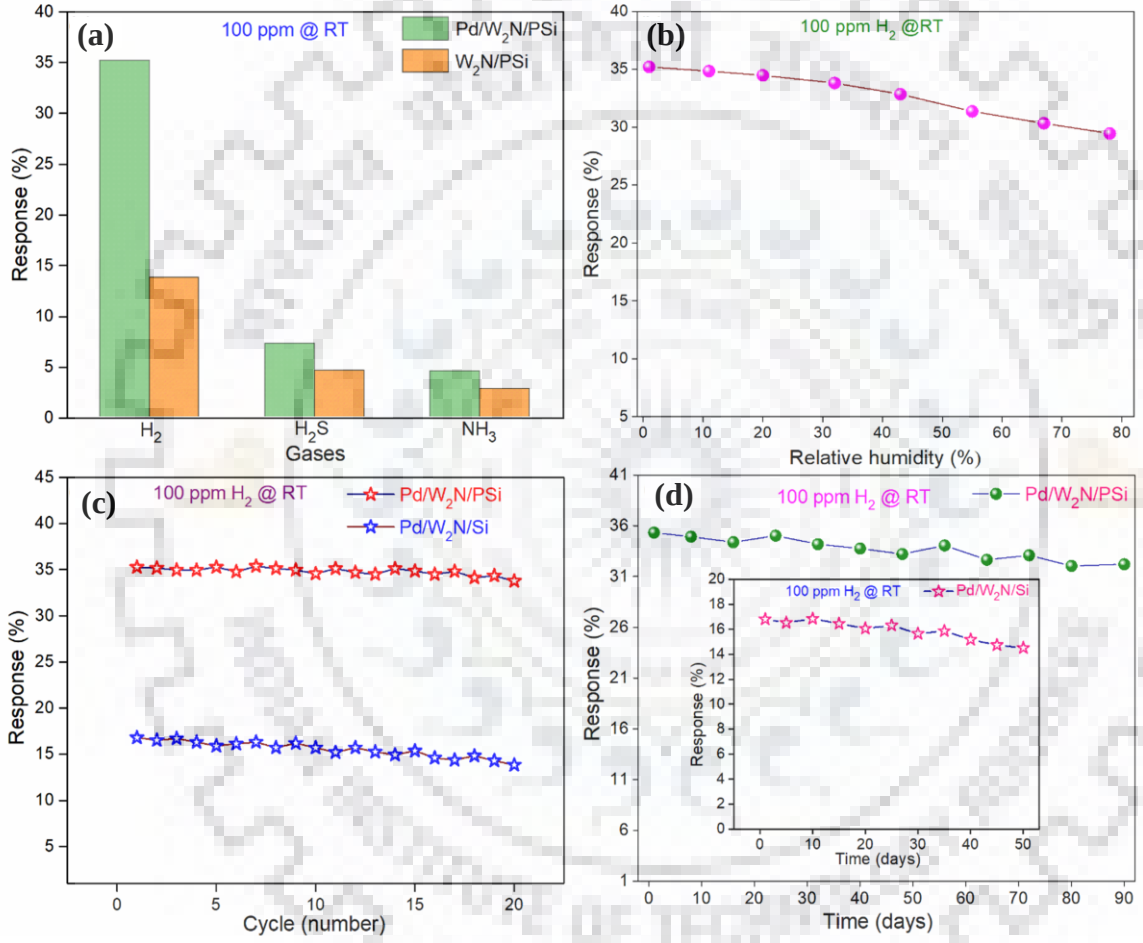

Figure 4.6 (a) Gas selectivity data for Pd/W_2N/PSi and W_2N/PSi structure at RT, **(b)** gas response of Pd/W_2N nanoballs structure to 100 ppm hydrogen in different humidity environments (0–80 RH) at RT, **(c)** show the repeatability test up to 20 cycles and **(d)** shows the response time behaviour for Pd/W_2N structure fabricated on PSi and bare Si substrates respectively.

The results depict that about 14 % declines in the response was noticed at high humidity condition (78 % RH). Here, the continuous decay in sensing response is mainly accredited to the adsorption of more water molecules after exposure to mixed gas on active layer in humid environment **[10]**. Thereafter, these water molecules may restrict the adsorption of analyte gas

molecules on the sensor surface. Thus, the reaction rate between adsorbed oxygen species and water molecules reduced which may donate to decline in baseline resistance and hence declined the sensor response. Therefore, the water vapors can slow down the sensor response by blocking the dissociation of hydrogen gas molecules on the Pd surface **[27, 28]**. However, the reduction in the response under humid environment can be ascribed to the hydroxyl ions (OH^-) adsorption on the top of sensing layer **[8]**. Moreover, the water molecules can perform as an obstruction against the hydrogen adsorption as a result, the migration of H_2 gas molecules on the Pd/W_2N/PSi NBs sensor surface become more difficult **[27]**. Furthermore, the repeatability test for Pd/W_2N/PSi and Pd/W_2N/Si structures to 100 ppm H_2 in dry air was also performed at RT as shown in **Fig. 4.6 (c)**. It can be seen that Pd/W_2N/PSi NBs and Pd/W_2N/Si thin film sensors exhibit 5 % and 17 % decline in the response after 20th cycles, indicating the high reproducibility of the Pd/W_2N/PSi NBs structure as compared to Pd/W_2N/Si thin film structure. Moreover, **Fig. 4.6 (d)** depicts the stability test for both the sensors to 100 ppm H_2 in dry synthetic air at RT. Here, we observed that Pd/W_2N/PSi NBs sensor reveals ~ 7 % decline in the response after 90 days. On the other hand, Pd/W_2N/Si thin film sensor displays ~ 14 % decrease in the response after 50 days. Therefore, these results demonstrate that the Pd/W_2N/PSi NBs sensor indicate almost constant response signal, illustrating the incredible stability of the proposed nanoballs sensor as compared to Pd/W_2N/Si thin film sensor at RT. Here, we have used the porous silicon substrates to influence the surface morphology of metal nitride and increase the active surface area of material and hence increase the reactivity towards target gas molecules **[28]**. Thus, the porous silicon can provide the reproducibility as well as excellent stability to 100 ppm H_2 at RT. Here, all the sensing tests were repeated three times and about 4 % deviation in the sensor performance was observed. Therefore, the nanoballs structure may comprise the new approach to design and construction of nanostructures as an inspiring material for H_2 sensing device applications.

4.3.4 Sensing mechanism

Usually, the origin of sensor response is due to interaction of analyte gas molecules on surface of the active layer is noteworthy **[29]**. For chemiresistive gas sensors, the reaction mechanism can be described using the surface depletion layer model **[30]**. Herein, the adsorption/desorption process of analyte gas molecules taking place on the surface of sensing material played a crucial role in altering the electrical resistance of the sensing layer. For nitride based semiconductor gas sensors **[31, 32]**, the nitrogen vacancies can act as the sorption sites for

analyte gas molecules on top of the sensing layer. Lee et al. reported that the oxygen can be adsorbed at the nitrogen vacancies **[33]**. Therefore, the oxygen sorption can plays a key role in altering the electrical resistance of W_2N materials. Thus, the basic reaction mechanism of n-type W_2N sensing layer for hydrogen gas in dry synthetic air includes the following steps: Firstly, when proposed gas sensor is exposed to air then oxygen molecules can adsorbed on its surface. These oxygen molecules undergo chemisorption process to form oxygen species (O^- and O^{2-}) via capturing the electron from the conduction band of W_2N material **[34]**. **Fig. 4.7** shows the schematic diagram of hydrogen gas sensing mechanism of Pd decorated W_2N nanoballs. Therefore, owing to decrease in carrier concentration, a depletion layer is formed and hence enhanced the initial resistance (R_a) of the sensing layer **[35]**. Secondly, when Pd/W_2N sensor surface is exposed to H_2 then an ultra-thin layer of Pd offers the inferior reaction energy to the H_2 gas molecules. Therefore, due to spill over effect the catalytic reaction of Pd layer dissociate the H_2 gas molecules into H atoms at the interface **[21]**. Here we observed that due to very low (~ 5 nm) thickness of Pd layer there is no significant change in conductivity and hence the electrical resistance of the device remains of the order of kΩ even after Pd coating. Thereafter, these H atoms react with the chemisorbed oxygen species (O^- and O^{2-}), resulting to form the hydroxyl OH^- groups **[36]**. These OH^- groups can again react with H atoms to form H_2O and releasing the free electron back to the W_2N layer.

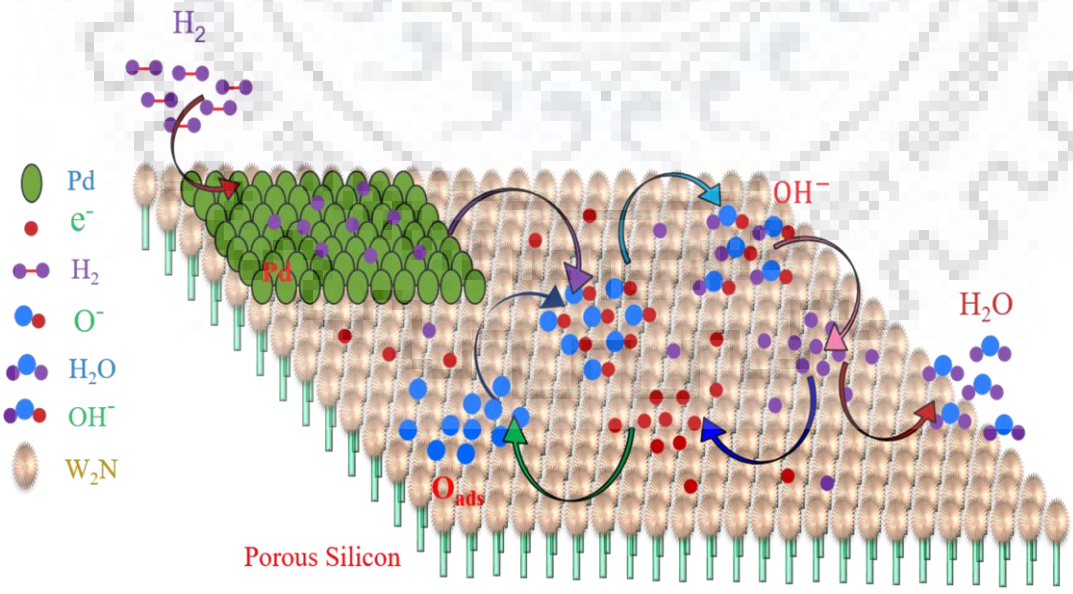

Figure 4.7 Schematic illustration of hydrogen gas sensing mechanism of Pd decorated W_2N nanoballs.

Therefore, the resistance (R_g) offered by surface of the active material start to decline. The whole processes can be illustrated by the following reactions (1-5), occur on the active surface as **[35]**:

$$O_{2(gas)} \rightarrow 2O_{(ads)} \quad (1)$$

$$O_{(ads)} + e^-_{(from\ W_2N)} \rightarrow O^- \quad (2)$$

$$H_{2(gas)} \rightarrow 2H_{(ads)} \quad (3)$$

$$H_{(ads)} + O^- \rightarrow OH^- \quad (4)$$

$$OH^-_{(ads)} + H_{(ads)} \rightarrow H_2O + e^-_{(to\ W_2N)} \quad (5)$$

Furthermore, during the recovery process, the electron concentration starts to decrease in the absence of hydrogen gas molecules, caused to recover the initial resistance of the sensor.

4.4 Conclusions

In summary, we have synthesized Pd decorated W_2N NBs on porous silicon substrate using DC reactive magnetron sputtering technique for room temperature H_2 gas sensing application. The as prepared nanostructure exhibits the remarkable sensing response (35.2 %), good stability (90 days) and excellent repeatability (20^{th} cycles) with quick response and recovery time of 24 sec and 38 sec towards 100 ppm hydrogen in the dry air at RT. Therefore, the porous silicon template may provide a new strategy to construct a simple, inexpensive and robust chemiresistive gas sensor with remarkable properties for low detection (5-500 ppm) of H_2 gas at RT for real field applications.

4.5 References

[1] Schlapbach L., Zuttel A., "Hydrogen-storage materials for mobile applications", *Nature*, **414,** 353-358 (2001).

[2] Kwon H., Lee Y., Hwang S., Kim J. K., "Highly-sensitive H_2 sensor operating at room temperature using Pt/TiO_2 nanoscale Schottky contacts", *Sens. Actuators, B-Chem.*, **241,** 985-992(2017).

[3] Sakintuna B., Lamari-Darkrim F., Hirscher M., "Metal hydride materials for solid hydrogen storage: A review", *Int. J. Hydrogen Energy*, **32**, 1121-1140 (2007).

[4] Samerjai T., Tamaekong N., Liewhiran C., Wisitsoraat A., Tuantranont A., Phanichphant S., "Selectivity towards H_2 gas by flame-made Pt-loaded WO_3 sensing films", *Sens. Actuators, B-Chem.*, **157**, 290-297 (2011).

[5] Jung D., Han M., Lee G. S., "Room-temperature gas sensor using carbon nanotube with cobalt oxides", *Sens. Actuators, B-Chem.*, **204**, 596-601 (2014).

[6] Kumar A., Sanger A., Kumar A., Chandra R., "Fast response ammonia sensors based on TiO_2 and NiO nanostructured bilayer thin films", *RSC Adv.*, **6**, 77636 -77643 (2016).

[7] Wang Y., Liu B., Cai D., Li H., Liu Y., Wang D., Wang L., Li Q., Wang T., "Room-temperature hydrogen sensor based on grain-boundary controlled Pt decorated In_2O_3 nanocubes", *Sens. Actuators, B-Chem.*, **201**, 351-359 (2014).

[8] Chen J., Zhang J., Wang M., Li Y., "High-temperature hydrogen sensor based on platinum nanoparticle-decorated SiC nanowire device", *Sens. Actuators, B-Chem.*, **201**, 402-406 (2014).

[9] Kim K.-S., Chung G.-S., "Novel optical hydrogen sensors based on 3C-SiC membrane and photovoltaic detector", *Sens. Actuators, B-Chem.*, **193,** 42-45 (2014).

[10] Kumar A., Sanger A., Kumar A., Chandra R., "Porous silicon filled with Pd/WO_3-ZnO composite thin film for enhanced H_2 gas-sensing performance", *RSC Adv.*, **7**, 39666-39675 (2017).

[11] Singh N., Kumar A., Kaur D., "Hydrogen gas sensing properties of platinum decorated silicon carbide (Pt/SiC) Nanoballs", *Sens. Actuators, B-Chem.*, **262**, 162-170 (2018).

[12] Sanger A., Kumar A., Kumar A., Jaiswal J., Chandra R., "A fast response/recovery of hydrophobic Pd/V_2O_5 thin films for hydrogen gas sensing", *Sens. Actuators, B-Chem.*, **236**, 16-26 (2016).

[13] Kumar A., Sanger A., Kumar A., Chandra R., "Highly sensitive and selective CO gas sensor based on a hydrophobic SnO_2/CuO bilayer", *RSC Adv.*, **6**, 47178-47184 (2016).

[14] Robbie K., Friedrich L. J., Dew S. K., Smy T., Brett M. J., "Fabrication of thin films with highly porous microstructures", *J. Vac. Sci. Technol., A*, **13**, 1032 (1995).

[15] Prakash R., Rathore B. P. S., Kaur D., "Effect of top electrode material on resistive switching properties of WN based thin films for non-volatile memory application", *J. Alloys. Compd*., **726**, 693-697 (2017).

[16] Kim J. B., Jang B., Lee H. J., Han W. S., Lee D. J., Hong T. E., Kim S. H., "A controlled growth of WN_x and WC_x thin films prepared by atomic layer deposition", *Mater. Lett.*, **168**, 218-222 (2016).

[17] Chakrapani V., Thangala J., Sunkara M. K., "WO_3 and W_2N nanowire arrays for photo electrochemical hydrogen production", *Int. J. Hydrogen Energy*, **34 (22)**, 9050-9059 (2016).

[18] Nandi D. K., Sen U. K., Sinha S., Dhara A., Mitra S., Sarkar S. K., "Atomic layer deposited tungsten nitride thin films as a new lithium-ion battery anode", *Phys. Chem. Chem. Phys.*, **17 (26)**, 17445-17453 (2015).

[19] Shim Y. S., Jang B., Suh J. M., Noh M. S., Kim S., Han S. D., Lee W., "Nano gap-controlled Pd coating for hydrogen sensitive switches and hydrogen sensors", *Sens. Actuators, B-Chem.*, **255**, 1841-1848 (2018).

[20] Sanger A., Kumar A., Kumar A., Chandra R., "Highly sensitive and selective hydrogen gas sensor using sputtered grown Pd decorated MnO_2 nanowalls", *Sens. Actuators, B-Chem.*, **234,** 8-14 (2016).

[21] Wang L., Huang H., Xiao S., Cai D., Liu Y., Liu B., Wang D., Wang C., Li H., Wang Y., Li Q., Wang T., "Enhanced sensitivity and stability of room-temperature NH_3 sensors using core–shell CeO_2 Nanoparticles@Cross-linked PANI with p–n heterojunctions", *ACS Appl. Mater. Interfaces*, **6**, 14131 (2014).

[22] Choi K. I., Hwang S. J., Dai Z., Kang Y. C., Lee J. H., "Rh-catalyzed WO_3 with anomalous humidity dependence of gas sensing characteristics", *RSC Adv.*, **4**, 53130–53136 (2014).

[23] Kumar A., Kumar A., Chandra R., "Fabrication of porous silicon filled Pd/SiC nanocauliflower thin films for high performance H_2 gas sensor", *Sens. Actuators, B-Chem.*, **264**, 10-19 (2018).

[24] Kim K. S., Chung G. S., "Fast response hydrogen sensors based on palladium and platinum/porous 3C-SiC Schottky diodes", *Sens. Actuators, B-Chem.*, **160**, 1232-1236 (2011).

[25] Choi S. J., Chattopadhyay S., Kim J. J., Kim S. J., Tuller H. L., Rutledge G. C., Kim I. D., "Coaxial electrospinning of WO_3 nanotubes functionalized with bio-inspired Pd catalysts and their superior hydrogen sensing performance", *Nanoscale*, **8**, 9159-9166 (2016).

[26] Zhao Z., Knight M., Kumar S., Eisenbraun E. T., Carpenter M. A., "Humidity effects on Pd/Au-based all-optical hydrogen sensors", *Sens. Actuators, B-Chem.*, **129**, 726–733 (2008).

[28] Qi Q., Zhang T., Zheng X., Fan H., Liu L., Wang R., Zeng Y., "Electrical response of Sm_2O_3-doped SnO_2 to C_2H_2 and effect of humidity interference," *Sens. Actuators, B-Chem.*, **134**, 36-42 (2008).

[28] Schechter I., Chorin M. B., Kux A., "Gas sensing properties of porous silicon", *Anal. Chem.*, **67**, 3727-3732 (1995).

[29] Sanger A., Jain P. K., Mishra Y. K., Chandra R., "Palladium decorated silicon carbide nanocauliflowers for hydrogen gas sensing application", *Sens. Actuators, B-Chem.*, **242**, 694-699 (2017).

[30] Guo J., Zhang J., Zhu M., Ju D., Xu H., Cao B., "High-performance gas sensor based on ZnO nanowires functionalized by Au nanoparticles", *Sens. Actuators, B-Chem.*, **199**, 339-345 (2014).

[31] Chitara B., Late D. J., Krupanidhi S. B., Rao C. N. R., "Room-temperature gas sensors based on gallium nitride nanoparticles", *Solid State Commun.*, **150**, 2053–2056 (2010).

[32] Kim S. S., Park J. Y., Choi S. W., Kim H. S., Na H. G., Yang J. C., Lee C., Kim H. W., "Room temperature sensing properties of networked GaN nanowire sensors to hydrogen enhanced by the Ga_2Pd_5 nanodot functionalization", *Int. J. Hydrogen Energy*, **36**, 2313–2319 (2011).

[33] Lee D. S., Lee J. H., Lee Y. H., Lee D. D., "GaN thin films as gas sensors", *Sens. Actuators, B-Chem.*, **89**, 305–310 (2003).

[34] Lupan O., Chai G., Chow L., "Fabrication of ZnO nanorod-based hydrogen gas nanosensor", *Microelectron. J.*, **38**, 1211–1216 (2007).

[35] Abdullah Q. N., Yam F. K., Hassan Z., Bououdina M., "Hydrogen gas sensing performance of GaN nanowires-based sensor at low operating temperature", *Sens. Actuators, B-Chem.*, **204**, 497-506 (2014).

[36] Chen J., Zhang J., Wang M., Li Y., "High-temperature hydrogen sensor based on platinum nanoparticle-decorated SiC nanowire device", *Sens. Actuators, B-Chem.*, **201**, 402-406 (2014).

Chapter 5

Structural, Corrosion and Mechanical Properties of the Chromium Tungsten Nitride ($Cr_{1-x}W_xn$) Nanocomposite Thin Films

CHAPTER 5

STRUCTURAL, CORROSION AND MECHANICAL PROPERTIES OF THE CHROMIUM TUNGSTEN NITRIDE ($Cr_{1-X}W_XN$) NANOCOMPOSITE THIN FILMS

5.1 Introduction

Chromium (Cr) and titanium (Ti) based binary metal nitride thin films have been extensively used as corrosion and wear resistance protective coatings due to their excellent mechanical and tribological properties **[1]**. Protective thin films enhance the lifetime of the tools or machine's parts and prevent the surface from the affecting environments. Extending the applications lifetime and performance can be beneficial to the cost reduction. In spite of reflecting these tremendous properties, binary metal nitride systems are not sufficient for excellent performance in such applications which required more hardness and better oxidation resistance **[2]**. Properties of binary metal nitrides are also degrade at high temperature **[2, 3]**. In order to overcome these complications and to enhance the properties like hardness, elastic modulus, surface morphology, corrosion stability, lubrication, adhesion and to adjust the parameters such as grain size, lattice constant, crystal orientation and internal stress, other metals like Mo, Al, Ta and W are alloyed **[4, 5]**. After alloying the other metal, binary nitride systems become ternary metal nitride system. Due to covering a wide spectrum of physical and chemical properties, the thin film based on ternary metal nitride are used in a variety of applications like decorative, protective and hot corrosion resistive coatings **[6]**.

However, CrN thin films are most promising material regarding future applications **[7-9]**. But CrN thin films start to oxidize near about the temperature of 700 ºC and as a result performance becomes worse. Thus, fabrication of CrN based ternary coatings such as Cr-Mo-N, Cr-Ti-N, Cr-Al-N, Cr-Si-N and Cr-W-N have been reported and successfully utilized for various applications in harsh environment **[10-12]**. These thin films can be deposited using various physical vapour deposition techniques such as cathodic arc evaporation, ion beam assisted deposition and magnetron sputtering **[13, 14]**. Magnetron sputtering has more advantage due to uniformity and good adhesion of deposited films on the substrate, which are required for such applications. Apart from the addition of other metal into CrN matrix and fabricate a ternary metal nitride, the concentration of the alloying metal and material composition also play a significant role on the material performance.

In present study, the chromium tungsten nitride ($Cr_{1-x}W_xN$) thin films were fabricated using magnetron sputtering technique and investigate the effect of W content on the structural, corrosion and mechanical properties. Selection of tungsten (W) as alloying metal into CrN matrix is due to its superior properties and compatibility with binary nitrides. To date, the related studies on the effect of W content in CrN based ternary system on the corrosion rate along with

mechanical properties are very rare. The addition of W atoms in CrN matrix leads to improved microstructure and mechanical properties. The decrement in corrosion rate along with enhanced mechanical properties of $Cr_{1-x}W_xN$ thin films has shown the potential in several applications such as optical, microelectronic, glass moulding, solid lubrication and protective coatings for cutting tools.

5.2 Experimental details

In this study, the chromium tungsten nitride ($Cr_{1-x}W_xN$) thin films were deposited on silicon (100) substrate at 400 ºC temperature using reactive DC magnetron co-sputtering in which two separate targets (Cr and W) were sputtered simultaneously. It was also found that lower deposition temperature results in poor crystallinity of the thin films while polycrystalline nature occurs at higher temperature. Both the targets were made of very high purity (99.999%, Excel Metal & Engg. Industries, India) and the dimensions of 50 mm diameter and 3 mm of thickness. Total five samples were fabricated with increasing W content ($0 < x < 0.61$) and named as S-1 to S-5. The silicon substrates were initially cleaned thoroughly in an ultrasonic bath with a mixture of distilled water and trichloroethylene in 4:1 ratio and then washed using boiled acetone. Prior to deposition, the chamber was evacuated to a base pressure of the order of 2×10^{-6} Torr and then backfilled with argon and nitrogen gas to achieve desired deposition pressure of 10 m Torr. Target to substrate distance was fixed at 5 cm for both sputtering targets (Cr and W) with off axis geometry. No post-annealing was done after deposition **[15]**. Both the targets were sputtered in the presence of 50% Ar and 50% N_2 gas mixture. Variation in nitrogen flow can change the dominant orientation of the deposited thin film. The target power for chromium was typically set to 80 watt, while tungsten target power was varied. Before every sputtering run, both the targets have been pre-sputtered for 5 min in order to ascertain the same state of the targets. The substrate holder was rotated at 20 rpm in a horizontal plane to achieve a uniform film composition and thickness. The deposition time for all thin films was set to 30 minutes.

The crystallinity and orientation of $Cr_{1-x}W_xN$ thin films were studied using a Bruker AXS-D8 advanced X-ray diffractometer with CuKα (1.54 Å) radiations in θ-2θ geometry at a scan speed of 1º/min. Surface morphology and topography was studied using field emission scanning electron microscopy (FE-SEM) FEI Quanta 200F and atomic force microscopy (AFM) NT-MDT: NTEGRA model respectively. The elemental composition of thin films was determined using the energy dispersive X-ray analysis (EDAX) attached with FE-SEM. In order to analyze the corrosion rate of as synthesized $Cr_{1-x}W_xN$ thin films, an electrochemical

experiment was performed for each thin film. The electrochemical measurements were conducted using Gamry instrument; model PCI 4, interface 1000 potentiostat connected with a corrosion cell of 0.79 cm^2 exposed area in 3.5 wt. % NaCl aqueous solution at room temperature. The corrosion cell consists of three electrodes in which thin film acted as a working electrode, while a standard calomel electrode and a platinum rod served as reference and counter electrodes respectively. Thereafter, Potentiodynamic polarization tests were carried out with a scan rate of 1 mV/s. Tafel polarization curves were obtained at the voltage ranging from - 0.25 to + 0.25 V with respect to the open circuit potential (OCP). Mechanical properties were measured using the Micro materials Nanotest system (Wrexham, UK) at room temperature. The same amount of load (0.5 mN) was applied to all the samples at a constant loading rate of 0.05 mNs^{-1} to compare their mechanical properties. At least 6 independent indentations were performed and the data were averaged to minimize the irrespective noise and variations.

5.3 Results and discussion

5.3.1 Structural properties, surface morphology and composition

Fig. 5.1 shows the XRD pattern of the $Cr_{1-x}W_xN$ ($0 < x < 0.61$) thin films deposited onto Si (100) substrate and revealed the presence of (111) orientation along with preferred (200) reflection, which can assigned to FCC B-1 NaCl phase **[4, 16]**.

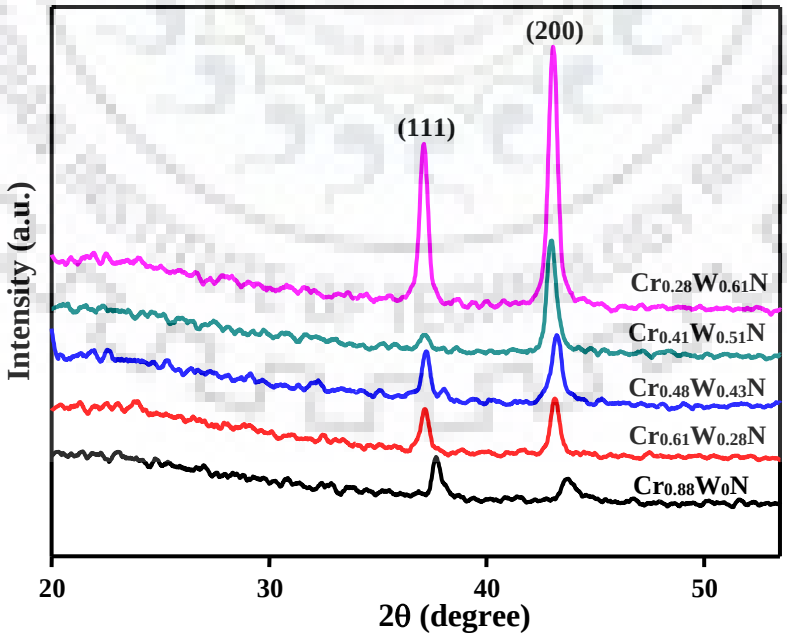

Figure 5.1. XRD pattern of all $Cr_{1-x}W_xN$ thin films with ($0 < x < 0.61$).

In XRD pattern, it is also seen that the diffraction peaks of $Cr_{1-x}W_xN$ thin films were shifted towards lower diffraction angle with an increase in W content. This shift indicates the

increase in lattice constant from 4.129 Å to 4.182 Å with increasing W content as shown in **Fig. 5.2**. Bao-Shun Yau et al. reported that the enhancement in lattice constant can be explained by the fact that Cr, W and/or N atoms incorporated in interstitial positions and then form a solid solution phase of $Cr_{1-x}W_xN$, therefore as a result the lattice constant increases **[17]**. Scherrer formula is used to calculate the crystallite size of the $Cr_{1-x}W_xN$ thin films.

Fig. 5.2 demonstrates the variation of crystallite size of $Cr_{1-x}W_xN$ thin films as a function of W content in which crystallite size decreases from 31.2 nm to 15.2 nm with the W addition up to 43.6 %, beyond this W concentration value the crystallite size led to increasing.

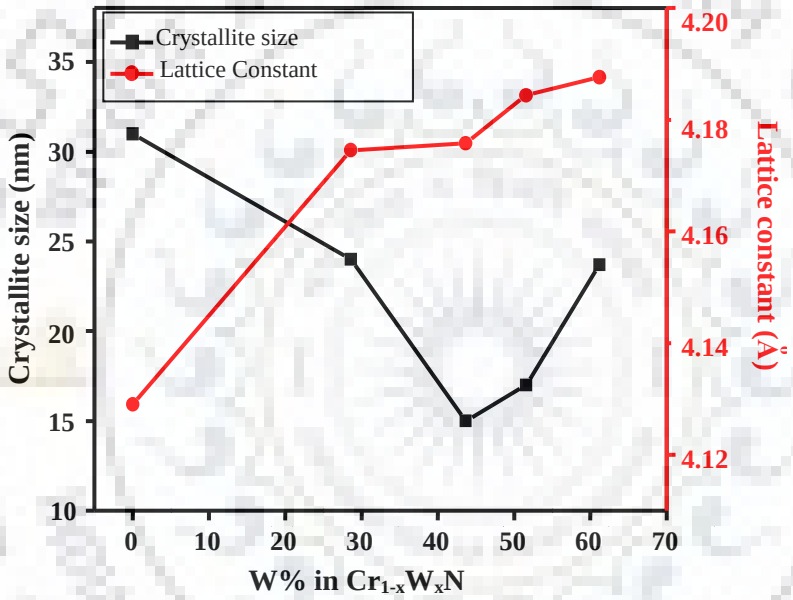

Figure 5.2. Crystalline size and lattice constant as a function of W %.

The reduction of crystallite size may be due to high kinetic energy and the mobility of the depositing atoms. The kinetic energy of the depositing atoms/molecules depends upon the target power and has been considered as a major factor that decides the adatoms mobility and formation of nucleated clusters. High power results higher sputter rate and higher kinetic energy of depositing atoms, therefore nucleation rate is enhanced and the films with reduced grain size is formed. Thus, grain refinement has been achieved due to increase in nucleation rate that caused by high power on tungsten target. As the power on W target reached beyond to 40 watts, the kinetic energy of incorporated W atoms increase the probability of collision with Cr and N atom on the surface of the depositing film. Due to collisions, there could be a sufficient loss of kinetic energy of adatoms during deposition, therefore mobility and diffusion of the atoms become lower

and a coarse grain structure developed. Bao-Shun Yau et al. and wuhrer et al. have been verified these results for $Cr_{1-x}W_xN$ thin films **[17, 18]**.

Apart from XRD results, the FE-SEM and AFM images also confirmed that grain size of the films decreases to $Cr_{0.48}W_{0.43}N$ thin film and then approaches toward larger grain size with the further addition of W content as shown in **Fig. 5.3**. It was also observed that the grain size determined by XRD is smaller than the grain size determined by FE-SEM **(Table 5.1)**. This difference in grain size was due to the fact that AFM and FE-SEM show agglomeration of the particles however XRD gives an average mean crystallite size. Data from XRD and FE-SEM/AFM can be accepted by the fact that smaller particles have a large surface energy and therefore, tend to agglomerate faster and grow into larger grains.

Table 5.1. XRD, FE-SEM, EDAX and AFM details of $Cr_{1-x}W_xN$ thin films.

Sample name	Chemical composition (At %)		Grain size (nm)		Lattice constant (Å)	Surface roughness (nm)
	Cr	W	XRD	SEM		
$Cr_{88.4}W_0N$ (S-1)	88.4	0	31.1	65.2	4.129	14.81
$Cr_{61.9}W_{28.6}N$ (S-2)	61.9	28.6	24.6	51.3	4.144	11.88
$Cr_{48.2}W_{43.6}N$ (S-3)	48.2	43.6	15.2	32.7	4.175	2.11
$Cr_{41.3}W_{51.5}N$ (S-4)	41.3	51.5	17.2	38.9	4.184	7.92
$Cr_{28.5}W_{61.2}N$ (S-5)	28.5	61.2	23.7	50.2	4.187	9.61

For the quantitative evaluation of surface topography, the average roughness (R_{avg}) of all the thin films was obtained from AFM scans over the substrate areas of 1μm × 1 μm, three times at different spot for each thin film by using the relationship,

$$R_{avg} = \frac{1}{N} \sum_{i=1}^{N} |Z_i - \bar{Z}|$$

where, N is the number of surface height data and $\bar{Z}$ is the mean-height distance.

It was found that the surface roughness of $Cr_{1-x}W_xN$ thin films strongly influenced by the W content. The lowest value of surface roughness 2.11 nm was achieved for S-3 sample. As the W content is being increased beyond 43.6 %, the induced surface roughness of the film enhanced. The variation of the surface roughness explained in terms smoothness of the film. The kinetic

energy of the depositing atom strongly affects the adatoms mobility and formation of the nucleated clusters, which in turn affect the microstructure and surface morphology of the films.

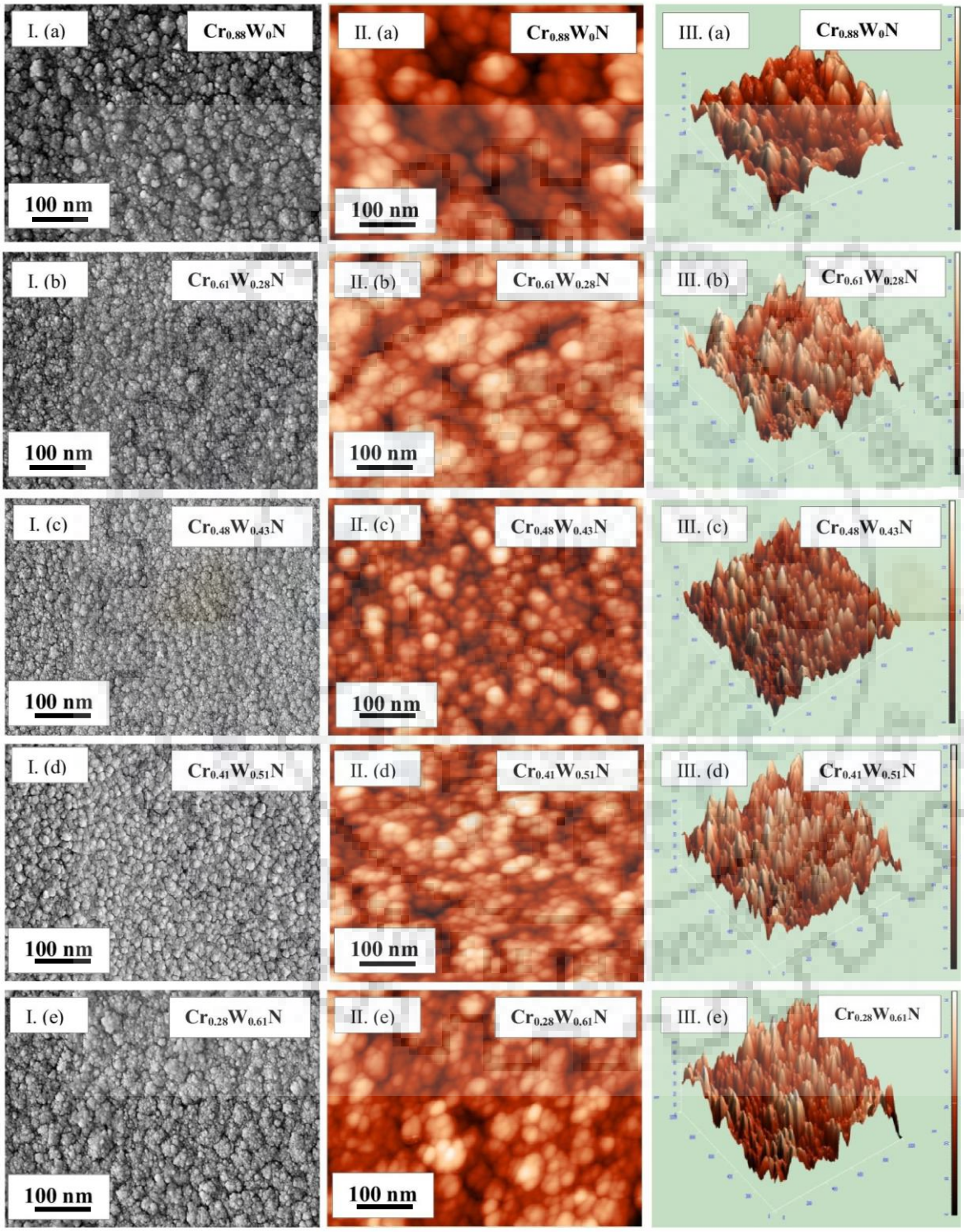

Figure 5.3. **I (a)-(e)** FE-SEM images, **II (a)-(e)** AFM 2-D images and **III (a)-(e)** AFM 3-D images of the thin films abbreviated as S-1, S-2, S-3, S-4 and S-5.

As the power increases, the sputtered atoms get more kinetic energy and adatoms mobility, thus nucleation rate become enhanced. High nucleation rate reduces the self-shadowing effect therefore, the atoms can migrate faster on the surface of the substrate. Enhanced adatoms mobility encourages a more even deposition, thus there is a decrease in surface roughness. At the power higher than 40-watt, depositing atoms get sufficient energy that they could leave the sites and disturb the evenness of film and as a result the surface roughness of grown films increased; this variation was also explained by others **[18]**. Modification of surface roughness can also described using crystallite size. As the crystallite size decreases surface roughness would also decrease due to decline in the relative grain height therefore, small grain size results low surface roughness. **Table 5.1** lists all the parameters which were calculated by XRD, FE-SEM and AFM techniques.

Fig. 5.4 shows the stoichiometric ratio of chromium, tungsten and nitrogen versus power on tungsten target. The composition of the thin films is given in **Table 5.1**, which shows the chromium content decreases and tungsten content increases with the power on the W target. As the power on W target increased, more W atoms were sputtered out from the target which replace the Cr atoms. The nitrogen content was observed almost invariant for all films and it may be due to fix amount of N_2 gas flow during deposition.

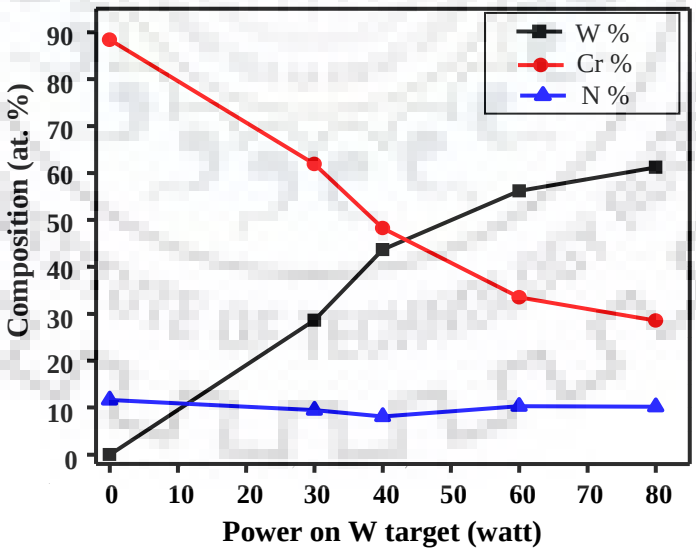

Figure 5.4 Relative composition of the Cr, W and N with the power on W target.

5.3.2 Electrochemical properties

Electrochemical techniques widely used for the kinetics study of the electrochemical process in a specific environment. Tafel Potentiodynamic polarization curves of all $Cr_{1-x}W_xN$

thin films were estimated from the testing of samples in a 3.5% NaCl solution in the open air at room temperature as shown in **Fig. 5.5**.

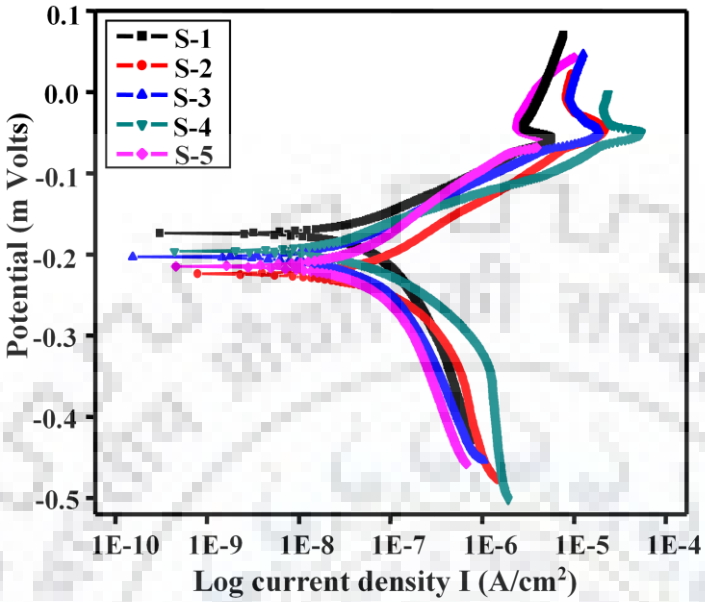

Figure 5.5. Potentiodynamic polarization curves for all the S-1, S-2, S-3, S-4 and S-5 thin films.

The performance of protective coating in terms of coating material degradation due to chemical reaction from the relative environment can be described by corrosion rate. Corrosion potential (E_{corr}) and corrosion current density (I_{corr}) were measured from the intersection of the anodic and cathodic Tafel curves using the Tafel extrapolation method as shown in **Table 5.2**. The shifting of Tafel polarization curves towards the region of lower current density confirms the good corrosion resistance of thin films. Only a factor 3 is estimated between the lowest and highest I_{corr}, it could be due to uncertainly inherent to the Tafel extrapolation method. Corrosion rate was determined using the formula, CR (mpy) = 0.13 I_{corr} (eq. wt.)/d, where eq. wt. and d is the equivalent weight of the material of thin film in grams and density of the films in g/cm^3, respectively. The unit of corrosion rate was converted from mpy (miles penetration per year) to µmy (micrometre penetration per year) using the formula 1 mpy = 25.4 µmy **[19]**. The lowest corrosion rate was found 0.398 µmy in S-3 sample compared to other thin films, i.e. S-3 will degrade only 39.8 nm per year. This corrosion rate value falls in the outstanding region (< 25 µm per year) which was suggested by M. G. Fontana **[19]**. Surface roughness plays a very significant role on the corrosion rate of the surface roughness trend. Modification of corrosion rate of $Cr_{1-x}W_xN$ thin films of lower roughness could be due to the fact that lower roughness provides the higher ratio of real surface area and projected area along with lower inhomogeneous

surface. Inhomogeneities on the surface might responsible for weak points that cause corrosive attacks **[20]**.

Table 5.2. Potentiodynamic measurement data of the $Cr_{1-x}W_xN$ thin films.

Sample name	W%	I_{corr} (nA/cm^2)	E_{corr} (mV)	Corrosion rate (µmy)
(S-1)	0	240.66	-174	1.248
(S-2)	28.6	218.00	-224	1.037
(S-3)	43.6	75.66	-194	0.398
(S-4)	51.5	92.33	-202	0.497
(S-5)	61.2	158.00	-215	1.078

Fig. 5.6 depicts the rate of corrosion behaviour as a function of W content. The rate of corrosion and surface roughness of the $Cr_{1-x}W_xN$ thin films decreases with the incorporation of W content in CrN lattice beyond 43.6 %. As this occurs, it is expected that the electrolyte penetrates less easily into the $Cr_{1-x}W_xN$ thin film. Apart from the surface roughness, the enhancement of corrosion rate may be due to improved covalent bonding character of $Cr_{1-x}W_xN$ thin film at 43.6 % W concentration.

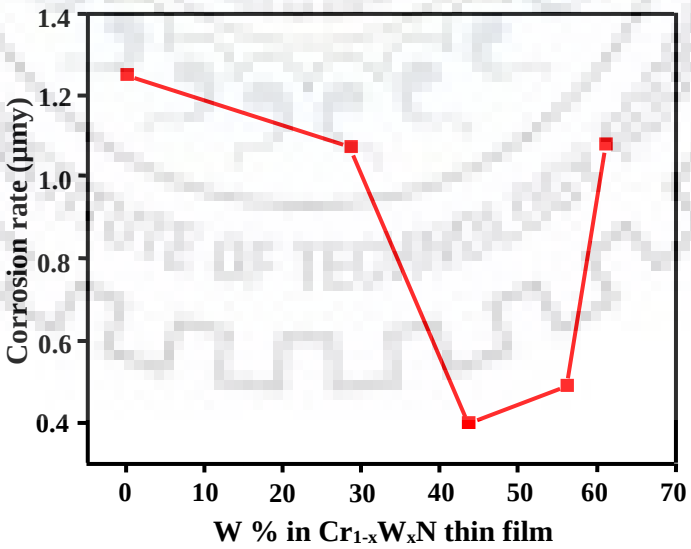

Figure 5.6 Corrosion rate as a function of W % for all the thin films S-1, S-2, S-3, S-4 and S-5.

5.3.3 Mechanical properties

Mechanical properties of the $Cr_{1-x}W_xN$ thin films are studied using Nanoindentation technique. The important details of Nanoindentation have been given in chapter 2.

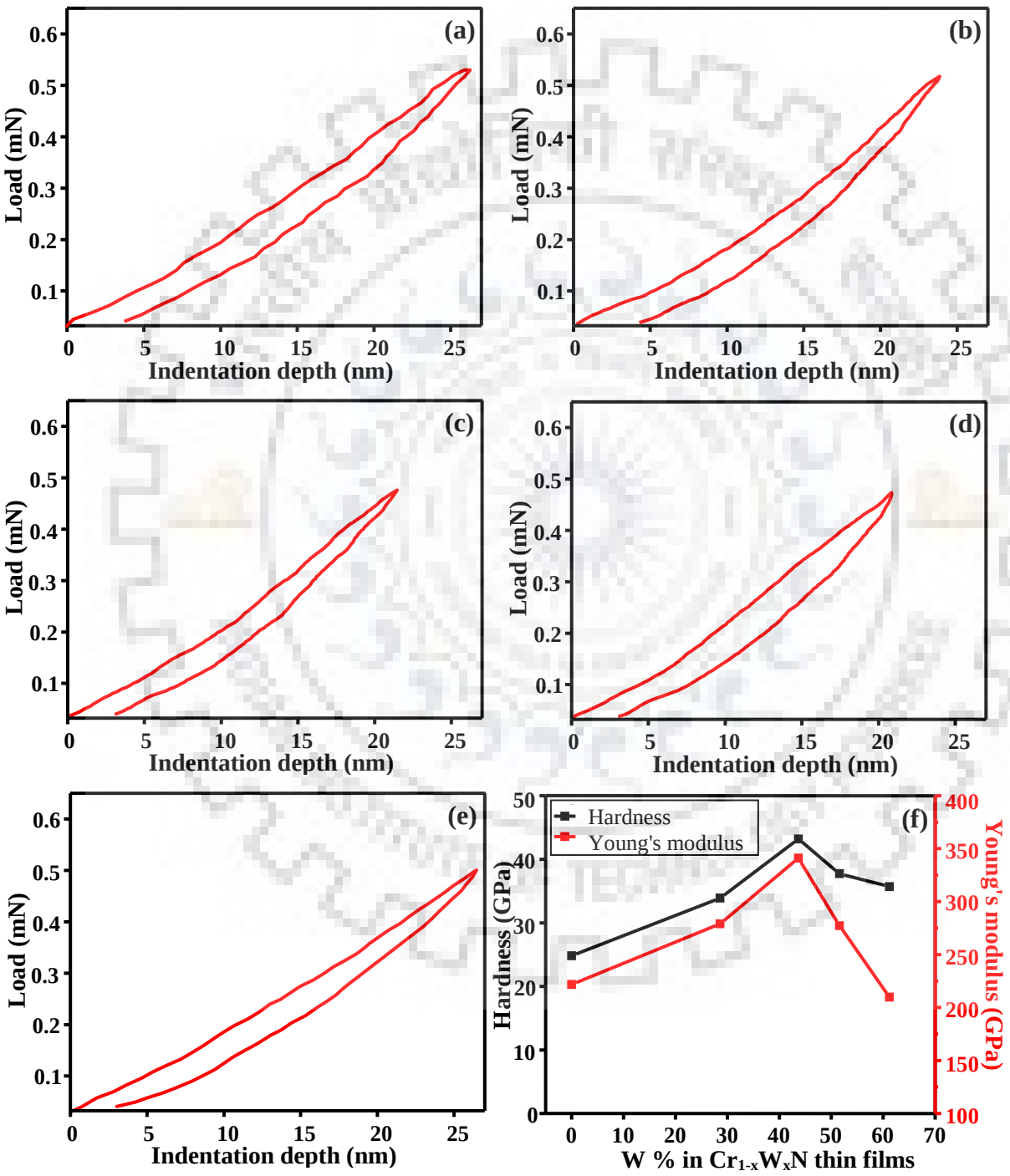

Figure 5.7 (a)-(e) Load versus depth curves and **(f)** Hardness and elastic modulus as a function of W % of all the thin films S-1, S-2, S-3, S-4 and S-5.

Hardness (H) and reduced elastic modulus (E_r) have been measured by directly calculating the physical dimensions of the indentation using the standard method suggested by Oliver and Pharr at room temperature **[21, 22]**. **Fig. 5.7 (a)-(e)** is showing the loading and unloading curves for S-1 to S-5 samples respectively. The hardness and reduced elastic modulus are represented in the **Fig. 5.7 (f)** as a function of tungsten content in $Cr_{1-x}W_xN$ thin films. Other important mechanical parameters such as plasticity index (H/E_r) and resistance to plastic deformation (H^3/E_r^2) also determined and listed in **Table 5.3**.

Table 5.3. Mechanical parameters of the $Cr_{1-x}W_xN$ thin films measured by Nanoindentation.

Sample name	Hardness (GPa)	Elastic modulus E_r (GPa)	H/E_r	H^3/E_r^2 10^{-2} (GPa)
(S-1)	24.80	221.78	11.18	31.01
(S-2)	33.88	279.06	12.14	49.93
(S-3)	43.18	341.02	12.66	69.22
(S-4)	37.73	277.24	13.60	69.87
(S-5)	35.69	209.80	17.01	103.28

The measured value of hardness and elastic modulus of S-1 sample were 24.80 GPa and 221.78 GPa, respectively. In S-2 sample, as W content increases up to 28.6 % the hardness and elastic modulus values are increased rapidly up to 33.88 GPa and 279.06 GPa respectively. Hence, the hardness and elastic modulus are increased 73.19 % and 79.47 %, respectively. The maximum hardness of 43.18 GPa and elastic modulus of 341.02 GPa are observed for S-3 sample as the W content is 43.6 %. Thereafter, the hardness start to decrease as W content increase. It was observed that both the hardness and elastic modulus follow the same trend as a function of W %. Bao Shun Yau et al. has reported that the mechanical properties are widely influenced by the change in charge distribution between W, Cr and N ions **[17]**. Higher covalent bonding of $Cr_{1-x}W_xN$ thin films exhibits higher hardness then that of more ionic bonding of CrN **[17]**.

The variation in hardness for all the sample can explained by Hall-Petch relation for hardness, which is written below,

$$H = H_0 + \frac{k_{gb}}{\sqrt{d}}.$$

where, H is resultant hardness, d is the crystallite size, H_0 and k_{gb} are the appropriate constants associated with the hardness measurements. As the load applied on indenter, it penetrates into thin film and generates some dislocations inside the crystal. Hardness depends upon the movement of the dislocation from one grain to another grain, therefore easy movement of dislocation implies to low hardness. Grain boundaries in thin film are behaved like as barriers that hinder the movement of dislocations from one grain to another grain. The smaller size of grains attributed to restriction in the dislocation movement due to more grain boundary volume, thus high hardness achieved by reduction in grain size. Apart from the Hall-Petch relation, residual stress in the thin film also plays a crucial role on hardness. Higher compressive residual stress is responsible for high hardness and tensile stress results softness. R. Whurer et. al. has reported that any doped atom larger than the host atom it substitutes, generates compressive strain on the surrounding crystal lattice **[18]**. In our case, the atomic radius of W atom (0.169 nm) is larger than the atomic radius of the Cr atom (0.144 nm). Incorporation of W atoms up to 43.6 % in CrN matrix at increase compressive stress results the hardness increases. Beyond the 43.6 % W, the films exhibit softness comparatively which may be due to dominating tensile stress over compressive stress. The plasticity index (H/E_r) and resistance to plastic deformation (H^3/E_r^2) are also important mechanical parameters for calculating the wear resistance and toughness, respectively. The H/E_r and H^3/E_r^2 values for $Cr_{1-x}W_xN$ thin films are varied in the range (0.1118 - 0.1701) GPa and (0.3101 - 1.0328) GPa respectively, which indicate the presence of better wear resistance and toughness. Due to high hardness, elastic modulus and good wear resistance $Cr_{1-x}W_xN$ thin films are promising protective thin films.

5.4 Conclusions

In summary, we have systematically investigated the effect of tungsten content on structural, corrosion and mechanical properties of $Cr_{1-x}W_xN$ ($0 < x < 0.61$) thin films. XRD pattern revealed that $Cr_{1-x}W_xN$ films were developed as FCC B-1 NaCl phase with (200) preferred orientation. The XRD peaks shift towards the lower angle with increasing W content, which attributed by the expansion of lattice due to solid solutioning of W in CrN matrix. The crystallite size decreased with increased W content up to 43.6 % due to induced high nucleation rate and reduction of self-shadowing effect. Further increase in W content results coarse grained structure. The lowest corrosion rate 39.8 nmy was achieved for S-3 thin film. Nanoindentation tests revealed that the films exhibit improved mechanical properties such as hardness and elastic modulus after alloying W metal. Low surface roughness (2.11 nm), best corrosion rate (39.06

nmy), highest hardness (43.18 GPa) and elastic modulus (341.02 GPa) were achieved in $Cr_{0.48}W_{0.43}N$ thin film. The alloying of W would be great technological interest in order to raise the performance of CrN thin films as protective coatings due to enhancement of structural, surface morphology, electrochemical and mechanical properties.

5.5 References

[1] Kim G. S., Lee S. Y., Hahn J. H., Lee B. Y., Han J. G., Lee J. H., Lee S. Y., "Effects of the thickness of Ti buffer layer on the mechanical properties of TiN coatings", *Surf. Coat. Technol.*, **171**, 83-90 (2003).

[2] Zeng X. T., Zhang S., Sun C. Q., Liu Y. C., "Nanometric-layered CrN/TiN thin films: Mechanical strength and thermal stability", *Thin Solid Films*, **424**, 99–102 (2003).

[3] Mayrhofer P. H., Willmann H., Mitterer C., "Oxidation kinetics of sputtered Cr-N hard coatings", *Surf. Coatings Technol.*, **146**, 222–228 (2001).

[4] Hones P., Consiglio R., Randall N., Leacutevy F., "Mechanical properties of hard chromium tungsten nitride coatings", *Surf. Coatings Technol.*, **125**, 179–184 (2000).

[5] Regent F., Musil J., "Magnetron sputtered Cr-Ni-N and Ti-Mo-N films: Comparison of mechanical properties", *Surf. Coatings Technol.*, **142**, 146–151 (2001).

[6] Sundgren J. E., Hentzell H. T. G., "A review of the present state of art in hard coatings grown from the vapor phase", *J. Vac. Sci. Technol*, **A4**, 2259–2279 (1986).

[7] Bull S. J., Jones A. M., "Multilayer coatings for improved performance", *Surf. Coatings Technol.*, **78**, 173–184 (1996).

[8] Hones P., Zakri C., Schmid P. E., Lévy F., Shojaei O. R., "Oxidation resistance of protective coatings studied by spectroscopic ellipsometry", *Appl. Phys. Lett.*, **76**, 3194–3196 (2000).

[9] Panjan P., Navinšek B., Cvelbar A., Zalar A., Milošev I., "Oxidation of TiN, ZrN, TiZrN, CrN, TiCrN and TiN/CrN multilayer hard coatings reactively sputtered at low temperature", *Thin Solid Films*, **281**, 298–301 (1996).

[10] Banakh O., Schmid P. E., Sanjinés R., "High-temperature oxidation resistance of $Cr_{1-x}Al_xN$ thin films deposited by reactive magnetron sputtering", *Surf. Coatings Technol.*, **163**, 57–61 (2003).

[11] Kim G. S., Lee S. Y., "Microstructure and mechanical properties of AlCrN films deposited by CFUBMS", *Surf. Coatings Technol.*, **201**, 4361– 4366 (2006).

[12] Saha R., Inturi R. B., Barnard J. B., "Structural and mechanical characterization of Cr-Ta-N hard coatings prepared by reactive magnetron sputtering", *Surf. Coatings Technol.*, **82**, 42–47 (1996).

[13] Choi E. Y., Kang M. C., Kwon D. H., Shin D. W., Kim K. H., "Comparative studies on microstructure and mechanical properties of CrN, Cr–C–N and Cr–Mo–N coatings", *J. Mater. Process. Technol.*, **187**, 566–570 (2007).

[14] Wu F. B., Tien S. K., Duh J. G., "Manufacture, microstructure and mechanical properties of CrWN and CrN/WN nanolayered coatings", *Surf. Coatings Technol.*, **200**, 1514–1518 (2005).

[15] Barman R., Kaur D., "Leakage current behavior of $BiFeO_3/BiMnO_3$ multilayer fabricated by pulsed laser deposition," *J. Alloys Compd.*, **644**, 506–512 (2015).

[16] Kaushal A., Choudhary N., Kaur N., Kaur D., "VO_2-WO_3 nanocomposite thin films synthesized by pulsed laser deposition technique", *Appl. Surf. Sci.*, **257**, 8937–8944 (2011).

[17] Yau B. S., Chu C. W., Lin D., Lee W., Duh J. G., Lin C. H., "Tungsten doped chromium nitride coatings", *Thin Solid Films*, **516**, 1877–1882 (2008).

[18] Wuhrer R., Yeung W. Y., "Grain refinement with increasing magnetron discharge power in sputter deposition of nanostructured titanium aluminium nitride coatings", *Scr. Mater.*, **50**, 813–818 (2004).

[19] Fontana M. G., "Corrosion engineering", *Macc, Hill*, ISBN: 0-07-021463-8, (1987).

[20] Kumar A., Singh D., Goyal R. N., Kaur D., "Fabrication and nanoindentation properties of TiN/NiTi thin films and their applications in electrochemical sensing", *Talanta*, **78**, 964–969 (2009).

[21] Veprek S., "The search for novel, superhard materials", *J. Vac. Sci. Technol.*, **A 17 (5)**, 2401 (1999).

[22] Oliver W. C., Pharr G. M., "An improved technique for determining hardness and elastic modulus using load and displacement sensing indentation experiments", J. Mater. Res., **7**, 1564 (1992).

Chapter 6

Conclusions and Future Prospects

CHAPTER 6

CONCLUSIONS AND FUTURE PROSPECTS

6.1 Conclusions

6.1.1 Bipolar resistive switching behavior in Cu/AlN/Pt structure for ReRAM application.

6.1.2 Effect of top electrode material on resistive switching properties of WN based thin films for non-volatile memory application.

6.1.3 Pd capped W_2N nano porous thin films for remarkable room temperature hydrogen gas sensing performance.

6.1.4 Structural, corrosion, and mechanical properties of sputtered deposited chromium tungsten nitride ($Cr_{1-x}W_xN$) nanocomposite thin films.

6.2 Future prospects

6.1 Conclusions

The main objective of the present thesis is to fabricate several metal nitride thin films such as AlN, WN and CrWN on silicon (Si), Pt coated silicon ($Pt/Ti/SiO_2/Si$) and porous silicon (PSi) substrates using DC magnetron sputtering technique for various device applications. A brief summary and conclusion of the entire work are as follows.

(i) Resistive switching properties of AlN and WN thin films for ReRAM device application have been investigated.

(ii) Porous silicon (PSi) substrate was prepared by metal assisted chemical etching method and fabricate tungsten nitride (WN) nanoballs (NBs) structure for hydrogen gas sensing application.

(iii) Fabrication of ternary metal nitride $Cr_{1-x}W_xN$ nanocomposite thin films with different tungsten concentration and study their structural, corrosion and mechanical properties for protective coating on cutting tools.

6.1.1 Bipolar resistive switching behaviour in Cu/AlN/Pt structure for ReRAM application.

Highly stable bipolar resistive switching behaviour of Aluminium nitride (AlN) thin film sandwiched between Cu (top) and Pt (bottom) electrodes has been investigated. Resistive switching properties in Cu/AlN/Pt structure are induced by the formation/disruption of Cu conducting filaments in AlN thin film. Excellent non-volatile resistive switching characteristics have been observed at voltage of + 2.6 V and - 1.7 V. Trap controlled space charge limited current (SCLC) and ohmic behaviours are found to be dominant conduction mechanisms at high resistance state (HRS) and low resistance state (LRS) respectively. The resistance ratio of HRS and LRS is found of the order of ~ 10^4. Moreover, the proposed structure also showed an endurance till > 10^4 cycles and a non-volatile retention time for > 10^4 sec.

6.1.2 Effect of top electrode material on resistive switching properties of WN based thin films for non-volatile memory application.

The influence of top electrode (TE) material on resistive switching properties of DC magnetron sputtered tungsten nitride (WN) thin film with TE (Ti, Al and Cu)/WN/Pt stack configuration has been investigated. Bipolar resistive switching behaviour has been clearly found for all three top electrodes. The memory cells with Ti and Al TE exhibit two resistance states i.e. low resistance state (LRS) and high resistance state (HRS) switching which caused by formation and rupture of ionic filaments. The formation of additional Cu metallic filaments in WN layer are responsible for three resistance states (or say multilevel) switching for Cu TE. Temperature

vs resistance measurement confirms the formation of ionic and metallic filaments. The WN thin film show an excellent endurance over 10^5 cycles and non-volatile long retention of 10^5 sec along with ~ 10^2 resistance ratio between HRS/LRS. This study suggests that the electrode engineering of WN thin films have potential for non-volatile and multilevel resistive switching random access memory application.

6.1.3 Pd capped W_2N nano porous thin films for remarkable room temperature hydrogen gas sensing performance.

The hydrogen (H_2) gas sensing performance of palladium modified tungsten nitride (Pd/W_2N) nanoballs (NBs) grown on the porous silicon (100) substrate via reactive DC magnetron sputtering has been studied. Porous silicon (PSi) substrate has attracted enormous amount of consideration for gas sensing application due to its high reactive surface morphology. Reversible change in resistance is observed during hydrogenation and dehydrogenation process at room temperature. The H_2 gas sensing performances together with sensing mechanism of proposed Pd/W_2N NBs structure under low detection range (5-500 ppm) are discussed in detail. Moreover, the prime requirements for gas sensing such as stability, reproducibility and selectivity measurements are also studied at room temperature.

6.1.4 Structural, corrosion, and mechanical properties of sputtered deposited chromium tungsten nitride ($Cr_{1-x}W_xN$) nanocomposite thin films.

Chromium tungsten nitride ($Cr_{1-x}W_xN$) thin films are fabricated on silicon (100) substrate using reactive DC magnetron co-sputtering technique. X-ray diffraction pattern with different atomic concentrations of tungsten ($0<x<0.61$) shows the presence of (111) and (200) orientations for $Cr_{1-x}W_xN$. A small amount of tungsten addition led to significant changes in structural, electrochemical and mechanical properties of the $Cr_{1-x}W_xN$ films as a consequence of improved microstructure. The observed crystallite size varies from 31.1 nm to 15.2 nm with different W content. The lowest corrosion rate 39.8 nmy (nanometre penetration per year) is achieved for $Cr_{0.48}W_{0.43}N$ thin film. Hardness follows the Hall-Petch relation and tends to increase with decrease in grain size. Highest hardness of 43.18 GPa and elastic modulus of 341.02 GPa are achieved at the grain size of 15.2 nm in $Cr_{0.48}W_{0.43}N$ thin film. The alloying of W would be great technological interest in order to raise the performance of CrN thin films as protective coatings due to enhancement of structural, surface morphology, electrochemical and mechanical properties.

6.2 Future prospects

There are many unsolved issues and also new ideas related to these metal nitride thin films and structures, on which one can widen the study in future are as follows:

(i) The performance of AlN and WN thin film based memory devices can be enhanced in terms of endurance and retention by optimizing the vacancies and defects inside the active switching layer.

(ii) Electrode engineering with compatible metal could be a good approach for multilevel ReRAM application to fulfil future memory storage demands.

(iii) An attempt can be done to further enhance the W_2N NBs based hydrogen gas sensor which can be operate at harsh environment also by optimizing thickness, resistance and morphology of W_2N thin films.

(iv) Selection of appropriate alloying metal into binary metal nitride and make them ternary or quaternary metal nitride can be utilized for further enhancement of total performance of protective coatings.